UNIVERSITY OF OKLAHOMA

GRADUATE COLLEGE

UNDERSTANDING THE DIURNAL CYCLE AND ITS MODULATION UNDER LARGE SCALE INFLUENCES OVER THE MARITIME CONTINENT

A DISSERTATION

SUBMITTED TO THE GRADUATE FACULTY

in partial fulfillment of the requirements for the

Degree of

DOCTOR OF PHILOSOPHY

by HRAG NAJARIAN

Norman, Oklahoma

2026

Downloaded from SHAREOK. Persistent Handle URL: https://hdl.handle.net/11244/342853

UNDERSTANDING THE DIURNAL CYCLE AND ITS MODULATION UNDER LARGE SCALE INFLUENCES OVER THE MARITIME CONTINENT

A DISSERTATION APPROVED FOR THE
SCHOOL OF METEOROLOGY

BY THE COMMITTEE CONSISTING OF

Dr. James Ruppert Jr. (Chair)

Dr. Nakoko Sakaeda

Dr. Kathy Pegion

Dr. Renee Mc Pherson

©Copyright by HRAG NAJARIAN 2026

All Rights Reserved.

Acknowledgments

Writing this section after completing an entire dissertation is a strange feeling. I have spent the better part of 2026 writing scientific literature, focused on presenting a series of fact-based results that guide the reader through a story with a clear beginning, ending, and future implications. Now, I have to reach into the feelings part of my brain and put pen to paper about the people and experiences that have led me to where I am today. Below, I acknowledge a handful of people and moments that played a significant role in my academic journey.

I would not be where I am today without the support of my parents. Thank you, Mom and Dad. They immigrated to the United States to provide a better and safer life for our family. While the journey has been filled with long days working alongside my family, it has also been an incredibly fulfilling one—one I would never change if given the opportunity. My brother, Hagop, taught me to reach for the stars simply by watching him become the incredible person he is, despite all that he had to overcome. My oldest brother, Bedros, taught me patience and to never judge a book by its cover. Without them, I would just be an annoying—and even more spoiled—younger brother with no one to keep me in check. To my grandparents, uncles, aunts, cousins, and nieces, thank you for your endless love, support, and all the laughter we have shared over the years.

I cannot imagine making it through the final months of my doctorate without Bryony, my fiancée. She has been my number one fan, despite not always knowing exactly what I do, and she believed in me even when I did not believe in myself. I will never forget her support during the hardest of times—making sure there was always food on the table and reminding me to step away from work and take a break. Thank

you for your never-ending love and support. I cannot wait to spend the rest of my life with you.

Thank you to my wonderful advisors, James Ruppert Jr. and Naoko Sakaeda. I could not have asked for two better mentors. They each brought their own unique strengths to this journey, complementing one another throughout my doctorate in ways that made me a better scientist. It was a privilege to be your first Ph.D. graduate, and I cannot wait to see all the future students who will follow. Thank you for believing in my abilities from the moment you accepted me into your group and for supporting me every step of the way. Thank you to everyone in the Sakaeda Lab, Convective Storm Dynamics, and OU-UH research group for all the scientific conversations that have helped shaped my understanding of meteorology.

Thank you to all the friends I made in Norman. There are far too many of you to list individually, so I will have to resort to categories instead. Thank you to my housemates; my friends from volleyball, rock climbing, tennis, and frisbee; my colleagues and friends in NWC 5409; my car friends; friends of friends; Armenian friends; AMS friends; GCC friends; and classmates, some of which have no choice but to accept we will be lifelong friends. I am so lucky to have met some of the most amazing people in my lifetime during my time in Norman.

Thank you to everyone at the Goddard Health Center. This center provides free healthcare to students, and it helped me through the many physical injuries I managed to accumulate during my time at OU. Their counseling services also helped me navigate some of the most difficult moments of my life. Without the care and support they provide, both I and tens of thousands of students would have faced a much more difficult path.

Finally, thank you to everyone who, in ways both big and small, helped shape the person I have become. Whether through encouragement, friendship, mentorship, or

simply sharing a laugh when I needed it most, you have all left a lasting mark on my life. This dissertation may have my name on the cover, but it is the product of a community that lifted me up every step of the way.

Sincerely,

Dr. Hrag Najarian

Table of Contents

Acknowledgments iv

List of Tables ix

List of Figures x

Abstract xviii

1 Introduction 1

2 The Influence of Cloud-Radiative Interactions on the Diurnal Cycle over the Maritime Continent 6
2.1 Introduction 6
2.2 Data and Methods 9
2.2.1 Case Background State 9
2.2.2 Model Setup 10
2.3 Results 13
2.3.1 Cloud-Radiative Influence on the Diurnal Cycle of Rainfall . . . 13
2.3.2 Changes at the Surface due to Cloud-Radiative Interactions . . 18
2.3.3 Terrain's Influence on the Diurnal Cycle 21
2.4 Conclusions 30

3 Understanding the Environmental Influence of the Madden-Julian Oscillation on the Behavior of the Diurnal Cycle over the Maritime Continent 34
3.1 Introduction 34
3.2 Data and Methods 38
3.2.1 Case Background State 39
3.2.2 Model Configuration 39
3.2.3 Model Verification of Diurnal Rainfall Variability 41
3.2.4 Moisture and Circulation Sensitivity Experiments 43
3.3 Results 44
3.3.1 Moisture and Circulation Influence Diurnal Rainfall Differently Over Land and Ocean 44

3.3.2 Predominant Role of Moisture on Oceanic Diurnal Rainfall . . . 46
3.3.3 Understanding the Mechanisms Driving the Land Diurnal Cycle 49
3.3.4 Conclusions . . . 59

4 Summary and Conclusions . . . 64

Appendix A . . . 69

Appendix B . . . 83

Reference List . . . 86

List of Tables

3.1 Overview of the experimental design. Three swap experiments are performed during the MJO period by replacing ERA5 large-scale relative humidity (RH) and/or horizontal winds (U,V) in the initialization and lateral boundary conditions with values from the PreMJO period. . . . 44

List of Figures

2.1 a) The domain average ("All") diurnal composite of rain rate (mm/hr, log-scale) is calculated over the MC domain for CTRL (black, solid), and NCRF (black, dashed). It is split into the land (orange) and ocean (blue) domain. b) The diurnal composite of rain rate range difference between NCRF and CTRL are shown spatially, where red shading indicates greater diurnal range for NCRF and blue shading indicates CTRL has greater range. Three regions where transect analysis is conducted are overlaid in solid black rectangles and labeled A (Sumatra Mid Central), B (Sumatra Northwest), and C (Borneo Northwest). 14

2.2 The frequency distribution of the difference in diurnal-composite rainfall initiation timing in hours between NCRF and CTRL over ocean (blue), land (orange), and all (black). Rainfall initiation is defined for a given grid point where the rain rate time tendency is positive and rain rate exceeds 1 mm/hr. The solid vertical black line indicates the timing difference of zero hours, where a negative difference indicates earlier convection initiation in NCRF. The values next to each domain in the legend indicate the percentage of domain points that met or exceeded our criteria for convective initiation. 16

2.3 CTRL diurnal rain rate composite (mm/hr) is computed at the three regions from Fig. 2.1b, Sumatra Mid Central, Sumatra Northwest, and Borneo Northwest (a,c,e). The standardized rain rate difference of NCRF from CTRL is computed at each respective region (b,d,f), where reds indicate greater rain rate than CTRL, and blues indicate less. Positive/negative distances are offshore/onshore, with the vertical dashed brown and black lines representing the coastline and diagonal solid brown and black lines denoting a selection of phase speeds of offshore propagation. A 9 km (3-grid point) moving average is applied to the rain rates over the distance-from-coast dimension to smooth out the signal and isolate the most salient features. 17

2.4 a) The diurnal composite of surface flux (W/m^2) averaged over land for both CTRL (solid) and NCRF (dashed), with sensible heat flux (SH, green), latent heat flux (LH, blue), net shortwave radiative flux (SW, red), net longwave radiative flux (LW, orange), and their sum ($SH+LH+SW+LW$, Net, black). These values are positive downward, indicating energy input towards the surface. b) The diurnal composite of CTRL cloud fraction over land is shown w.r.t. pressure (left y-axis) in the shading, and the pressure-weighted and level-averaged low (1000-700 hPa, solid), mid (700-450 hPa, dashed), and high (450-200 hPa, dotted) cloud fraction is overlaid (right y-axis). 20

2.5 The fractional frequency of occurrence of the diurnal range of shortwave and sensible surface flux (shading) for NCRF (a), CTRL (b), normalized such that the sum over the x and y dimensions equals one. The average rain rate diurnal range is overlaid (contour) after smoothing using a 5-bin center-average (black, mm/hr). (c) The low level-average cloud fraction diurnal range (1000-700 hPa, shading) and terrain height (m, contour) is plotted for CTRL. 22

2.6 The CTRL diurnal composite evolution in local solar time of low (a, 1000-700 hPa), mid (b, 700-450 hPa), and high (c, 450-200 hPa) pressure-weighted and level-averaged cloud fraction as a function of terrain height (m) is plotted. The surface shortwave CRF (W/m^2) is overlaid as a contour (black), with increasingly negative values indicating stronger cloud-radiative cooling at the surface. 23

2.7 The frequency distribution of the diurnal range of rain rate (mm/hr) versus terrain height (m) over land, normalized by the terrain height bin, for NCRF (a), CTRL (b), and their difference (NCRF-CTRL) (c). Corresponding average rain rate range (green) at each terrain height bin is overlaid for NCRF (dashed), CTRL (solid), and their difference (black, dotted). Terrain averaged frequency (a, b) and anomalous frequency (c) of rain rate range is plotted below the heat maps (blue, solid). The number of terrain height samples at each terrain height bin is plotted (d) (blue, solid). 24

2.8 The average profiles of diurnal range of surface flux as a function of terrain height over land for NCRF (a), CTRL (b), and their difference (NCRF-CTRL) (c). Surface shortwave (SW, red), longwave (LW, brown), sensible (SH, green), latent (LH, blue), and the sum of sensible and latent (SH+LH, cyan) fluxes are shown. 25

2.9 The frequency distribution of the diurnal range of surface (10-m) slope flow (m/s) as a function of terrain height (m) over land, normalized by the terrain height bin, for NCRF (a), CTRL (b), and their difference (NCRF-CTRL) (c). Corresponding average slope flow range (green) at each terrain height bin is overlaid NCRF (dashed) in a), CTRL (solid) in b), and their difference (black, dotted) in c). Terrain averaged frequency (a, b) and anomalous frequency (c) of slope flow range is plotted below the heat maps (blue, solid). 27

2.10 The diurnal composite of CTRL 10-m wind speed (m/s) is plotted at times of maximum 10-m convergence over land (14 LST) (a) and ocean (6 LST) (c) after a 30 grid-point center point average, with arrows representing the wind direction. The wind speed difference (NCRF-CTRL) is shaded at the same times (b, d), where reds indicate stronger magnitude winds in NCRF, while blues indicate the opposite. The arrows represent the wind vector difference between NCRF and CTRL, where scaling of the arrows differ between the left and right column subplots. Arrows are not included where the magnitude of the wind speed difference (b, d) did not exceed 0.25 m/s. Terrain height at 750 m is overlaid in solid green. 29

3.1 The domain average diurnal composite of rain rate (mm/hr, log-scale) is calculated over the MC domain for WRF CTRL simulations after spatial regridding to match IMERG (triangles), and for IMERG after temporal aggregation to match WRF's hourly output (circles). Rain rates are averaged over the land (a) and ocean (b) domains during the PreMJO (solid) and MJO (dashed) periods. c,d) The diurnal composite of rain rate range difference between PreMJO and MJO are shown spatially after WRF spatial regridding and IMERG temporal aggregation, where red shading indicates greater diurnal rain rate range during the PreMJO period and blue shading indicates greater diurnal rain rate range during the MJO period. 42

3.2 Time-averaged vertically integrated (1000-100 hPa) relative humidity (VI RH, %) and 850-hPa wind vectors (m/s) are calculated for each simulation. 44

3.3 The grid-point difference of (a) diurnal rain rate range (mm/hr) and (b) time-averaged vertically integrated (1000-100 hPa) relative humidity (VI RH, %) from MJO domain-averaged over land (brown, no hatch) and ocean (blue, hatched) points, where X represents the corresponding simulation labeled on the x-ticks. The black brackets represent the confidence interval at a 95% confidence level through bootstrapping at $N = 1000$. 46

3.4 The daily rain rate (mm/day) and vertically integrated (1000-100 hPa) relative humidity (VI RH) is calculated for all days (N=10 days) and binned at 1% VI RH intervals over (a) land and (b) ocean points for all simulations, with the corresponding number of points (log-scale) at each VI RH bin (c,d). The scatter points represent the time-averaged rain rate and relative humidity across the entire time period. 47

3.5 Time-averaged rain rate (mm/hr) for each simulation. 48

3.6 The PreMJO-to-MJO terrain face changes in (a) land-average diurnal rain rate range, (b) coastal- and time-averaged 950-hPa onshore flow, (c) coastal-averaged diurnal coast-normal 2-m potential temperature gradient ($\nabla_n \theta_{2\,\mathrm{m}}$) range, (d) coastal-averaged diurnal sea-level pressure (SLP) range, (e) land- and time-averaged convective available potential energy (CAPE), (f) land- and time-averaged convective inhibition (CIN) are averaged over the four main islands (Sumatra, Borneo, Java, and Sulawesi) over the western (teal, no hatch) and eastern (orange, hatch) terrain faces for the $PreMJO$ and MJO. The black brackets represent the confidence interval at a 95% confidence level through bootstrapping at $N = 1000$. 53

3.7 Same as Fig. 3.6 but with the y-axis representing land- and time-averaged vertically integrated relative humidity (VI RH) between (a) 1000-100 hPa, (b) 1000-700 hPa, (c) 700-500 hPa, (d) 500-100 hPa. 56

3.8 Same as Fig. 3.6a, but for all simulations. 57

3.9 (a) Coastal- and time-averaged 950-hPa onshore flow and the diurnal coastal thermal gradient range and the (b) land- and time-averaged vertically integrated relative humidity (VI RH) calculated between 1000-100 hPa and land-averaged diurnal rainfall range is shown for each simulation (marker shape) and terrain face (color and edge line). 58

A.1 The WRF model simulation domain is shown, where shading represents terrain height (m), the solid black rectangle represents the high-resolution nested domain (3-km grid spacing), and the three regions where cross-sectional analysis is conducted is overlaid in solid red rectangles and labeled A (Sumatra Mid Central), B (Sumatra Northwest), C (Borneo Northwest). 70

A.2 (a) The domain average ("All") diurnal composite of rain rate (mm/hr, log-scale) is calculated over the MC domain for CTRL (black, solid), and IMERG v7 (black, dashed). It is split into the land (orange) and ocean (blue) domain. (b) The diurnal composite of rain rate range difference between IMERG v7 and CTRL are shown spatially, where red shading indicates greater diurnal range for IMERG and blue shading indicates CTRL has greater range. Three regions where transect analysis is conducted are overlaid in solid black rectangles and labeled A (Sumatra Mid Central), B (Sumatra Northwest), and C (Borneo Northwest). . . . 71

A.3 Same as Fig. 2.1, but for dates December 10-20, 2015. 72

A.4 The maximum diurnal rain rate is calculated over land (orange) and ocean (blue) and compared between CTRL (solid) and NCRF (dashed). Data is binned at a 1 mm/hr interval in the x-axis, and the 1 mm/hr threshold (solid, black) used in the study is plotted for comparison. Fractional count refers to the number of counts in the bin divided by the total number of counts. 81% of CTRL land, 85% of NCRF land, and 62% of CTRL and NCRF ocean data is retained with a 1 mm/hr threshold. 73

A.5 Utilizing data from CTRL, spatial analysis of (a) the diurnal composite of rain rate range (mm/hr) and (b) the local solar time of when the diurnal composite of rain rate phase maximizes is shown. Rain rates were first spatially smoothed by running a 5-grid point centered moving mean. High rainfall rates exist over regions with high terrain, and frequent occurrence of rain rate ranges exceeding 1 mm/hr over ocean. Additionally, some coastal regions show a smooth gradient of local solar time, suggesting the existence of offshore propagation of convection. . . 74

A.6 The fractional frequency distribution of the difference in rain rate phase maximum between simulations ($NCRF - CTRL$) is calculated as a function of distance from coast. Negative distance from coast values represents the land, while positive represents the ocean. The solid green line is the average time difference at each distance from coast bin, where negative represents earlier NCRF diurnal composite rain rate maximum timing compared to CTRL, and positive represents and earlier CTRL timing. Earlier rain rate maximum timing exists over land and up to 150 km into the ocean in NCRF, but becomes indistinguishable past 150 km offshore, suggesting earlier initiation is largely constrained near and over land. 75

A.7 A frequency distribution between layer-averaged low (a, d, g), mid (b, e, h), and high (c, f, i) cloud fraction and surface cloud-radiative forcing (CRF) in the longwave (a–c), shortwave (d–f) and net (g–i) is conducted over land. The horizontal black line represents the CRF value of zero. Positive CRF values indicate cloud-radiative warming and negative values indicate cloud-radiative cooling at the surface. Data points where cloud fraction was equal to zero were removed. 76

A.8 The maximum (solid) and minimum (dotted) of the diurnal composite of soil moisture (0-0.1m) is averaged at each terrain height bin in (a) NCRF, (b) CTRL, and (c) their difference $NCRF - CTRL$. Minimum soil moisture follows closely between simulations, but the difference in maximum soil moisture deviates increasingly with increasing terrain height. This suggests NCRF soil moisture is moister as terrain height increases compared to CTRL. 77

A.9 The maximum (solid) and minimum (dotted) of the diurnal composite 2m temperature (red) and surface temperature (brown) are averaged at each terrain height bin in (a) NCRF, (b) CTRL, and (c) their difference $NCRF - CTRL$. While CTRL surface and 2m temperatures decrease at a constant rate, NCRF maximum surface temperature deviates and decreases at a much slower rate than that of CTRL. The temperature difference between simulations highlights the slower rate of decrease with increasing terrain height, showing NCRF maximum surface temperatures of nearly 7 K greater than CTRL at the highest points. The difference also shows how minimum temperatures are slightly cooler in NCRF, likely due to the absence of longwave trapping at nighttime. 78

A.10 The fractional frequency of occurrence of the terrain height (m) and terrain height slope (unitless) is conducted (shading), normalized such that the sum over x and y dimensions equal one. The best-fit line is plotted in dashed green after finding the linear relationship between both variables, along with a reference one-to-one line. The best-fit line closely follows the one-to-one line, along with a relatively high R^2 value, both suggesting that terrain slope and terrain height are linearly correlated. 79

A.11 The maximum (solid) and minimum (dotted) of the diurnal composite 10-m orographically forced surface vertical motion (m/s) are averaged at each terrain height bin in (a) NCRF, (b) CTRL, and (c) their difference $NCRF-CTRL$. Both the maximum and minimum increasingly diverge from 0 with increasing terrain height in both simulations. The difference between NCRF and CTRL show both differences in the maximum and minimum nearly equally contributing to the higher NCRF range compared to CTRL. The maximum in NCRF is significantly higher than CTRL, suggesting that upslope/anabatic winds see a greater increase compared to downslope/katabatic winds. 80

A.12 The frequency distribution of the diurnal range of 10-m wind divergence ($1/s$) as a function of terrain height (m) over land, normalized by the terrain height bin, for (a) NCRF, (b) CTRL, and (c) their difference $NCRF-CTRL$. Corresponding average surface divergence range (green) at each terrain height bin is overlaid NCRF (dashed) in (a), CTRL (solid) in (b), and their difference (black, dotted) in (c). Terrain averaged frequency (a, b) and anomalous frequency (c) of divergence range is plotted below the heat maps (blue, solid). 81

A.13 The local solar time of when CTRL diurnal slope flow maximizes is show w.r.t. upslope and downslope flow. Fractional count refers to the number of counts in the bin divided by the total number of counts. Upslope flow maximizes over all land points around 12-16 LST, while downslope flow maximizes at 6 LST with a local maximum at 19 LST that likely is associated with precipitation downdrafts and cold pools over terrain. 82

B.1 The fifth generation ECMWF atmospheric reanalysis (ERA5) data set of (a,b) zonal wind (m/s) and (c,d) specific humidity (kg/kg), time series averaged latitudinally (10°S-10°N) over the western Maritime Continent (MC) domain for both (a,c) $PreMJO$ and (b,d) MJO time periods. . 83

B.2 The outer (d01), inner (d02, white), and the domain analysis nest (red) is shown. 84

B.3 (a) Terrain height (m, log-scale) is shown in the color contour, with an overlay of the ridge line used to divide the islands into their western/eastern (southern/northern for Java) counterparts. The island of Sumatra is used as an example to show the distance from coast (km) values over the (b) western and (c) eastern sides of the ridge lines. . . . 85

Abstract

The Maritime Continent (MC) is one of the most convectively active and topographically complex regions on Earth, where diurnal convection strongly influences the regional hydrological environment and global circulation through interactions with large-scale tropical circulations like the Madden-Julian Oscillation (MJO). Despite its importance, numerical weather prediction and general circulation models (GCMs) struggle to accurately represent both the timing and intensity of the diurnal cycle of convection and the propagation of the MJO across the MC, highlighting the need to improve our understanding of the physical processes governing diurnal convection, which have been shown to affect the MJO. This dissertation investigates the mechanisms that modulate the diurnal cycle over the western MC and examines how MJO-induced large-scale environmental conditions modify these processes using convection-permitting simulations with the Weather Research and Forecasting model.

The first part of this dissertation examines the role of cloud-radiative interactions on the diurnal cycle of rainfall. Through the removal of cloud-radiative interactions in the model, this study demonstrates that cloud-radiative interactions suppress daytime island diurnal rainfall by reducing surface shortwave heating. This weakens surface turbulent fluxes, reducing rainfall intensity and delaying convective initiation. Diurnal rainfall sensitivity is greatest over mountainous regions, where orographic forced ascent promotes frequent low clouds that enhance cloud shading, suppressing diurnal rainfall and delaying convective initiation. This study demonstrates that erroneous representation of cloud-radiative interactions likely contributes to errors in the diurnal cycle, particularly over mountainous regions, partially explaining or exacerbating the biases in GCMs.

The second part investigates how the MJO modulates the diurnal cycle of rainfall through changes in the environmental moisture and circulation upon its propagation over the western MC. A series of novel initialization and boundary condition experiments are conducted to test the sensitivity of diurnal rainfall to changes in MJO-associated moisture and/or winds. Upon the onset of the MJO enhanced phase, diurnal rainfall strengthened over the oceanic regions, driven primarily by the increase in environmental moisture, likely dampening the dry-air entrainment that suppresses convective intensity and persistence. The modulation of diurnal rainfall over the islands depended on terrain-face direction, with the western sides experiencing weaker diurnal rainfall as stronger MJO-associated turbulent mixing diluted the land-sea thermal gradient driving the diurnal circulation, while the eastern sides experienced stronger diurnal rainfall because the moister MJO environment, particularly in the mid-to-upper troposphere, enhanced convection. This study highlights the mechanisms that drive the modulation of diurnal rainfall upon the onset of the MJO enhanced phase and demonstrates how MJO-associated moisture and circulation modulate the strength of these mechanisms.

Collectively, this dissertation establishes that MJO-associated cloud-radiative interactions, environmental moisture, and circulation each regulate distinct components of the MC diurnal cycle. Cloud-radiative interactions primarily control the local strength and timing of island convection, environmental moisture governs oceanic rainfall strength, and environmental winds and moisture determine the spatial distribution of island convection. These findings improve the physical understanding of the multi-scale mechanisms over the MC and provide a framework for evaluating the modulation of tropical convection under large-scale changes across regional and global scales.

Chapter 1

Introduction

The diurnal cycle of rainfall is the dominant component of atmospheric variability in the tropics, rendering it vital to global weather patterns, climate dynamics, and regional water resource management (Dai et al., 2007). Over the Maritime Continent (MC), a geographically complex region of vast islands and shallow seas, millions of people depend on a prominent diurnal cycle of rainfall to provide a consistent daily source of freshwater. Despite the socioeconomic importance of the diurnal cycle of convection and the critical role it plays in the global radiation budget and large-scale atmospheric circulation (Matus and L'Ecuyer, 2017), general circulation models (GCMs) systematically struggle to accurately represent the diurnal cycle's peak timing, strength, and spatial distribution (Yin and Porporato, 2017; Tang et al., 2021; Dong et al., 2023). Over the MC, diurnal convection is strongly modulated by larger-scale tropical disturbances, most notably the Madden-Julian Oscillation (MJO)—the dominant mode of tropical intraseasonal variability (Madden and Julian, 1971). However, MJO propagation across the MC remains poorly represented in GCMs, and the modulation of the diurnal cycle of convection by the MJO has been identified as a key process influencing its propagation through the region (Zhang and Ling, 2017; Ling et al., 2019; Bai and Schumacher, 2022; Chen et al., 2022). Therefore, it is essential to diagnose the mechanisms governing diurnal convection over the MC and determine how the MJO's large-scale environment modifies these mechanisms, thereby guiding efforts to improve the representation of both diurnal convection and the MJO in GCMs.

The diurnal cycle of rainfall over the MC is primarily governed by the land–sea

breeze circulations and mountain–valley winds, both of which are driven by solar insolation (Ray and Zhang, 2010; Wei et al., 2020; Tan et al., 2022; Lopez-Bravo et al., 2023). Daytime solar heating acts to destabilize the boundary layer over land and establish a land–sea thermal gradient that drives the sea-breeze circulation, promoting low-level convergence for the initiation of convection over land. Concurrently, differential heating along mountain slopes induces strong anabatic (upslope) winds that aid in initiating rainfall earlier and more intensely than over flat terrain (Tan et al., 2022). At night, these flows reverse to katabatic (downslope) winds and interact with gravity waves and the coastal land breeze to initiate and sustain offshore-propagating convective systems (Rampanelli et al., 2004). Oceanic diurnal rainfall strength maximizes in the early morning, aided by cloud-radiative interactions that destabilize the atmosphere through differential heating (Ruppert and Hohenegger, 2018). While these interactions continue existing over the MC with the propagation of the MJO, they end up modulating in strength with the changing environmental conditions, resulting in significant changes in the land and ocean diurnal cycle of rainfall.

The MJO modulates the diurnal cycle of rainfall over the MC through intraseasonal changes in environmental conditions (Rauniyar and Walsh, 2011; Peatman et al., 2014; Bai and Schumacher, 2022). Ahead of the MJO's enhanced phase of convection, diurnal rainfall peaks over land and subsequently weakens as the system approaches; conversely, oceanic diurnal rainfall intensifies as the MJO nears and propagates over the MC. This suggests that the the dominate rainfall domain goes from land-to-sea with the propagation of the MJO enhanced phase over the MC (Vincent et al., 2016; Peatman et al., 2014). Additionally, the MC often acts as a barrier as the MJO approaches from the Indian Ocean, resulting in the convective envelope to weaken and/or stall over the region (Ling et al., 2019; Bai and Schumacher, 2022). Interestingly, the diurnal cycle of rainfall over both land and ocean over the MC are more pronounced when the

MJO successfully propagates across the region, suggesting that the diurnal cycle may play an underappreciated role in facilitating MJO propagation (Zhang and Ling, 2017; Ling et al., 2019). Therefore, the intraseasonal evolution of diurnal rainfall has been suggested to be important for the continual propagation of the MJO across the MC, but the underlying mechanisms driving the diurnal rainfall evolution remain uncertain.

The MJO strongly modulates environmental moisture, wind, and cloud-cover, all of which affect the mechanisms that drive the diurnal cycle of rainfall over land and ocean. The MJO convective envelope increases cloud frequency and cloud cover over the MC (Riley et al., 2011), reducing the solar insolation that destabilizes the island boundary layer and drives the sea-breeze circulation. At the same time, enhanced cloud-radiative interactions increase oceanic diurnal rainfall through differential atmospheric heating (Ruppert and Hohenegger, 2018), which collectively would strengthens the land–sea contrast in the diurnal cycle of rainfall. Others suggest that large-scale MJO dynamics simply create more favorable environmental conditions over the ocean—such as enhanced low-level zonal moisture flux convergence—to independently fuel oceanic convective systems (Zhang and Ling, 2017). Concurrently, the spatial distribution of diurnal rainfall over the islands has been observed to shift from western-to-eastern-facing terrain as the MJO propagates across the MC (Ichikawa, 2006; Zhou et al., 2022). It is clear that the MJO induced environment effects the diurnal cycle of convection over MC, but understanding which mechanisms drive these changes and how the MJO environment modulates their strength can provide critical insight into understanding the barrier effect GCMs face.

Observational studies have suggested that the land-sea breeze is suppressed with stronger background wind speeds and cloudier conditions, resulting in generally weaker diurnal rainfall (Qian et al., 2012; Fujita et al., 2011; Qian et al., 2013). However, this weaker diurnal rainfall is not seen across the island as background wind direction has

found to strengthen the suppression of diurnal rainfall more over the windward side, while slightly strengthening diurnal rainfall over the leeward side (Virts et al., 2013; Ichikawa, 2006). Idealized modeling studies have provided the theoretical insights regarding how low-level background wind amplitude and direction and cloud cover can dilute the land-sea thermal gradient unevenly along the islands coastline, thereby weakening the strength of the land-sea breeze (Ichikawa, 2006; Wang and Sobel, 2017; Zhou et al., 2023; Natoli and Maloney, 2023b; Ruppert and Chen, 2020; Segal et al., 1986). Despite our theoretical understanding of the possible mechanisms at play, no numerical modeling study has conducted a non-idealized experiment that explicitly tests the MJO induced cloud-radiative, moisture, and wind influence on the diurnal cycle of rainfall, to the authors knowledge. While numerical models are inherently approximations of the real world, convection-permitting simulations can resolve convection while maintaining the topographical and geographical configurations necessary to evaluate real-world convective responses. We leverage their capabilities to systematically remove or isolate specific physical controls—such as cloud-radiative interactions and large-scale moisture and/or winds—to better isolate the physics governing tropical convection over the MC in a way idealized or observational frameworks cannot.

This dissertation aims to identify the underlying physical mechanisms that regulate diurnal variations across the land and ocean environments of the MC and how the MJO can disrupt the daily cycle of rainfall through changes in environmental conditions. To accomplish this, Chapter 2 will answer two questions focusing on how cloud-radiative interactions over complex terrain influence diurnal convection over the MC:

1. What processes do cloud-radiative interactions influence to affect the diurnal cycle of convection over the MC?

2. How does topography over the MC affect how cloud-radiative interactions influ-

ence the diurnal cycle of convection?

Chapter 3 will answer two final questions that expand our understanding of the relative large-scale influence cloud-radiative interactions, moisture, and winds have on the mechanisms governing the intraseasonal change in the diurnal cycle of convection:

1. How does the MJO induced large-scale moisture and wind conditions influence the diurnal cycle of convection over the MC?

2. What are the mechanisms through which large-scale moisture and circulation influence diurnal rainfall?

Chapter 2

The Influence of Cloud-Radiative Interactions on the Diurnal Cycle over the Maritime Continent

This chapter has been published in the following peer-reviewed journal article. Najarian, H., Ruppert, J., & Sakaeda, N. (2025). The influence of cloud-radiative interactions on the diurnal cycle over the maritime continent. Journal of Geophysical Research: Atmospheres, 130, e2025JD044512. https://doi.org/10.1029/2025JD044512.

WRF model specifications and configurations for the simulations used are published. Najarian, H. (2025). Premjo wrf namelists. Zenodo. https://doi.org/10.5281/zenodo.17353651.

2.1 Introduction

The diurnal cycle of rainfall is the dominant component of rainfall variability, rendering it vital to weather patterns, climate dynamics, and water resource management across the world (Dai et al., 2007). The Maritime Continent (MC) is a region where millions of people depend on the prominent diurnal cycle of convection to provide a consistent daily source of rainfall (Kikuchi and Wang, 2008; Peatman et al., 2014; Lu et al., 2019; Love et al., 2011). Despite the importance of the diurnal cycle locally and its influence on the global radiation budget (Matus and L'Ecuyer, 2017), the latest general circulation models (GCMs) continue to struggle with accurately representing the diurnal cycle's peak timing and strength (Yin and Porporato, 2017; Tang et al., 2021; Dong et al., 2023). These inaccuracies are associated with errors in convective parameterization (Wang et al., 2020), directly influencing cloud production and areal coverage and

amplifying uncertainty in the prediction of Earth's radiative energy balance (Zelinka et al., 2020; Boucher et al., 2013). This especially becomes important over topographically complex regions such as the MC, where the low-resolution of GCMs can smooth out key topographic features (i.e., valleys, steep slopes) that are vital in the diurnal cycle of convection. Therefore, it is essential to leverage higher-resolution convection permitting models to better understand how cloud-radiative interactions can influence the diurnal cycle of convection.

Over the MC, cloud cover is strongly modulated by the Madden-Julian Oscillation (MJO), with studies suggesting that the "blocking" of the MJO by the MC can be attributed to the strength of the diurnal cycle of convection over the region (Zhang and Ling, 2017; Ling et al., 2019). Therefore, systematic model errors in representing the diurnal cycle of convection can influence predictions of the interaction between the MC and larger-scale weather and climate patterns, such as the MJO (Qian et al., 2013; Najarian and Sakaeda, 2023; Ding et al., 2024). Progress in addressing such model inadequacies is limited by our incomplete knowledge of diurnal convective-scale processes. This study will investigate the diurnal cycle of convection over the MC, focusing on the influence of cloud-radiative interactions on diurnal cycle characteristics.

The islands of the MC vary in their orientation, size, and terrain heights, leading to regionally unique patterns of diurnal convection driven by interacting land-sea breezes, mountain-valley breezes, and insolation (Ray and Zhang, 2010; Wei et al., 2020; Tan et al., 2022; Lopez-Bravo et al., 2023). When daytime insolation heats regions of steep terrain, strong anabatic (upslope) winds develop and initiate rainfall earlier and/or more strongly than over a region with flat terrain. These flows reverse to katabatic (downslope) at night, aiding in nocturnal offshore-propagating convection associated with the land breeze (Rampanelli et al., 2004). Offshore-propagating convection is a prominent feature of the diurnal cycle over the MC, with studies suggesting the im-

portance of the land breeze at near-shore distances and of gravity waves for sustaining the propagation over greater offshore distances (Mapes et al., 2003; Vincent and Lane, 2016; Ruppert and Zhang, 2019; Peatman et al., 2025; Tang et al., 2025).

Less well understood is how cloud–radiative interactions influence the development and evolution of diurnal convection over the MC. Clouds influence surface insolation through mechanisms such as the cloud-albedo effect, which reduces the amount of shortwave radiation reaching the surface, while their longwave emission can enhance downwelling longwave radiation (L'Ecuyer et al., 2019). Low-level clouds are the most effective at reducing insolation through the albedo effect due to their microphysical properties that make them highly reflective relative to mid- or high-level clouds, but also their frequent occurrence around solar noon (Burleyson et al., 2015). For example, the reduction of surface solar heating over land by clouds may impact the afternoon-to-evening timing and intensity of diurnal rainfall over land through changes in the timing and strength of the sea breeze.

Theories on the diurnal cycle of convection over open ocean suggest the importance of diurnal cloud-radiative heating and its interaction with deep convection (Sui et al., 1997; Yang and Smith, 2006; Ruppert and Hohenegger, 2018). What is not well understood, however, is if and how cloud-radiative interactions influence the diurnal cycle of convection at the intersection of land and ocean in places like the MC. Understanding if and how cloud–radiative interactions influence the diurnal cycle of convection over the MC is crucial for a complete understanding of convection and climate in this region.

To our knowledge, no study to date has assessed the role of cloud-radiative interactions in complex contexts such as the MC, where the land and oceanic diurnal cycle processes intersect. Here we address this gap by utilizing a convection-permitting model to simulate the diurnal cycle over the MC and assess the impact of cloud-radiative interactions. In this study, we address three questions: 1) How do cloud-radiative in-

teractions influence the diurnal cycle of convection over the MC? 2) What processes explain the changes in the diurnal cycle of convection when cloud-radiative interactions are removed? 3) How does the unique topography of the MC affect the cloud-radiative feedback in the diurnal cycle of convection?

2.2 Data and Methods

We select a case between November and December 2015 that corresponds with a well-documented strong diurnal cycle of convection and the frequent occurrence of offshore propagating convection over the MC (Yokoi et al., 2017). Below we discuss the observed atmospheric state and the diurnal cycle over the MC during this time period, as well as our model experiment that tests the impact of cloud-radiative interactions on the diurnal cycle.

2.2.1 Case Background State

The diurnal cycle of convection is influenced by the background thermodynamic and dynamic state. The El Niño Southern Oscillation (ENSO) influences environmental conditions such as the vertical moisture profile, wind direction and speed, and oceanic temperatures over the MC (Lu et al., 2023), directly influencing the diurnal cycle of convection over the MC (Bai and Schumacher, 2022; Natoli and Maloney, 2023a; Lu et al., 2023; Peatman et al., 2014). During the chosen study period, strong El Niño conditions were present, generally resulting in a stronger diurnal cycle of rainfall over the western MC and a weaker diurnal cycle in the northern and eastern MC (Yokoi et al., 2019; Lu et al., 2023).

The MJO also influences the diurnal cycle of convection over the MC by altering the background moisture, wind, and cloud state. When the MJO convective signal is

over the Indian Ocean, stronger background easterlies enhance the frequency of offshore propagating diurnal convection over the MC and overall enhance diurnal rainfall variability as the MJO approaches the MC (Peatman et al., 2014; Ling et al., 2019; Zhou et al., 2022). Based on the Real-time Multivariate MJO index from Wheeler and Hendon (2004), an MJO convective signal that hovers in and out of the threshold amplitude of 1 was present over the Indian Ocean in mid-November-to-early-December 2015 (MJO phase 2-3). If outgoing longwave radiation MJO index (OMI) is used, the amplitude is less than 1 throughout the time period, suggesting that a low-amplitude MJO signal was present (Kiladis et al., 2014).

The weak state of the MJO suggests that the MJO had a minor influence on the diurnal cycle of convection over the MC (Yokoi et al., 2017). Yokoi et al. (2017) shows a regional view of the observed offshore propagation of convection in November and December 2015 over the western central-coastal region of Sumatra through radar-estimated rain rates. Their results show that convection over land maximizes at around 15 local solar time (LST), and moves offshore around 18 LST. The diurnal composite speed of offshore propagation begins at 3 m/s near the coastline, but increases in speed to 8 m/s farther offshore. These results provide a regional expectation of how the diurnal cycle of convection should behave in our simulations.

2.2.2 Model Setup

The Advanced Research Weather Research and Forecasting (WRF) model Version 4.3.3 is utilized in this study to simulate the diurnal cycle over the MC (Skamarock et al., 2021). A 10.5-day control (CTRL) simulation is conducted from 1200 UTC November 22 ($\sim$19 LST) to 0000 UTC December 3 ($\sim$07 LST) 2015, with the first 12 hours removed to account for model spin-up. The WRF Model configuration for CTRL includes an outer domain of 12-km grid spacing with the Tiedtke cumulus scheme

applied, and an inner nest of 3-km grid spacing with explicit convection (Fig. A.1). The model has 55 vertical levels, with vertical spacing between levels increasing with height, with a model top at 10 hPa. Model output is saved at an hourly frequency. Both domains use the WRF Double-Moment 6-class microphysics (Lim and Hong, 2010), RRTMG radiation (Iacono et al., 2008), and the Noah Land Surface Model (Ek et al., 2003).

To ensure the model simulates rainfall rates that closely match observational measurements, sensitivity tests were conducted. The microphysical parameterization was found to influence rain rate significantly, where the WRF double moment 6-class scheme performed closest to satellite-based rainfall estimates from Integrated Multi-satellitE Retrievals for the Global Precipitation Measurement Mission (IMERG) version 7 (Huffman et al., 2023). Observational comparison between WRF rain rate output and IMERG over the 10 days shows consistent diurnal rainfall timing compared to CTRL, but not in amplitude over land (Fig. A.2a). Spatial analysis of the diurnal rain rate range difference between IMERG and CTRL show that regions with the greatest difference are generally collocated over land, particularly over regions with high terrain (Fig. A.2b). However, IMERG rainfall estimates over orographically complex regions are also known to deviate from rain gauge measurements (Sari et al., 2024; Xiong et al., 2025; Ramadhan et al., 2024). Considering the uncertainty of IMERG, particularly over the complex terrains, the comparison between IMERG and CTRL indicates that the diurnal cycle of rainfall is adequately represented in CTRL.

To examine how cloud-radiative interactions influence the diurnal cycle of convection, an ensemble of sensitivity simulations is conducted, where cloud-radiative interactions are turned off via the namelist option "icloud" (NCRF; these simulations are otherwise identical to CTRL). Setting this parameter to zero excludes hydrometeors from the radiative transfer model, effectively making all cloud transparent to radia-

tion. NCRF simulations are initialized using CTRL data at 0000 UTC (roughly, local sunrise) starting November 23 and run for 36 hours, repeating this for each of the first 9 days of the CTRL run. This produces an ensemble of 9 NCRF simulations, showcasing how the diurnal cycle of convection evolves when cloud-radiative interactions are excluded. This time-staggered ensemble approach minimizes the mean-state drift of the NCRF simulations that is expected over time scales significantly beyond a day.

To analyze the difference between CTRL and NCRF, diurnal composites are calculated by averaging the overlapping days between simulations (N=9 days) for a corresponding time of day. We leverage diurnal compositing to isolate the most robust, repeated patterns of the diurnal cycle, while we also assess day-to-day variance to quantify the deviation from the composite patterns. Both methods produce similar results, so for simplicity, the diurnal composite method will only be shown. We often utilize diurnal range as a metric to diagnose the strength of diurnal variation throughout the study, but unless stated otherwise, results are nearly identical when substituted with diurnal maximum. Additionally, all analysis is conducted using the higher-resolution inner domain (3-km), with domain averages calculated between 10°S−10°N and 90°E−125°E. Changes in the diurnal composites between NCRF and CTRL are statistically significant, determined through bootstrapping with 500 iterations with repetition and the two-tailed 95% confidence level. The current sample size of 9 days can introduce some biases, such as results being specific to MJO suppressed conditions. However, the consistent results among all 9 days suggest the signal is robust. Additional analysis between December 10-20 (N=10, during RMM phase 4-5), during the enhanced phase of the MJO, shows very similar results, suggesting the findings of this paper are not specific to MJO phase (Fig. A.3).

2.3 Results

2.3.1 Cloud-Radiative Influence on the Diurnal Cycle of Rainfall

We first examine rain rate characteristics of the diurnal cycle over the MC to understand the influence cloud-radiative interactions have on the diurnal cycle. First, LST is calculated ($LST = UTC + (\lambda/15)$), where λ represents the longitude at each grid point. The diurnal composite of rain rate in LST is then calculated, where Fig. 2.1 illustrates the diurnal composite of rain rate in CTRL and NCRF domain averaged over land and ocean (Fig. 2.1a) as well as the spatial difference (NCRF-CTRL) of the diurnal composite of rain rate range (Fig. 2.1b). The diurnal rain rate range is calculated by taking the difference between the diurnal composite rain rate maximum and minimum. Rainfall over land throughout the entire diurnal cycle increases in NCRF compared to CTRL, with the diurnal rain rate range increasing by 34% compared to CTRL, largely driven by the maximum. Over ocean, the NCRF diurnal rain rate range increases by 7% compared to CTRL, driven by an increase in rainfall during the early morning hours, and a decrease in rainfall in late afternoon hours (Fig. 2.1a). Over the entire domain (land and ocean, labeled as "All"), diurnal rainfall in NCRF is the same or more than CTRL, suggesting that the removal of cloud-radiative interactions increases rainfall over the MC.

The difference in the diurnal rain rate range between NCRF and CTRL at each grid point highlights the strong regional dependence of the impact when cloud-radiative interactions are removed (Fig. 2.1b). The region dependence is discussed in more detail in section 3.3, but an increase of diurnal rain rate range is apparent nearly everywhere, including over ocean, albeit with a lower magnitude change than over land.

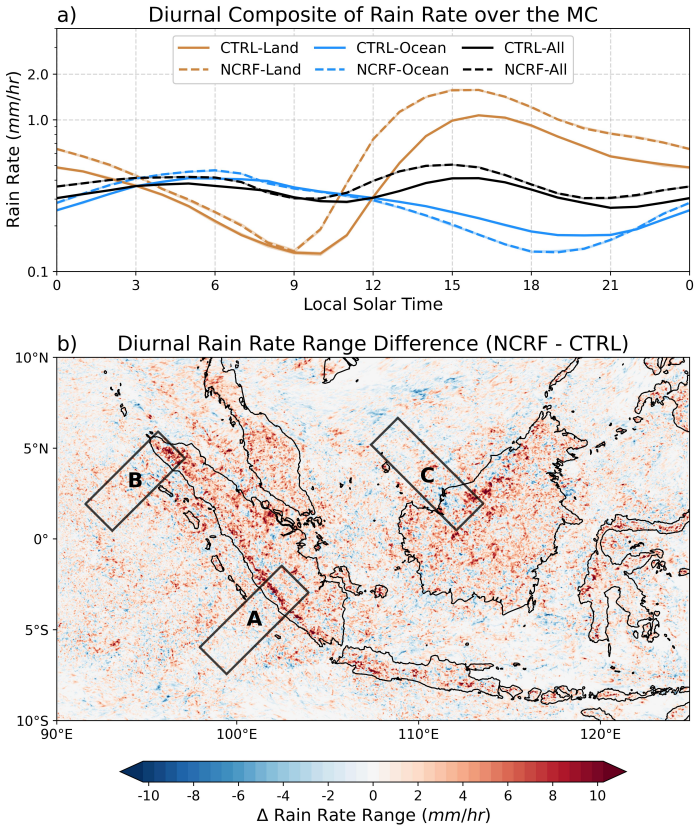

Figure 2.1: a) The domain average ("All") diurnal composite of rain rate (mm/hr, log-scale) is calculated over the MC domain for CTRL (black, solid), and NCRF (black, dashed). It is split into the land (orange) and ocean (blue) domain. b) The diurnal composite of rain rate range difference between NCRF and CTRL are shown spatially, where red shading indicates greater diurnal range for NCRF and blue shading indicates CTRL has greater range. Three regions where transect analysis is conducted are overlaid in solid black rectangles and labeled A (Sumatra Mid Central), B (Sumatra Northwest), and C (Borneo Northwest).

The largest difference in diurnal rain rate range occurs over regions with high terrain, suggesting a stronger cloud-radiative influence over mountainous regions, consistent with observational findings from the Upper Indus Basin (Forsythe et al., 2015). The removal of cloud-radiative interactions, therefore, increases the diurnal variability of rain rate, but it also influences the diurnal timing of rainfall.

The daytime pickup of rainfall over land begins about an hour earlier in NCRF than CTRL (Fig. 2.1a). The earlier increase in diurnal rain rate in NCRF implies

that diurnal convection initiates earlier over land when cloud-radiative interactions are turned off. To better assess this shift in diurnal rainfall initiation timing, we assess rainfall initiation at each grid-point, which is defined by the occurrence of two specific conditions: 1) the diurnal composite of rain rate (RR) is increasing ($dRR/dt > 0$) and 2) rain rate exceeds a predetermined rain-rate threshold. The first condition isolates times where rain rate is increasing which is indicative of rainfall initiating. In this study's definition, rainfall is not initiated if the rain rate is light, therefore the second condition becomes necessary to exclude light rainfall. After sensitivity testing a wide range of rain rate thresholds, 1 mm/hr threshold was found to effectively capture the diurnal rainfall initiation over both land and ocean (Text A.1, Fig. A.4).

Based on these conditions, the difference in diurnal rainfall initiation timing between NCRF and CTRL is shown (Fig. 2.2). These results reveal a strong skew towards NCRF initiating rainfall before CTRL over land, with a weaker skew over ocean. Rainfall initiation timing difference is also computed at each major island, which all showed, on average, earlier initiation in NCRF compared to CTRL (Borneo: -0.32 hr, Sumatra: -0.42 hr, Malay Peninsula: -0.56 hr, Sulawesi: -0.76 hr, Java: -0.96 hr). These results suggest that diurnal rainfall initiation over the MC land is more sensitive to cloud-radiative interactions than over ocean, initiating earlier when cloud-radiative interactions are turned off.

Earlier rainfall initiation over land may influence the timing and strength of offshore propagation of convection. Therefore, changes in offshore propagating convective signals with respect to coastal distance are examined over the three regions depicted in Fig. 2.1b (A, B, C) that have intense convection over land and offshore propagating signals in CTRL (Fig. A.5). The Hovmöller diagrams depict the diurnal evolution of rain rate over each region as a function of distance from the coast in CTRL (Fig. 2.3a,c,e), along with the standardized rain rate difference between NCRF and

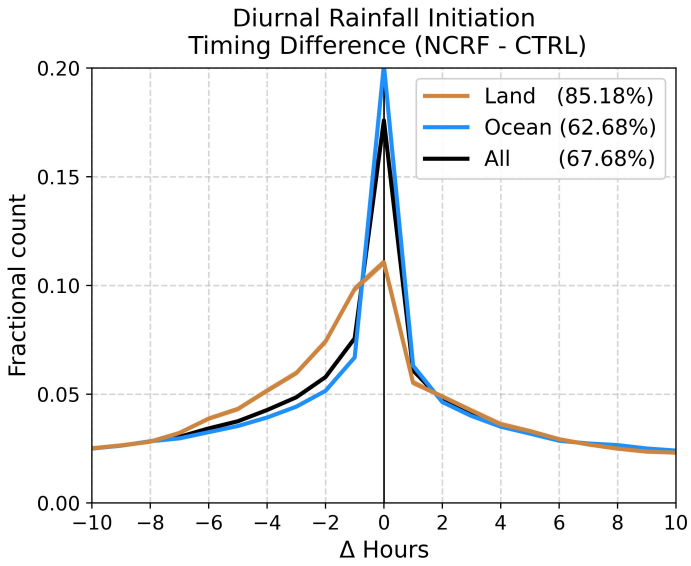

Figure 2.2: The frequency distribution of the difference in diurnal-composite rainfall initiation timing in hours between NCRF and CTRL over ocean (blue), land (orange), and all (black). Rainfall initiation is defined for a given grid point where the rain rate time tendency is positive and rain rate exceeds 1 mm/hr. The solid vertical black line indicates the timing difference of zero hours, where a negative difference indicates earlier convection initiation in NCRF. The values next to each domain in the legend indicate the percentage of domain points that met or exceeded our criteria for convective initiation.

CTRL (Fig. 2.3b,d,f). Standardized rain rate difference is calculated by subtracting CTRL diurnal rain rate from NCRF and dividing by the standard deviation of CTRL at each distance from the coast.

Over Sumatra (Fig. 2.3a,c), convection initiates over land between 10-12 LST, with rain rate maximizing at 16 LST in CTRL, which is consistent with the observed results in Yokoi et al. (2017) from the Pre-YMC field campaign (see their Fig. 5a). Rainfall propagates in two directions: following the phase speed lines, convection moves offshore at 18 LST at speeds around 3-5 m/s, while convection also moves inland at a faster speed of 10-12 m/s. Over Borneo Northwest (Fig. 2.3e), convection initiates onshore and propagates inland during the afternoon and early evening, with rain rates peaking over land at 21 LST. The convection then moves offshore around 06 LST, advancing at

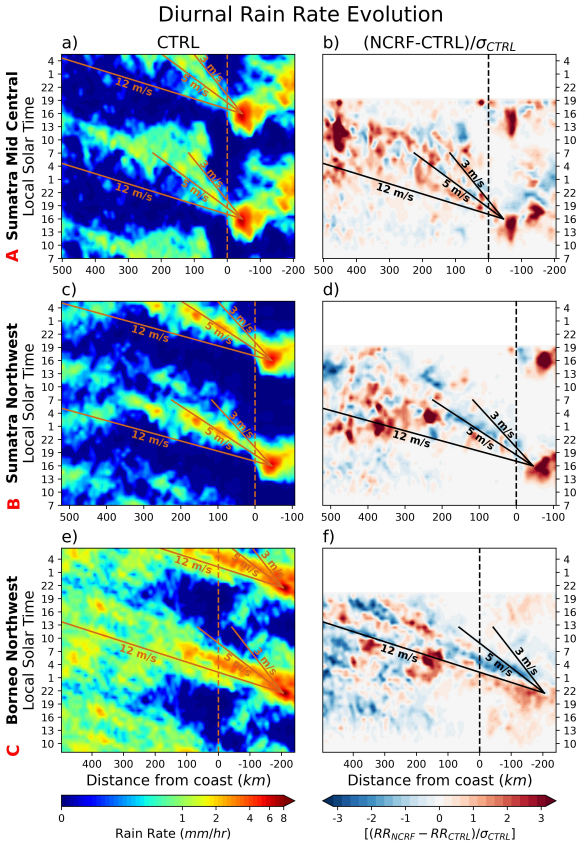

Figure 2.3: CTRL diurnal rain rate composite (mm/hr) is computed at the three regions from Fig. 2.1b, Sumatra Mid Central, Sumatra Northwest, and Borneo Northwest (a,c,e). The standardized rain rate difference of NCRF from CTRL is computed at each respective region (b,d,f), where reds indicate greater rain rate than CTRL, and blues indicate less. Positive/negative distances are offshore/onshore, with the vertical dashed brown and black lines representing the coastline and diagonal solid brown and black lines denoting a selection of phase speeds of offshore propagation. A 9 km (3-grid point) moving average is applied to the rain rates over the distance-from-coast dimension to smooth out the signal and isolate the most salient features.

a faster average speed (approximately 5–12 m/s) than over the Sumatran regions. In all three regions, NCRF produces stronger rain rates over land, and slightly stronger rain rates offshore (Fig. 2.3b,d,f). However, analysis of day-by-day tracking of offshore propagating signals reveals no statistically significant changes in phase speed between the simulations (not shown). These results suggest that while cloud-radiative interactions influence the intensity of rainfall, they do not have a statistically significant effect

on the speed of offshore propagating convection.

We further illustrate the changes in diurnal rain rate phase between CTRL and NCRF by plotting the frequency of the diurnal rain rate maximum phase difference between simulations (NCRF-CTRL) with respect to distance from coast over the MC (Fig. A.6). This analysis confirms an earlier maximum of rain rate over land and near the coastline ($\sim$150 km offshore) in NCRF, with nearly no difference farther offshore. In summary, we find significantly greater rain rates and earlier initiation of land convection in NCRF, with no statistically significant impact on offshore propagation speeds. The latter result suggests that cloud-radiative interactions and stronger land convection do not significantly influence previously discussed mechanisms of offshore propagation (i.e., land breezes and gravity waves).

2.3.2 Changes at the Surface due to Cloud-Radiative Interactions

Turning off cloud-radiative interactions directly affects the amount of solar radiative flux reaching the surface, which subsequently affects the atmosphere through surface turbulent heat and longwave radiative fluxes. The focus will be primarily on MC land, where the most significant changes in the diurnal cycle occur over land when cloud-radiative interactions are turned off. Figure 2.4a depicts this impact averaged over the MC land. In the absence of cloud-radiative interactions, an increase in sensible, latent, net surface shortwave ($SW_{down} - SW_{up}$), and net longwave flux ($LW_{down} - LW_{up}$) amplitude occurs. To provide context on how cloud fraction evolves with surface fluxes, the CTRL diurnal composite of pressure-weighted and level-averaged cloud fraction is plotted over three vertical levels of the atmosphere: 1) low-level (1000-700 hPa), 2) mid-level (700-450 hPa), and 3) high-level (450-200 hPa) (Fig. 2.4b). We utilize the

WRF variable output CLDFRA, which uses cloud water as a prognostic variable and a grid-scale dependent (land vs. ocean) relative humidity threshold. While this method does not distinguish between cloud types, it provides a general understanding of which cloud levels influence the diurnal cycle of convection. Results show that CTRL low-level cloud fraction is more in-phase with surface shortwave flux than mid- and high-level clouds, which maximize near or after sunset.

The amplitude of latent and sensible heat flux is higher without cloud-radiative interactions, driven by the increase in surface shortwave flux. There is also a one-hour phase shift (later peak) in the surface shortwave flux without cloud-radiative interactions, which likely explains the phase shifts in the surface latent and sensible heat flux. The later and stronger peak of surface shortwave flux in NCRF can be understood by noting the diurnal evolution of low-level cloud fraction, which dampens shortwave flux in CTRL around midday (Fig. 2.4b). The stronger latent and sensible heat fluxes in response to the stronger shortwave flux destabilize the boundary layer earlier and more intensely, leading to earlier initiation of rainfall and more intense rain rates, which is explored next (Fig. 2.1,2.2).

To directly tie rain rates to surface forcing, we calculate the joint frequency distribution of diurnal ranges in surface shortwave vs. sensible heat flux over land, along with the averaged diurnal rain rate range in each bin for both simulations (Fig. 2.5a,b). The frequency distribution is concentrated over a narrower range of higher diurnal shortwave flux range in NCRF than CTRL due to the absence of cloud-radiative interactions. NCRF also shows increasing diurnal rain rate range with increasing shortwave and sensible flux range (Fig. 2.5a). This result suggests that a strong relationship exists between surface forcing and rain rate in NCRF, where the diurnal rainfall is higher over regions with higher surface forcing. However, with the inclusion of cloud-radiative interactions in CTRL, diurnal rain rate range maximizes where sensible and shortwave

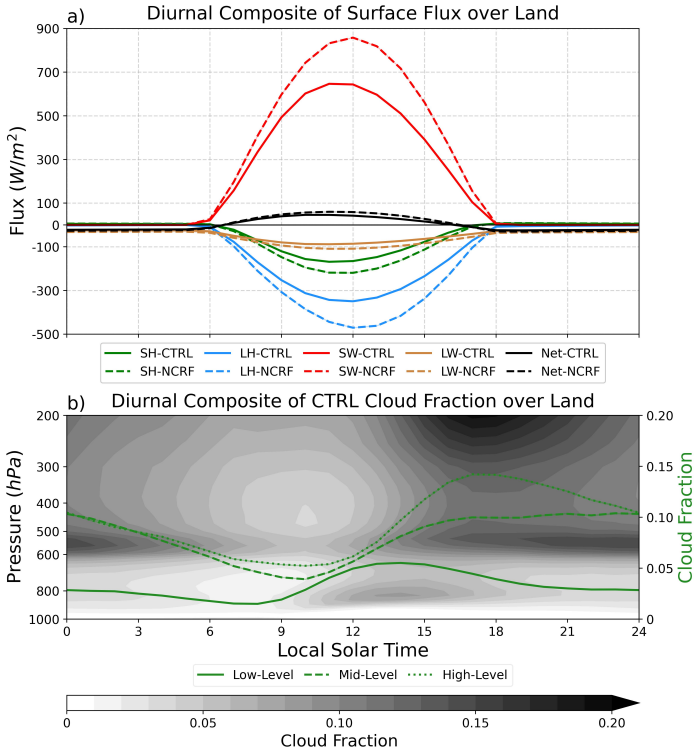

Figure 2.4: a) The diurnal composite of surface flux (W/m^2) averaged over land for both CTRL (solid) and NCRF (dashed), with sensible heat flux (SH, green), latent heat flux (LH, blue), net shortwave radiative flux (SW, red), net longwave radiative flux (LW, orange), and their sum ($SH + LH + SW + LW$, Net, black). These values are positive downward, indicating energy input towards the surface. b) The diurnal composite of CTRL cloud fraction over land is shown w.r.t. pressure (left y-axis) in the shading, and the pressure-weighted and level-averaged low (1000-700 hPa, solid), mid (700-450 hPa, dashed), and high (450-200 hPa, dotted) cloud fraction is overlaid (right y-axis).

surface flux ranges minimize, albeit with a smaller fraction of points (Fig. 2.5b). This result implies that surface shortwave flux more directly and locally controls rain rate range in NCRF, while a less clear relationship exists in CTRL due to the drop in surface shortwave flux from cloud shading.

To shed light on why CTRL maximizes in rain rate range when surface forcing range minimizes, opposite to NCRF, the average CTRL low-level cloud fraction diurnal range and terrain height are plotted with respect to the shortwave and sensible heat flux di-

urnal range (Fig. 2.5c). CTRL exhibits the strong albedo effect of low-level clouds over the regions that exhibit high rain rate range, suggesting that frequent low-level cloud coverage is responsible for the weaker surface flux ranges (Fig. 2.5c). The high fraction of low-level clouds reduces the influence of thermodynamic forcing from surface fluxes, however, rain rates still reach their maximum when surface fluxes minimize. The alignment of terrain height contours with the range of low-level cloud fraction is consistent with the expected role of anabatic winds over elevated terrain, enhancing low-level cloud formation. While the high fraction of low-level clouds suppresses surface fluxes, the anabatic winds support convective triggering through both adiabatic cooling and convergence around mountain peaks, thereby supporting the high rain rates observed in CTRL (Fig. 2.5c). Analysis where mid- and high-level cloud fraction range is substituted in place of low-level cloud fraction range showed a weaker relationship with terrain height or shortwave flux range. To better understand this terrain height dependency, we analyze variables with respect to terrain height in the next section.

2.3.3 Terrain's Influence on the Diurnal Cycle

The diurnal relationship between CTRL cloud fraction and surface shortwave cloud-radiative forcing (CRF) with respect to terrain height is shown (Fig. 2.6). Surface CRF quantifies the cloud-radiative effect by taking the difference of the surface radiative forcing between all-sky (includes cloud-radiative interactions) and clear-sky (excludes cloud-radiative interactions) forcing, where negative values indicate a cooling effect from clouds.

Figure 2.6 shows how the diurnal cycle of surface shortwave CRF and cloud fraction evolves at different terrain heights in CTRL. Surface shortwave CRF decreases with terrain height, suggesting stronger cloud-radiative influences at higher terrain heights. A clear diurnal signal for all three cloud levels exists at all terrain heights, albeit

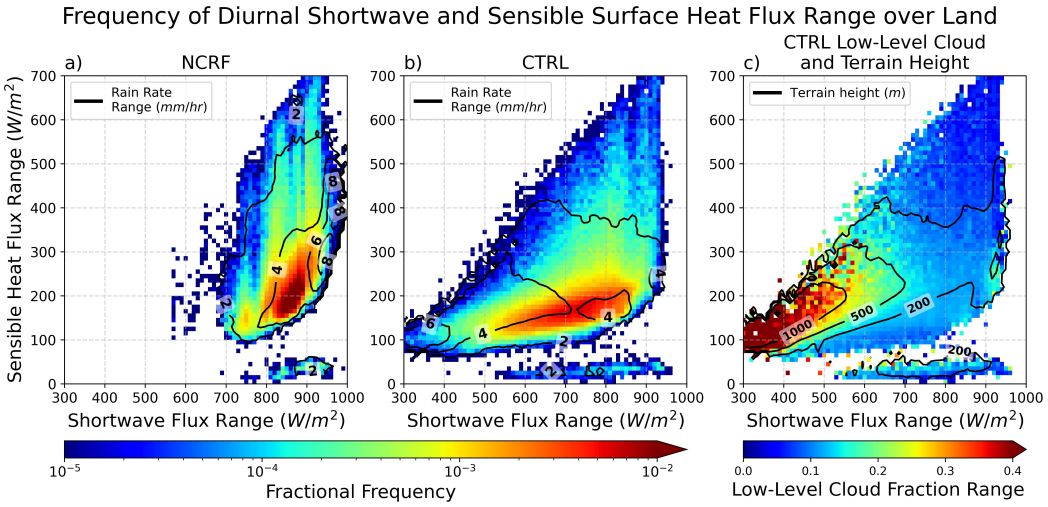

Figure 2.5: The fractional frequency of occurrence of the diurnal range of shortwave and sensible surface flux (shading) for NCRF (a), CTRL (b), normalized such that the sum over the x and y dimensions equals one. The average rain rate diurnal range is overlaid (contour) after smoothing using a 5-bin center-average (black, mm/hr). (c) The low level-average cloud fraction diurnal range (1000-700 hPa, shading) and terrain height (m, contour) is plotted for CTRL.

at lower amplitudes at the lowest terrain heights. Additionally, there is an earlier increase in cloud fraction at higher terrain heights. Low-level cloud fraction has the highest diurnal variability at the highest terrain heights and the strongest in-phase relationship with surface shortwave CRF (Fig. 2.6a). Mid- and high-level clouds have greater cloud fraction at lower terrain heights compared to low-level cloud fraction (Fig. 2.6b,c). Mid- and high-level cloud fraction peaks after maximum solar insolation at all terrain heights, limiting their shortwave CRF impact to later in the day. In contrast, low-level cloud fraction increases earlier and persists throughout the day over higher terrain, strongly inhibiting surface warming via the cloud-albedo effect.

Burleyson et al. (2015) attempted to quantify the diurnal cloud-radiative effect by cloud type over Darwin, Australia, and found that low and deep convective cloud types had the most impact on surface shortwave CRF. Our own analysis of the relationship between cloud-level fraction and surface shortwave CRF confirms that low-level clouds

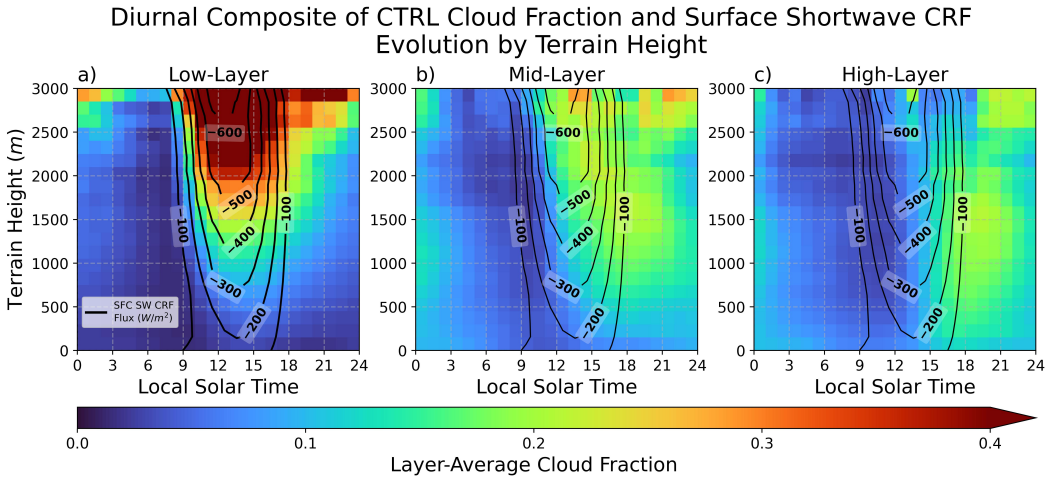

Figure 2.6: The CTRL diurnal composite evolution in local solar time of low (a, 1000-700 hPa), mid (b, 700-450 hPa), and high (c, 450-200 hPa) pressure-weighted and level-averaged cloud fraction as a function of terrain height (m) is plotted. The surface shortwave CRF (W/m^2) is overlaid as a contour (black), with increasingly negative values indicating stronger cloud-radiative cooling at the surface.

more strongly influence surface shortwave flux compared to mid- and high-level clouds (Fig. A.7). These results point to a clear terrain-dependent radiative response, primarily driven by frequent low-level cloud cover over higher terrain, where the diurnal range of surface shortwave and sensible heat fluxes are small in CTRL (Fig. 2.5b).

To more closely assess the terrain-height dependence of rain rate intensity, we compute the joint frequency distribution of diurnal rain rate range and terrain height (Fig. 2.7). Because the number of samples decrease with increasing terrain height (Fig. 2.7d), the frequency plots are normalized by the sample count at each terrain height bin to enable comparison across terrain heights. Both NCRF and CTRL initially show increasing diurnal rain rate range with increasing terrain height (Fig. 2.7a,b). However, CTRL and NCRF rain rate range eventually plateaus at a terrain height of 1500 m and 1700 m respectively, with CTRL decreasing in rain rate range above 2100 m (Fig. 2.7b). The difference in rain rate range between NCRF and CTRL highlights the increasing rain rate range difference with increasing terrain height between the

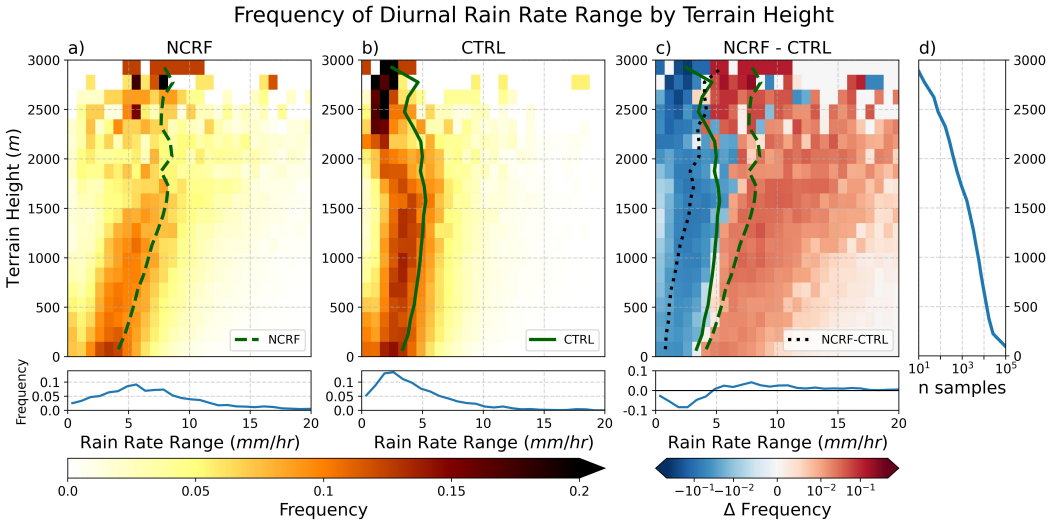

Figure 2.7: The frequency distribution of the diurnal range of rain rate (mm/hr) versus terrain height (m) over land, normalized by the terrain height bin, for NCRF (a), CTRL (b), and their difference (NCRF-CTRL) (c). Corresponding average rain rate range (green) at each terrain height bin is overlaid for NCRF (dashed), CTRL (solid), and their difference (black, dotted). Terrain averaged frequency (a, b) and anomalous frequency (c) of rain rate range is plotted below the heat maps (blue, solid). The number of terrain height samples at each terrain height bin is plotted (d) (blue, solid).

simulations, where the average NCRF diurnal rain rate range above terrain heights of 750 m is 50% greater than CTRL (Fig. 2.7c). As shown in Fig. 2.6a, low-level clouds more frequently cover regions of higher terrain heights, which decreases surface shortwave flux range in CTRL. Together with Fig. 2.7, these results suggest that cloud-radiative interactions, primarily from low-level clouds over high terrain, decrease surface shortwave forcing, resulting in less intense rainfall at higher terrain heights in CTRL.

2.3.3.1 The Terrain-Dependent Diurnal Surface Flux Response

To quantify the dependence of surface fluxes on terrain height, Fig. 2.8 shows how the average diurnal range of each surface flux component changes with terrain height. In CTRL (Fig. 2.8b), the range of surface shortwave flux (SW) decreases with increas-

ing terrain height due to increasing low-level cloud cover (Fig. 2.5c), which decreases incoming surface shortwave flux through the cloud-albedo effect. In the absence of cloud-radiative interactions, NCRF (Fig. 2.8a) exhibits slightly increasing SW with terrain height, likely due to the thinner atmosphere at higher elevations, leading to less clear-air attenuation of shortwave radiation. The difference in SW between NCRF and CTRL (Fig. 2.8c) therefore strongly increases with terrain height, which directly increases the surface latent and sensible heat fluxes.

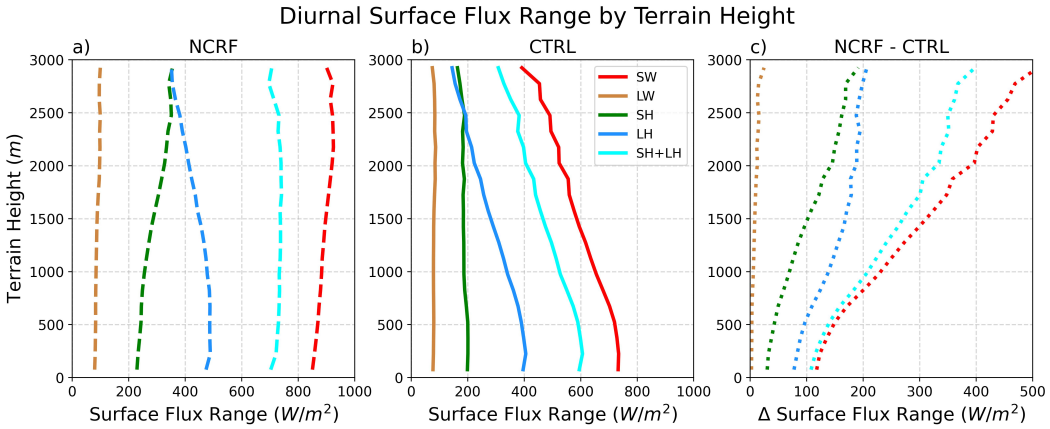

Figure 2.8: The average profiles of diurnal range of surface flux as a function of terrain height over land for NCRF (a), CTRL (b), and their difference (NCRF-CTRL) (c). Surface shortwave (SW, red), longwave (LW, brown), sensible (SH, green), latent (LH, blue), and the sum of sensible and latent (SH+LH, cyan) fluxes are shown.

The range of surface latent heat flux (LH) decreases with increasing terrain height for both simulations (Fig. 2.8a,b), with a greater decrease in CTRL than NCRF. The slower decrease of LH with increasing height in NCRF relative to CTRL can be linked to the greater diurnal soil moisture maximum at the top layer (0-0.1 m) of soil in NCRF compared to CTRL (Fig. A.8). A moister land surface in NCRF can enhance the evaporation of water at the surface, resulting in a higher LH compared to CTRL. The higher soil moisture values in NCRF compared to CTRL can be attributed to the higher rain rates over higher terrain heights in NCRF (Fig. 2.5b).

The range of surface sensible heat flux (SH) slightly decreases with increasing terrain height for CTRL, while it increases for NCRF. For a given wind speed, SH is a function of the disequilibrium between surface temperature and atmospheric temperature ($T_s - T_2$), where T_s represents the surface skin temperature and T_2 represents the atmospheric temperature at 2 m. Figure A.9 demonstrates nearly no change in this disequilibrium with increasing terrain height in CTRL, whereas in NCRF, it increases with terrain height because the rate of decrease of T_s with height is reduced. Greater T_s at higher elevation can be explained by the much greater surface shortwave flux with terrain height in NCRF than CTRL (Fig. 2.8c). The greater T_s at higher elevations in NCRF also explains why the range of surface longwave flux (LW) increases slightly more than CTRL (Fig. 2.8c).

The increasing difference of all surface flux ranges with increasing terrain height between simulations (Fig. 2.8c) illustrates how the absence of cloud-radiative interactions alters the thermodynamic environment, with a strong dependence on terrain height. These results help explain why the diurnal rain rate range difference is greatest over regions of high terrain when cloud-radiative interactions are removed (Fig. 2.1). These results do not account for changes in dynamics, which are explored next.

2.3.3.2 Orographically Enhanced Diurnal Lifting

To assess how these terrain-dependent thermodynamic changes at the surface affect circulation, Fig. 2.9 depicts the joint frequency distribution of diurnal orographically forced surface vertical motion (hereafter, simply "slope flow") range and terrain height. Slope flow is calculated following Luo and Yanai (1983) method,

$$w_{10} = \nabla h \cdot \vec{U} \tag{2.1}$$

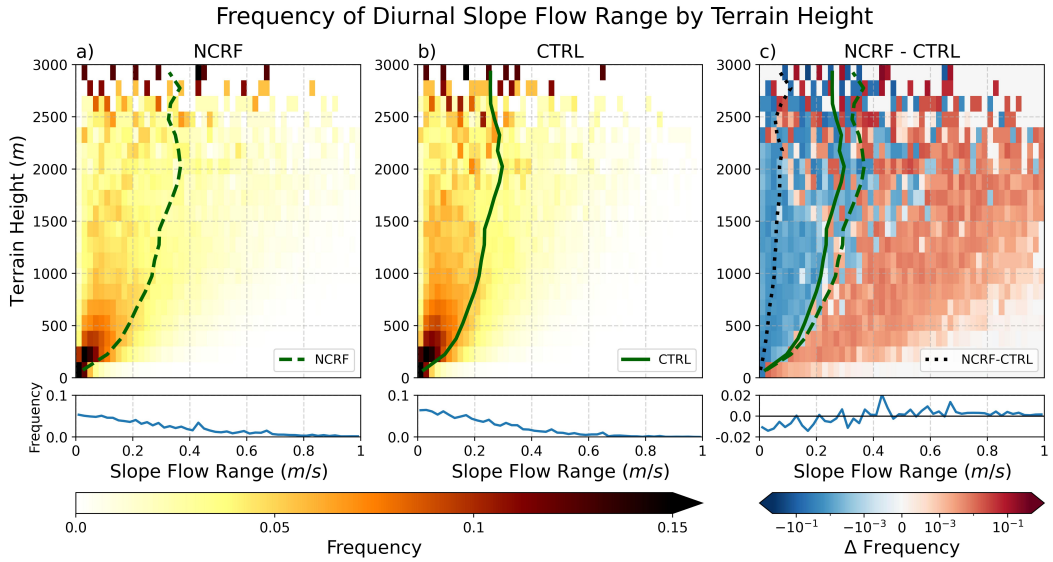

Figure 2.9: The frequency distribution of the diurnal range of surface (10-m) slope flow (m/s) as a function of terrain height (m) over land, normalized by the terrain height bin, for NCRF (a), CTRL (b), and their difference (NCRF-CTRL) (c). Corresponding average slope flow range (green) at each terrain height bin is overlaid NCRF (dashed) in a), CTRL (solid) in b), and their difference (black, dotted) in c). Terrain averaged frequency (a, b) and anomalous frequency (c) of slope flow range is plotted below the heat maps (blue, solid).

where h represents the terrain height (m), $\vec{U}$ represents the 10-m surface horizontal winds (m/s), and w_{10} represents the 10-m slope flow (m/s). While land-sea breezes may contribute to the diagnosed slope flow near the coastline, we expect this flow to be dominated by diurnal anabatic and katabatic winds.

The results show that both simulations exhibit an increase in slope flow range with terrain height (Fig. 2.9a,b). It is important to note that a positive linear relationship exists between terrain height and terrain slope over the MC, such that grid points over higher terrain are also more sloped than low terrain grid points (Fig. A.10). This positive relationship helps explain why diurnal slope flow range increases with terrain height in general: steeper terrain slopes lead to stronger buoyancy-driven diurnal katabatic and anabatic winds.

The diurnal slope flow range difference between the simulations (black, dotted) in-

creases with terrain height (Fig. 2.9c), suggesting that the absence of cloud-radiative interactions enhances the anabatic and katabatic winds. The diurnal slope flow range is split into the maximum and minimum components to investigate the individual contribution to the range (Fig. A.11). The difference between NCRF and CTRL show both the minimum (downslope/katabatic) and maximum (upslope/anabatic) winds grow stronger in NCRF with increasing terrain height. However, as terrain height increases, upslope winds contribute more to the range than downslope winds in NCRF (Fig. A.10a), suggesting that cloud-radiative influences on daytime upslope winds are more impactful to the range than nighttime downslope winds. The enhanced diurnal cycle of slope flow in NCRF is consistent with the enhanced surface shortwave, latent, and sensible flux forcing compared to CTRL (Fig. 2.8c). We also see a similar terrain dependence of diurnal surface divergence range (Fig. A.12), consistent with the interpretation that surface heating along the sloping terrain increases the diurnal cycle of low-level vertical motion.

To visualize how the diurnal coastal surface flow changes in association with the slope flow, the diurnal composite of CTRL 10-m wind speed at the average time of maximum diurnal upslope flow over land (14 LST) and maximum diurnal downslope flow over land (6 LST) is compared (Fig. A.13), where the magnitude and vector difference of surface winds are taken between NCRF and CTRL (Fig. 2.10). During the time of maximum diurnal upslope flow over land, prominent onshore flows, contributed from both sea breezes and anabatic flows, can be seen in the afternoon (Fig. 2.10a) due to the strong warming of the land-surface and sloped terrain by incoming shortwave flux. NCRF produces stronger onshore winds over the entirety of the MC compared to CTRL, likely due to the higher surface shortwave flux (Fig. 2.10b).

During the time of minimum diurnal upslope flow over land, offshore winds from the land breeze and katabatic flows manifest due to the nocturnal cooling of the land-

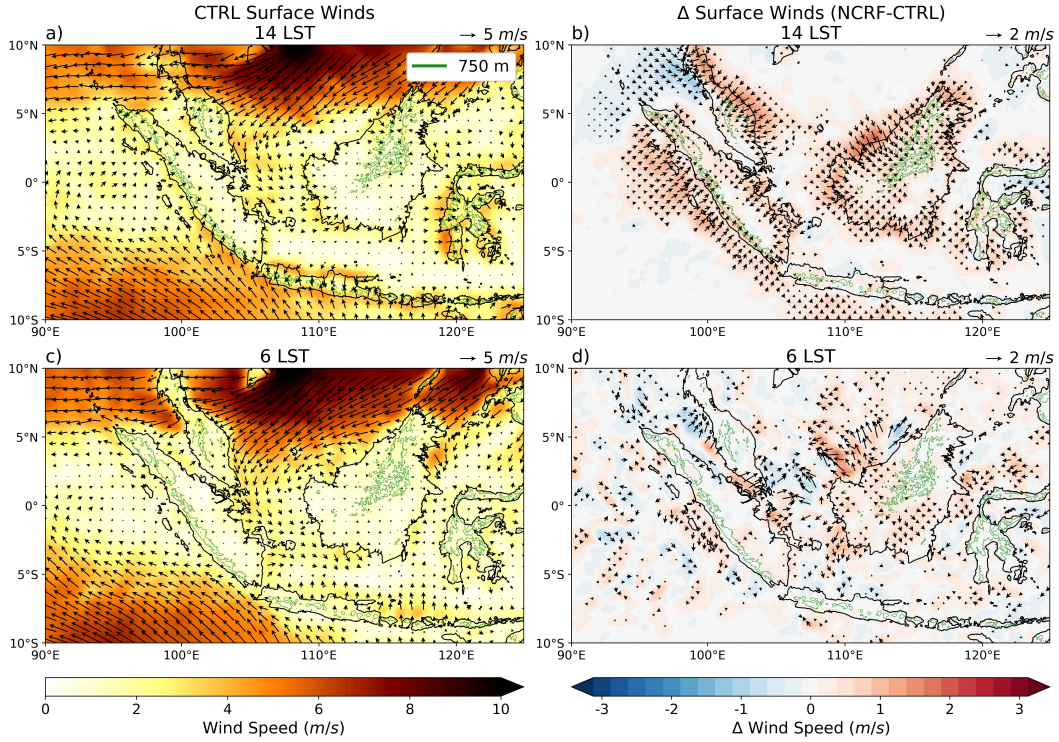

Figure 2.10: The diurnal composite of CTRL 10-m wind speed (m/s) is plotted at times of maximum 10-m convergence over land (14 LST) (a) and ocean (6 LST) (c) after a 30 grid-point center point average, with arrows representing the wind direction. The wind speed difference (NCRF-CTRL) is shaded at the same times (b, d), where reds indicate stronger magnitude winds in NCRF, while blues indicate the opposite. The arrows represent the wind vector difference between NCRF and CTRL, where scaling of the arrows differ between the left and right column subplots. Arrows are not included where the magnitude of the wind speed difference (b, d) did not exceed 0.25 m/s. Terrain height at 750 m is overlaid in solid green.

surface (Fig. 2.10c). During this time, NCRF and CTRL do not have a clear signal of differing surface winds (Fig. 2.10d). These results suggest that cloud-radiative interactions influence the daytime diurnal flows more than the nighttime flows. Since offshore convection propagates at varying local times across the MC (Fig. 2.3), alternative times were used in place of 6 LST; however, this did not qualitatively affect our results. This result corroborates our previous findings of an insignificant change in offshore propagation speed between the simulations. However, the less organized and significant difference in wind speed at night could be related to model divergence or

background state drift between CTRL and NCRF, and/or boundary-level dynamics or nighttime stability, so future research should attempt to isolate the nighttime influence of cloud-radiative interactions without the influence from the daytime. Nevertheless, the contrast between CTRL and NCRF highlights the role of the cloud-radiative effects in shaping the distribution of the surface energy balance across the varying terrain heights over the MC, contributing to an increase in diurnal rainfall by enhancing sea breezes and anabatic flows.

2.4 Conclusions

The latest GCMs continue to struggle with accurately predicting the peak timing and intensity of the diurnal cycle of rainfall, with implications for the prediction of large-scale climate. These longstanding challenges underscore our need to improve our fundamental understanding of the diurnal cycle of convection. Here we investigate how cloud-radiative interactions influence the diurnal cycle of rainfall over the Maritime Continent (MC) using a convection-permitting model, improving our understanding of their impact on convection over regions of complex islands and steep terrain.

The background setting of our study is a period in late 2015, during the wet season, when conditions of large-scale easterly flow favored enhanced diurnal rainfall over the islands of the MC, with prominent signatures of nocturnal offshore propagation. The simulations were performed using the WRF model (v4.3.3), with a convection-permitting inner domain (3-km grid spacing) over a 10.5-day period. To test the sensitivity of the diurnal cycle of rainfall to the removal of cloud-radiative interactions, an ensemble of nine 36-hour sensitivity simulations was conducted in which cloud-radiative interactions were disabled (NCRF). Each NCRF run was initialized daily at approximately local sunrise (0000 UTC) as a model restart from a continuous 10.5-day

control simulation (CTRL). Our experiment took place during an MJO suppressed phase, but the model experiment was repeated during the enhanced phase of the same MJO, yielding consistent results compared to the suppressed phase (Fig. A.3). Therefore, we can be more confident that our results are not highly sensitive to MJO phase, but may not be generally applied during all seasons or backgrounds states.

We found that the removal of cloud-radiative interactions led to an increase in diurnal rainfall range over the MC land (34%) and ocean (7%). Additionally, diurnal rainfall initiated earlier, with the greatest magnitude change over the MC land. More intense and earlier-triggered diurnal rainfall also occurred over coastal and offshore regions, characterized by strong signals of offshore rainfall propagation. The speed of offshore rainfall propagation did not significantly change when cloud-radiative interactions were absent. The limited sensitivity of diurnal rainfall over the ocean and offshore-propagating rainfall to the removal of cloud-radiative interactions highlights the need for future work to isolate oceanic cloud-radiative effects and their contribution to nocturnal rainfall over the MC.

The diurnal rain rate range difference between NCRF and CTRL increased markedly with terrain height, where the average NCRF diurnal rain rate range above terrain heights of 750 m is 50% greater than CTRL. These results suggest that diurnal rainfall is more sensitive to cloud-radiative interactions at higher terrain heights. This increase resulted from the increasing difference in surface forcing (shortwave, longwave, sensible heat, and latent heat fluxes) with terrain height between NCRF and CTRL. The additional thermodynamic surface forcing at higher terrain in NCRF induced a stronger response in orographically forced surface vertical motion through enhanced anabatic winds and sea breezes. A less clear cloud-radiative influence was seen on katabatic winds and land breezes during the night.

Topographically-induced clouds were found to be essential to the terrain-dependency

described above. In CTRL, low-level clouds significantly reduce surface shortwave flux, more strongly than mid- and high-level clouds, due to their reflective properties (the cloud-albedo effect) and their more in-phase relationship with insolation. Mid- and high-level cloud coverage peaks after maximum insolation at all terrain heights, limiting their shortwave CRF impact to later in the day, while low-level cloud coverage maximizes closer to maximum insolation. Low-level cloud coverage was also the highest over regions of higher terrain, strongly dampening the thermodynamical surface forcing. The implication of this finding is that cloud–radiative interactions, such as the cloud-albedo effect, weaken buoyancy-driven diurnal anabatic winds, ultimately reducing rainfall intensity over higher and steeper terrain across the MC.

The results from this study suggest that cloud-radiative interactions are a critical component to accurately predicting the timing and strength of the diurnal cycle of rainfall in this region. Specifically, the decrease in surface shortwave flux from cloud-radiative interactions strongly influences the surface sensible and latent heat flux, with substantial impact on diurnal mesoscale circulations and rainfall. Therefore, regions with early initiating and persistent cloud cover during the day, particularly from low-level clouds, need to be carefully considered, as errors in the representation of cloud-radiative interactions can significantly modulate diurnal rainfall patterns.

Our study corroborates the findings of an observational study by Forsythe et al. (2015), indicating that mountainous regions are highly sensitive to radiative forcing and its modification by clouds due to their elevated cloud coverage during the day. This study identifies key mechanisms that alter the diurnal cycle of rainfall over the MC, underscoring its complexity and highlighting opportunities for deeper investigation of the diurnal cycle in GCMs. Past studies have attributed GCM deficiencies in diurnal rainfall to limitations in convective parameterizations (Wang et al., 2020; Tang et al., 2022; Dong et al., 2023; Tao et al., 2024). In our study, removing cloud-radiative

interactions led to changes in the diurnal cycle of rainfall that resemble common GCM deficiencies (i.e., overly frequent triggering and early rainfall onset). This result therefore suggests the potential importance of erroneous representation of cloud-radiative interactions, especially associated with low-level clouds over high terrain, in either partially explaining or exacerbating these deficiencies in GCMs.

Chapter 3

Understanding the Environmental Influence of the Madden-Julian Oscillation on the Behavior of the Diurnal Cycle over the Maritime Continent

3.1 Introduction

The Madden-Julian Oscillation (MJO; Madden and Julian, 1971) is the dominant mode of intraseasonal variability in the tropics, modulating large-scale circulation, moisture, convection, and precipitation globally and locally over the Maritime Continent (MC) (Jiang et al., 2020). The diurnal cycle of rainfall explains the majority of rainfall variability over the MC Kikuchi and Wang (2008), and recent studies have shown that its strength and spatial distribution over land and ocean is strongly modulated as the MJO propagates across the region (Ichikawa, 2006; Qian, 2020; Zhou et al., 2022; Bai and Schumacher, 2022; Ling et al., 2019), however, the mechanisms responsible for the changes remain uncertain. Despite the importance of the MJO and the diurnal cycle of convection along the MC, general circulation models (GCMs) and higher-resolution numerical models continue to struggle in accurately representing the MJO and the diurnal cycle of convection (Chen et al., 2022).

The diurnal cycle of rainfall remains a persistent source of model bias, with errors in its timing, intensity, and spatial distribution (Yin and Porporato, 2017; Tang et al., 2021; Dong et al., 2023), limiting the reliability of projections of freshwater availability, the global radiation budget, and large-scale atmospheric circulation (Matus and

L'Ecuyer, 2017). Improving our understanding of the mechanisms through which the MJO modulates the MC diurnal cycle may therefore provide a pathway toward improving model representation of both phenomena (Ling et al., 2019; Zhou et al., 2025). To address this gap, this study investigates how MJO-induced changes in environmental conditions influence the land–ocean distribution of diurnal rainfall across the western MC using high-resolution, convection-permitting sensitivity experiments.

The diurnal cycle of rainfall's land-sea contrast and its spatial distribution over the MC islands modulates with the propagation of the MJO. Over the MC, island and oceanic diurnal rainfall exhibit opposing intraseasonal behavior, with island rainfall peaking ahead of the MJO enhanced phase and weakening thereafter, while oceanic rainfall maximizes when the MJO enhanced phase is overhead (Peatman et al., 2014; Sakaeda et al., 2017; Coppin and Bellon, 2019; Ling et al., 2019; Oh et al., 2012). Additionally, the spatial distribution of diurnal rainfall over some of the larger islands shifts from one terrain face to the other (i.e., western-to-eastern facing) as the MJO propagates through the region (Ichikawa, 2006; Qian, 2020; Zhou et al., 2022; Bai and Schumacher, 2022; Sakaeda et al., 2020). Recent studies have also linked the successful propagation of the MJO over the MC to the strength of the land-sea contrast in the diurnal cycle of rainfall (Zhang and Ling, 2017; Ling et al., 2019), however the mechanisms underlying these observed features of diurnal rainfall remain uncertain.

A mechanism that remains unexplored is the increasing influence of cloud-radiative interactions on suppressing land diurnal rainfall during the propagation of enhanced phase of the MJO over the MC. As shown in chapter 2, cloud-radiative effects suppress diurnal rainfall more strongly over land than ocean; therefore, as cloud cover increases with the onset of the MJO enhanced phase over the MC, the observed increasing land–ocean contrast in diurnal rainfall may be explained by cloud-radiative interactions.

To capture the intraseasonal influence cloud-radiative interactions have on diurnal rainfall over the MC, we have performed an ensemble of sensitivity experiments in which cloud-radiative interactions are disabled when the enhanced phase of the MJO is over the MC, following the same methodology and MJO event described in Chapter 2.2.2. This MJO event was slightly unique because the magnitude of diurnal rainfall over land slightly increased from when the MJO enhanced phase is over the Indian Ocean to over the western MC (PreMJO-to-MJO), despite the increase in cloud cover and resulting reduction in surface fluxes. This suggests that while cloud-radiative effects dampen land diurnal rainfall from PreMJO-to-MJO, other processes must sustain it on the intraseasonal time scale. Additionally, the cloud-radiative effect on oceanic diurnal rainfall is much weaker compared to the intraseasonal change, indicating that, while cloud-radiative interactions affect diurnal rainfall over land and ocean, they are not the primary driver of the intraseasonal change in the land-sea distribution of diurnal rainfall over the MC. This conclusion suggests that the MJO modulates other environmental conditions along its propagation over the MC that are more responsible for the intraseasonal change in diurnal rainfall over the MC.

Several mechanisms have been proposed to explain the intraseasonal evolution of the Maritime Continent diurnal cycle. Some studies argue that the islands ultimately compete against oceanic convection, therefore the suppression of convection over land will inherently enhance oceanic convection (Oh et al., 2012; Ling et al., 2019; Zhou et al., 2025), while others suggest more favorable environmental conditions over ocean, such as a moister environment, enhances oceanic convection over the MC (Zhang and Ling, 2017). It is likely that the suppression of land and enhancement of oceanic convection both play a role in the intraseasonal evolution of diurnal rainfall, but the mechanisms responsible and their relative contribution remains unclear. More recent studies examining the intraseasonal evolution of rainfall over land attribute the western-

to-eastern terrain facing shift in the spatial distribution of diurnal rainfall to the dynamical wind response from the onset of the MJO or other large-scale wind patterns (Zhou et al., 2022, 2023; Qian et al., 2010, 2013). Furthermore, idealized studies have demonstrated that stronger background winds suppress island-wide diurnal convection, particularly on the windward side, likely through enhanced coastal mixing that weakens the land–sea temperature gradient and thereby reduces onshore flow strength (Wang and Sobel, 2017; Natoli and Maloney, 2023b). The vast majority of the mechanisms that have been suggested to modulate the diurnal cycle of rainfall over the MC are strongly influenced by the background environmental conditions, such as moisture and wind.

The MJO modulates environmental moisture and lower-tropospheric winds, directly influencing the key mechanisms that govern tropical diurnal convection. As the enhanced phase of the MJO propagates over the MC, atmospheric moisture deepens into the mid-to-upper troposphere and anomalous easterlies reverse to westerlies. In regards to how atmospheric moisture can effect diurnal rainfall over the MC, a well-known relationship exists between moisture availability and tropical oceanic rainfall, where an increase in atmospheric moisture is associated with an exponential increase in rainfall (Bretherton et al., 2004). This relationship is weaker over land (Hohenegger and Stevens, 2022; Schmidt and Hohenegger, 2024), which could explain the growing land-sea contrast in diurnal rainfall with the onset of the MJO enhanced phase. Lower-tropospheric easterly flow can enhance convection on the leeward side while suppressing on the windward side over the MC islands, helping to explain the changing spatial distribution of rainfall over land with the reversal of anomalous easterlies to westerlies upon the onset of the MJO enhanced phase (Ichikawa, 2006; Wang and Sobel, 2017; Sakaeda et al., 2020; Natoli and Maloney, 2023b). Previous studies have suggested the mechanism responsible for the changing spatial distribution of island diurnal rainfall

is the weakening land-sea thermal-gradient through enhanced mixing on the windward side that suppresses sea-breeze driven convection (Wang et al., 2020; Qian et al., 2013; Qian, 2020; Natoli and Maloney, 2023b). Despite the documented impact large-scale moisture and circulation has on the mechanisms that influence diurnal convection over the MC, the relative role of each environmental forcing associated with the MJO on diurnal convection has not been explicitly tested before.

Utilizing a convection-permitting model and a set of novel experiments, we isolate the MJO induced moisture and circulation change over the MC into their individual and combined contribution to the intraseasonal change of diurnal rainfall over the MC land and ocean. In this study, we address these two questions: 1) What are the relative influences of the MJO's large-scale moisture and circulation profile on the diurnal cycle of rainfall? 2) What are the mechanisms through which moisture and circulation influence diurnal rainfall?

3.2 Data and Methods

The MJO event we investigate occurred in the winter of 2015, which provided a well-documented and strong change in the diurnal cycle of convection over its lifetime (Yokoi et al., 2017). Below we will discuss the observed characteristics of this particular MJO and the changing diurnal cycle of rainfall over the western MC during the study period (November 23 to December 20, 2015). Additionally, we will discuss the methods we leverage to answer our stated questions, including model verification and the suite of novel experiments designed to isolate the effects of MJO-associated environmental moisture and circulation on the diurnal cycle of rainfall.

3.2.1 Case Background State

Based on the outgoing longwave radiation MJO index (OMI), the MJO event during the study period (November 23 to December 20, 2015) has an amplitude of less than 1 ($\bar{\mu} = 0.7$) over the Indian Ocean (Phase 2-3) between November 23 and December 03. The MJO strengthens to an amplitude greater than 1 ($\bar{\mu} = 1.75$) as it propagates over the MC (Phase 4-5) between December 10-20 (Kiladis et al., 2014). The Realtime Multivariate Madden Julian Index (RMM) provides a similar story, suggesting our study period consists of a strengthening MJO event that propagates from the Indian Ocean to the MC. During this MJO event, moderate easterlies over the MC transitioned into strong westerlies at 850-hPa, along with significant moistening of the troposphere between the the study periods (Fig. B.1).

Observational analysis of this MJO event over the western central coast of Sumatra by Yokoi et al. (2017) exhibit a strong diurnal cycle of rainfall that maximizes onshore at 15 local solar time (LST), and propagates offshore around 18-19 LST before the onset of the MJO enhanced phase. During the onset of the MJO enhanced phase, both offshore and onshore diurnal rainfall weakens, largely due to the strong westerly winds in the lower troposphere associated with the enhanced phase of the MJO. Yokoi et al. (2017) study is done over a relatively small region of the western MC, so extending this analysis across the broader western MC will provide a more comprehensive understanding of how MJO environmental conditions influence the diurnal cycle of rainfall at regional scales, motivating the model-based analysis presented in the following subsection.

3.2.2 Model Configuration

The Advanced Research Weather Research and Forecasting (WRF) model Version 4.3.3 is utilized in this study to run a pair of 10.5-day control (CTRL) simulations between

November 22 1200 UTC and December 03 0000 UTC when the MJO enhanced phase is over the Indian Ocean (PreMJO) and December 09 1200 UTC - 20 0000 UTC when the MJO enhanced phase is over the western MC (MJO), with the first 12 hours of the simulations removed to account for model spin-up (Skamarock et al., 2021). The WRF Model configuration for the CTRL simulation largely follows Najarian et al. (2025), which includes an outer domain of 12-km grid spacing with the Tiedtke cumulus scheme and an inner nest of 3-km grid spacing with explicit convection (Fig. A.1). The model has 55 vertical levels, with vertical spacing between levels increasing with height, a model top at 10 hPa, and output saved at an hourly frequency. Both domains use the WRF Double-Moment 6-class microphysics (Lim and Hong, 2010), RRTMG radiation (Iacono et al., 2008), and the Noah Land Surface Model (Ek et al., 2003). The fifth generation ECMWF atmospheric reanalysis (ERA5) data set is used to initialize and update boundary conditions for the models (Hersbach et al., 2020).

A deviation from Najarian et al. (2025) is made with the use of spectral nudging at an hourly timescale of winds (u,v) and moisture (q) in the outer domain (12-km), for long wavelengths (>1000 km), and excluding any nudging in the boundary layer. Our specific use of spectral nudging preserves the evolving large-scale MJO circulation and moisture anomalies over the outer domain, while allowing convection within the inner domain to develop without explicit nudging, resulting in a more realistic domain-average oceanic diurnal cycle of rainfall and improved representation of the MJO over the MC. To avoid resolution-induced numerical artifacts at the boundary of the inner nest, and to focus our analysis over the western MC region where the MJO enhanced phase propagates, analysis will be confined further within the inner nest (Fig. B.2, red rectangle).

3.2.3 Model Verification of Diurnal Rainfall Variability

To ensure the model simulates the observed intraseasonal shift in diurnal rainfall strength over land and ocean, the Integrated Multi- satellitE Retrievals for the Global Precipitation Measurement Mission (IMERG) version 7 satellite estimated rain rates at 30-minute and 0.1-degree resolution is leveraged to compare against PreMJO and MJO output (Huffman et al., 2023). Before comparisons are made, CTRL's spatial grid spacing is regridded to match IMERG using area-weighted averages, approximately conserving the spatial integral of precipitation during the remapping process, while IMERG is temporally aggregated to hourly resolution by averaging consecutive 30-minute samples. After converting coordinated universal time (UTC) to LST ($LST = UTC + (\lambda/15)$), where λ represents the longitude at each grid point, the domain average of the diurnal composite of rain rate and the the grid point diurnal range ($max - min$) is calculated and compared over land and ocean points (Fig. 3.1). We utilize IMERG's land mask metric for both datasets after regridding and found that defining land points as grid points with 75% water coverage or less, with all remaining grid points classified as ocean, best ensured coastal land regions were properly identified as land.

While the exact values of the domain average diurnal rain rate between CTRL and IMERG differ over land and ocean during the PreMJO and MJO periods, grid point diurnal range increases more over ocean than over land in both IMERG (23.3% and 4.9% respectively) and CTRL (30.1% and 5.5% respectively), suggesting the estimated shift in diurnal rainfall strength from PreMJO-to-MJO is well captured by CTRL over the MC region (Fig. 3.1a,b). The general spatial patterns of differences in the PreMJO-to-MJO spatial difference in diurnal rainfall range agree between CTRL and IMERG, with a clear signal of stronger diurnal rainfall over oceanic regions during the

MJO (offshore south of Java, the Java Sea, and offshore east of Borneo), with less clear agreement over land (Fig. 3.1c,d). These results indicate that the shift in diurnal rainfall from PreMJO-to-MJO for this MJO event is adequately represented over the western MC, allowing us to confidently conduct experiments built upon the CTRL simulations to test the MJO's environmental influence on the diurnal cycle of rainfall.

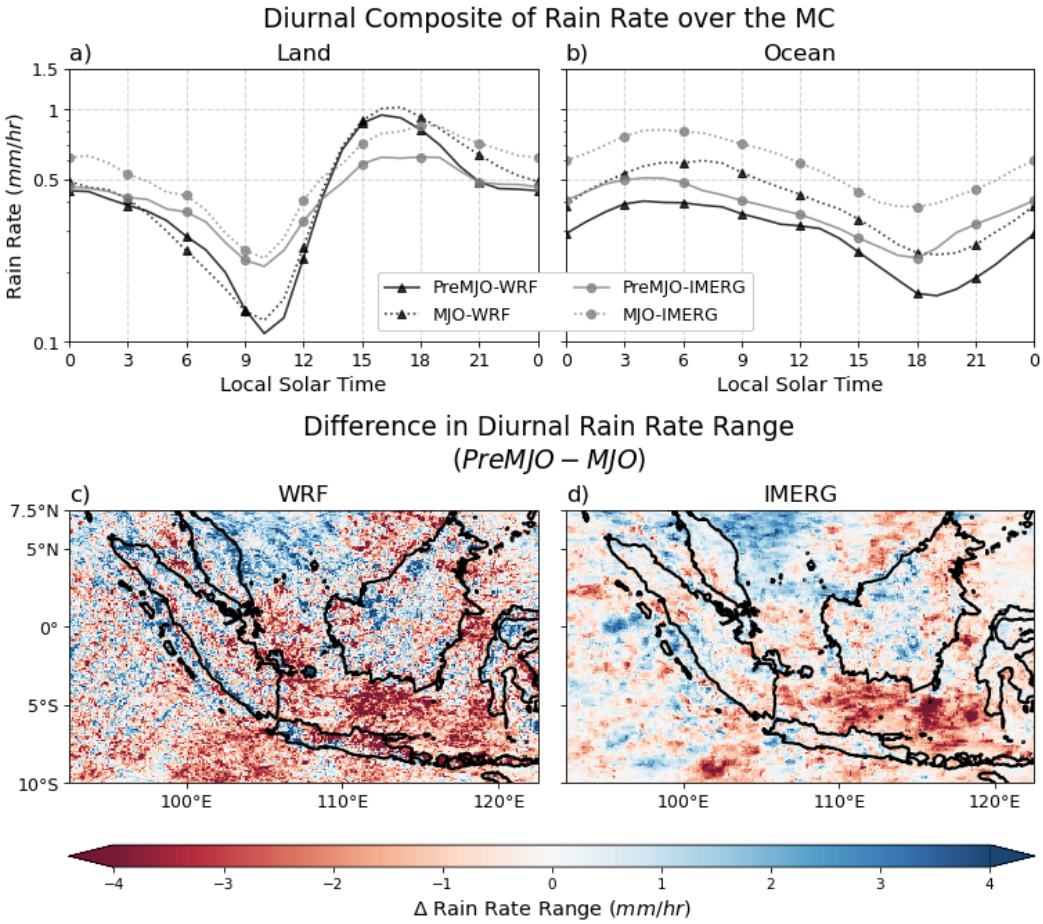

Figure 3.1: The domain average diurnal composite of rain rate (mm/hr, log-scale) is calculated over the MC domain for WRF CTRL simulations after spatial regridding to match IMERG (triangles), and for IMERG after temporal aggregation to match WRF's hourly output (circles). Rain rates are averaged over the land (a) and ocean (b) domains during the PreMJO (solid) and MJO (dashed) periods. c,d) The diurnal composite of rain rate range difference between PreMJO and MJO are shown spatially after WRF spatial regridding and IMERG temporal aggregation, where red shading indicates greater diurnal rain rate range during the PreMJO period and blue shading indicates greater diurnal rain rate range during the MJO period.

3.2.4 Moisture and Circulation Sensitivity Experiments

To test the intraseasonal change in large-scale environmental moisture and circulation on the diurnal cycle of rainfall, we leverage initialization and boundary condition experiments to adjust the environmental conditions. This is done by taking PreMJO large-scale fields—relative humidity (RH) and/or zonal and meridional winds (U,V) from ERA5—and imposing them during the MJO period. Three experiments are conducted during the MJO period in which RH ($Swap_{RH}$), winds ($Swap_{U,V}$), or both ($Swap_{RH,U,V}$) variables from the ERA5 files used to initialize and update boundary conditions are replaced with values used during the PreMJO period (Table 3.1). To verify that the swap simulations reproduce the intended large-scale conditions, 850-hPa winds and vertically integrated (VI) RH calculated between 1000–100 hPa are time-averaged over each 10-day long period (Fig. 3.2).

$$\text{VI RH} = \frac{\frac{1}{g}\int_{1000\,\text{hPa}}^{100\,\text{hPa}} q_v \,\mathrm{d}p}{\frac{1}{g}\int_{1000\,\text{hPa}}^{100\,\text{hPa}} q_{vs} \,\mathrm{d}p} \times 100 \tag{3.1}$$

q_v and q_{vs} are the water vapor mixing ratio and saturation mixing ratio, respectively, p is pressure, g is the acceleration due to gravity and the integration is performed from 1000 to 100 hPa. The results demonstrate that the swapped variables in the swap experiments (i.e., VI RH in $Swap_{RH}$) closely follow the PreMJO large-scale pattern, indicating that the swap experiments successfully impose the desired large-scale conditions. With the experiments working as intended, we will now examine the diurnal cycle of rainfall across all simulations and identify the mechanisms through which moisture and circulation influence diurnal rainfall.

Table 3.1: Overview of the experimental design. Three swap experiments are performed during the MJO period by replacing ERA5 large-scale relative humidity (RH) and/or horizontal winds (U,V) in the initialization and lateral boundary conditions with values from the PreMJO period.

Experiment	**Time Period**	**Imposed fields from** $PreMJO$
$PreMJO$	Nov 23-Dec 03, 2015	-
MJO	Dec 10-20, 2015	-
$Swap_{RH}$	Dec 10-20, 2015	RH
$Swap_{U,V}$	Dec 10-20, 2015	U,V
$Swap_{RH,U,V}$	Dec 10-20, 2015	RH,U,V

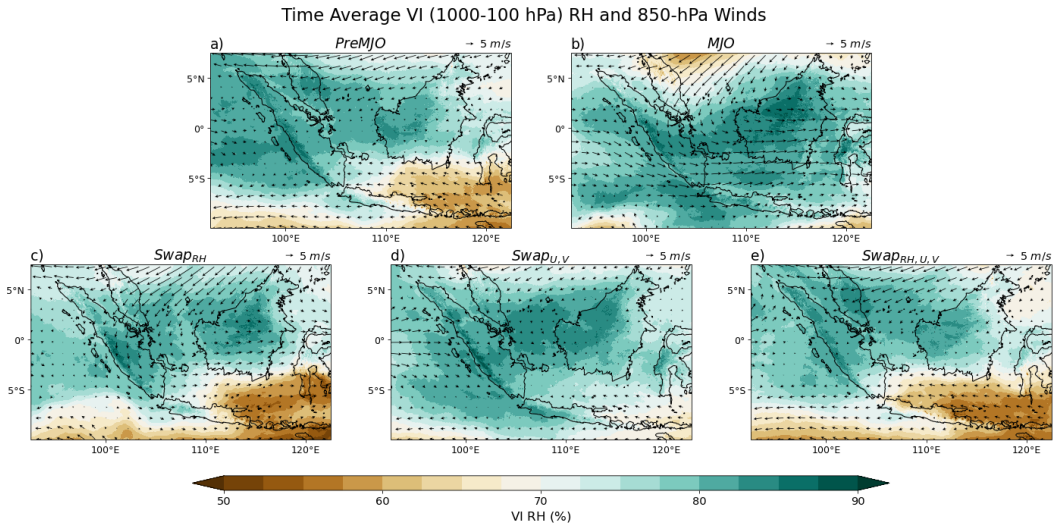

Figure 3.2: Time-averaged vertically integrated (1000-100 hPa) relative humidity (VI RH, %) and 850-hPa wind vectors (m/s) are calculated for each simulation.

3.3 Results

3.3.1 Moisture and Circulation Influence Diurnal Rainfall Differently Over Land and Ocean

Since moisture is key driver of rainfall over the tropics, the modulation of moisture by the MJO will have an influence on rain rates. To capture the change in the strength of diurnal rainfall with the changing large-scale moisture environment, the difference

in the average grid-point diurnal rain rate range and the grid-point time-averaged VI RH is taken between each simulation and the MJO and averaged over all land and ocean grid points. Between the CTRL simulations ($PreMJO - MJO$), time- and domain-averaged VI RH is roughly 3% lower over land and ocean points (Fig. 3.3b), while diurnal rain rate range is much weaker over the ocean compared to over land (Fig. 3.3a). Swapping RH to PreMJO-like conditions during the MJO period ($Swap_{RH}$) dries the atmosphere over land to levels comparable to $PreMJO$, while producing an even drier atmosphere over the ocean. Despite a comparable amount of environmental drying in $PreMJO$ and $Swap_{RH}$, the land diurnal rainfall decreases more in $Swap_{RH}$ (Fig. 3.3). This mismatch implies that either $Swap_{RH}$ diurnal rainfall over land is more sensitive to drying than $PreMJO$, or that the spatial distribution of VI RH varies. Qualitatively, we can see that the spatial distribution and magnitude of VI RH vary over land and ocean between $Swap_{RH}$ and $PreMJO$ (Fig. 3.2a,c), implying the importance of MJO circulation in modulating diurnal rainfall over land.

Swapping winds to PreMJO conditions ($Swap_{U,V}$) does not dry the atmosphere as much as $Swap_{RH}$, but despite the slight drying, the the rain rate range in $Swap_{U,V}$ increases from MJO over land (Fig. 3.3). These results suggest that the strength of the diurnal cycle of rainfall over the western MC islands is strongly suppressed under PreMJO moisture conditions (drier) and enhanced under PreMJO wind conditions (anomalous easterlies). Swapping both RH and winds result in the driest atmosphere over the western MC, the weakest diurnal rain rate range over ocean, and the closest to $PreMJO$ diurnal rain rate range over land (Fig. 3.3). On average, diurnal rain rate range difference over ocean follows the difference in VI RH but not over land (Fig. 3.3). This motivates an investigation of the relationship between environmental moisture and diurnal rainfall to better understand the role of atmospheric moisture in modulating the diurnal rainfall over land and ocean.

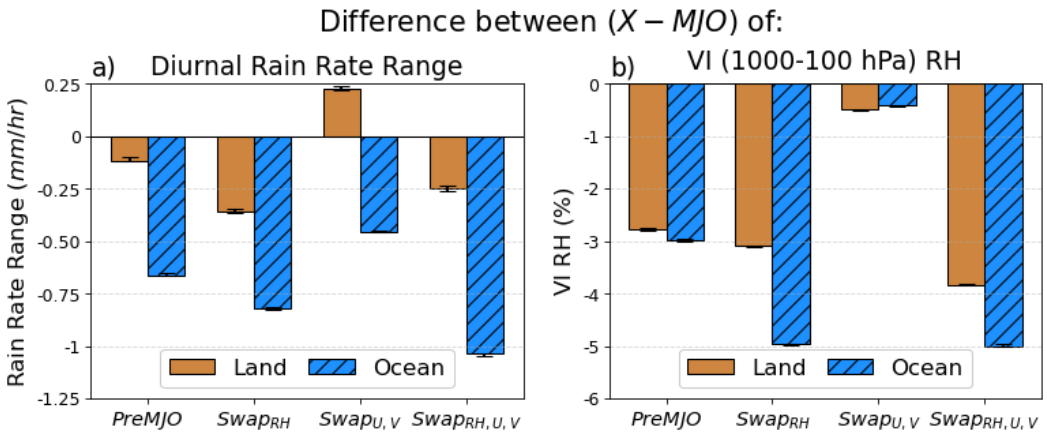

Figure 3.3: The grid-point difference of (a) diurnal rain rate range (mm/hr) and (b) time-averaged vertically integrated (1000-100 hPa) relative humidity (VI RH, %) from MJO domain-averaged over land (brown, no hatch) and ocean (blue, hatched) points, where X represents the corresponding simulation labeled on the x-ticks. The black brackets represent the confidence interval at a 95% confidence level through bootstrapping at $N = 1000$.

3.3.2 Predominant Role of Moisture on Oceanic Diurnal Rainfall

Previous studies have shown that tropical oceanic precipitation increases exponentially with column moisture (the P-r relationship), as greater atmospheric humidity reduces the negative effects of entrainment on convective updrafts, allowing convection to strengthen and produce higher rain rates (Bretherton et al., 2004; Peters and Neelin, 2006; Holloway and Neelin, 2009). To test the influence of environmental moisture on rain rate, the daily rain rate and VI RH (1000-100 hPa) is calculated for all days (N=10 days) and binned at 1% VI RH intervals over land and ocean points (Fig. 3.4a,b). Over land and ocean, the simulations generally align along a common exponential curve (y-axis is log scale, Fig. 3.4a,b) despite differences in the distribution of VI RH (Fig. 3.4c,d), showing that daily rainfall increases exponentially with VI RH among all the simulations.

The P–r relationship is stronger (exhibits a steeper slope) and has a greater variability in the average rain rates across all simulations (scatter points) over ocean than over land, suggesting that oceanic rainfall is more sensitive to environmental moisture (Fig. 3.4). Despite the stronger oceanic P-r relationship, land regions exhibit higher daily rainfall rates under drier conditions (VI RH $< 60\%$), implying that the exponential increase in rainfall begins at lower column moisture values over land than over ocean, consistent with prior studies (Ahmed and Schumacher, 2017; Bergemann and Jakob, 2016). These results suggest that the drier environment associated with the $PreMJO$ exerts a stronger control on the oceanic diurnal rainfall, however, domain-averaged VI RH does not necessarily explain rainfall responses in all experiments (Fig. 3.3).

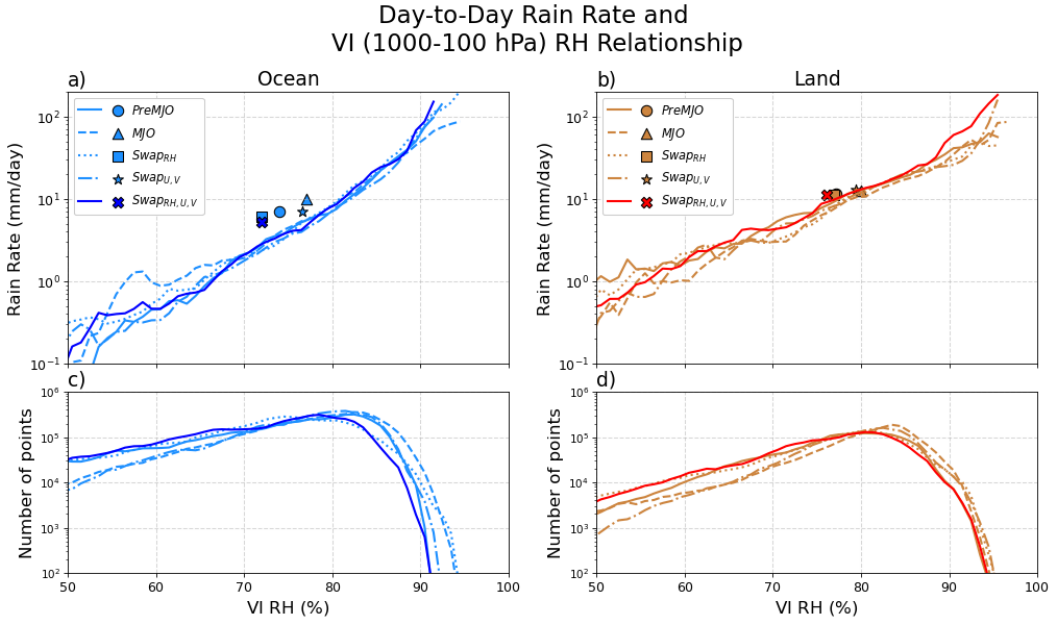

Figure 3.4: The daily rain rate (mm/day) and vertically integrated (1000-100 hPa) relative humidity (VI RH) is calculated for all days (N=10 days) and binned at 1% VI RH intervals over (a) land and (b) ocean points for all simulations, with the corresponding number of points (log-scale) at each VI RH bin (c,d). The scatter points represent the time-averaged rain rate and relative humidity across the entire time period.

Despite the nearly equivalent difference in VI RH between $Swap_{RH}$ and $Swap_{RH,U,V}$,

the latter exhibits a much larger decrease (27%) in oceanic diurnal rain rate range, suggesting that other factors are responsible for the change in rain rate range (Fig. 3.3). We compare the time-averaged spatial distribution of diurnal rainfall (Fig. 3.5) and the moisture and lower-tropospheric wind fields (Fig. 3.2) to understand whether the spatial distribution of moisture explains the disproportionate diurnal rain rate range response to VI RH between $Swap_{RH}$ and $Swap_{RH,U,V}$. The time-averaged rainfall during the MJO is widespread over the oceans and especially strong along the western half of Java and the Java sea between Java and Borneo, the region traversed by this specific MJO convective envelope (Fig. 3.2b). These specific regions across all simulations exhibit the largest differences in VI RH compared to MJO, which would result in the largest difference in rainfall following the exponential P-r relationship (Fig.3.2). This suggests that local changes in moisture is a key factor in determining the domain-average and spatial distribution of diurnal rainfall over the ocean.

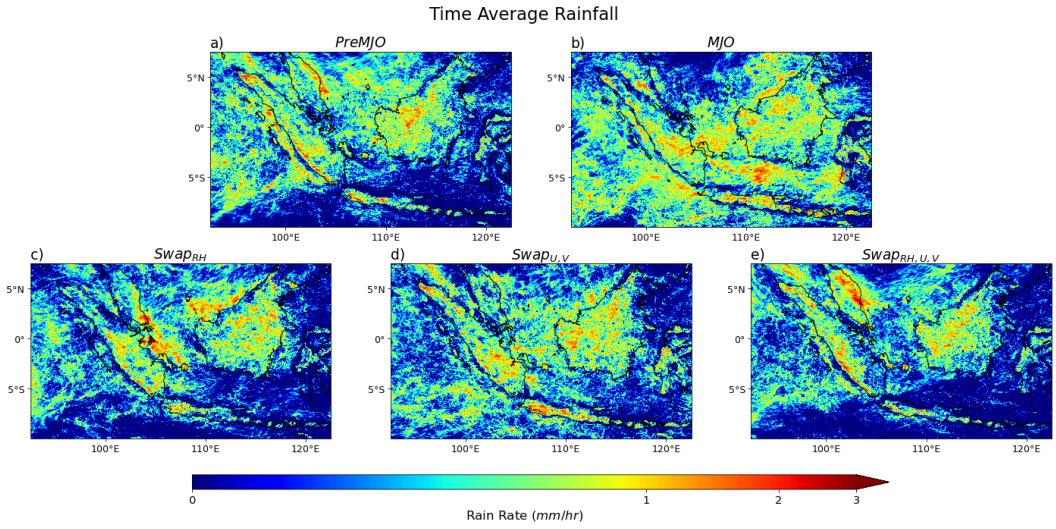

Figure 3.5: Time-averaged rain rate (mm/hr) for each simulation.

$Swap_{RH,U,V}$ average daily rain rate is spatially consistent with $PreMJO$, but the magnitude of oceanic rainfall in $Swap_{RH,U,V}$ is much weaker than $PreMJO$ over the Indian Ocean and South China Sea (Fig. 3.5a,e). The weaker rainfall over the Indian

Ocean can be explained by the exponential relationship between rainfall and VI RH, whereby a given change in VI RH produces larger rainfall differences at higher VI RH values (Fig. 3.4a). The VI RH values over the Indian Ocean region in $PreMJO$ is relatively high, while $Swap_{RH,U,V}$ is drier (Fig. 3.2a,e), resulting in a sharper decline in average rainfall rates over the Indian Ocean region. The weaker rainfall over the South China Sea cannot be explained by the magnitude differences since they have relatively similar VI RH values (Fig. 3.2a,e). Therefore, processes beyond moisture, such as changes in the offshore diurnal propagation of convection originating from Borneo, may play an important role in modulating oceanic diurnal rainfall over the South China Sea and explain why domain-averaged diurnal rainfall range differs between $Swap_{RH,U,V}$ and $PreMJO$ over some oceanic regions. Across all simulations, time-averaged rainfall also varies over land, leading us to investigate how environmental conditions influence diurnal rainfall over land in the next section (Fig. 3.5).

3.3.3 Understanding the Mechanisms Driving the Land Diurnal Cycle

While moisture is an important factor for land diurnal rainfall, the P-r relationship alone does not directly explain the changes in the domain-averaged diurnal rain rate range over land between the simulations (Fig. 3.3). The land diurnal cycle of convection over tropical islands is strongly driven by daytime surface shortwave heating, which destabilizes the boundary layer and initiate convection through orographic slope flow and sea-breeze-induced onshore flow associated with the land–sea thermal gradient. Prior research suggests that stronger background winds can weaken the land-sea thermal contrast through enhanced turbulent mixing and ventilation, resulting in weaker onshore flow and reduced instability (Wang and Sobel, 2017; Natoli and Maloney,

2023b; Short et al., 2019; Shige et al., 2017). Prior studies have also demonstrated that a terrain-relative (west/east, south/north) dipole in rainfall exists over major islands of the MC and weakens and/or flips to the opposite side of the terrain face during the onset of the MJO enhanced phase (Ichikawa, 2006; Sakaeda et al., 2020; Qian, 2020; Zhou et al., 2022; Bai and Schumacher, 2022). Turbulent mixing and ventilation is enhanced over the windward side of the islands which suppresses the diurnal coastal thermal gradient, possibly explaining the observed terrain-relative dipole in diurnal rainfall associated with the modulation in environmental winds with the propagation of the MJO. Therefore, we hypothesize that stronger background winds associated with the MJO weaken land diurnal rainfall more over the windward side of the islands through the weakening of the coastal land-sea thermal gradient and instability over land. We first develop an objective method to partition and analyze island terrain-faces to investigate the terrain-relative dipole in diurnal rainfall.

3.3.3.1 Island Partitioning and Coastal Analysis Framework

To ensure we investigate regions that experience a strong intraseasonal shift in background wind speed and direction, we first isolate the large islands along the propagation path of this particular MJO's convective envelope—Sumatra, Borneo, Java, and Sulawesi—thereby neglecting all smaller islands and the Malay Peninsula. Due to the varying influence of large-scale winds on the leeward and windward side of islands (Wang and Sobel, 2017; Natoli and Maloney, 2023b), we introduce a novel semi-objective method to divide each island into their western and eastern components (or southern and northern for Java). We divide islands at their respective maximum terrain heights (ridge line) at each latitude (longitude for Java) of the island after applying a variable gaussian spatial smoother onto terrain heights to avoid sharp transitions between mountain peaks (Fig. B.3a). The amount of spatial smoother applied in the

latitude and longitude varied between islands in order to ensure the terrain-face divide avoided distant terrain peaks, resulting in a semi-objective approach. After the islands are split into two components, the distance from the coast is calculated with respect to each island terrain face coastline, where the coastline is centered at $0m$, negative values moving onshore and positive moving offshore from the coastline (Fig. B.3b,c). Due to the importance of coastal flow over tropical islands, certain variables (i.e., winds) are projected onto the coast-normal unit vector to calculate their coast-normal components and subsequently averaged within a $\pm 25km$ coastal band to characterize the coastal environment, according to

$$X_{\perp}(d,t) = \mathbf{X}(d,t) \cdot \hat{\mathbf{n}} \tag{3.2}$$

$\mathbf{X}$ represents the vector variable of interest at distance from the coastline d and time t, $\hat{\mathbf{n}}$ is the coast-normal unit vector (positive offshore), and $X_{\perp}$ is the corresponding coast-normal component. We then take the coastal average over each terrain face coastline

$$\overline{X_{\perp}(t)} = \frac{1}{N} \sum_{n=1} X_{\perp}(d_n, t) \tag{3.3}$$

where N is the number of points and d_n is the coastal bounds used (-25 km $\leq d_n \leq$ $+25$ km). Consistent with previous studies and our own findings (not shown), Java features a more south/north contrast than the east/west contrast over other islands Qian (2020). We simplify the terminology hereafter by including Java's southern and northern terrain faces within the western and eastern terrain face categories, respectively.

3.3.3.2 MJO-associated Moisture and Circulation Modulates Terrain-Face Differences in Land Diurnal Rainfall

We first examine the relationship between land-averaged diurnal rain rate range and 950-hPa time-averaged coastal onshore flow ($\overline{u_{\perp,950hPa}}$) over the western and eastern sides to see whether stronger mean winds correspond to weaker diurnal rainfall over land (Fig. 3.6a,b). The 950-hPa level was chosen due to its position within the boundary layer, allowing the detection of coastal flow without the signal being dominated by free tropospheric winds and surface friction. From PreMJO to MJO, rainfall increases with weaker onshore flow on the eastern side, and rainfall decreases with stronger onshore flow on the western side (Fig. 3.6a,b). The terrain-relative dipole in rainfall also weakens from PreMJO to MJO, which could be associated with the changes in the mean onshore flow, in agreement with prior studies (Fig. 3.6a) (Qian et al., 2013; Wang and Sobel, 2017; Zhou et al., 2022; Natoli and Maloney, 2023b; Qian, 2020). These results suggest that stronger MJO background winds suppress land diurnal rainfall, supporting the first part of our hypothesis, however, the underlying mechanism responsible remains unclear.

The diurnal range of 2-m potential temperature gradient projected onto the coast normal unit vectors (Eq. 3.2) is averaged over the coastal region ($\nabla_\perp \theta_{2\,\mathrm{m}}$, Eq. 3.3) to quantify the strength of the coastal land-sea thermal gradient along each terrain side coast (Fig. 3.6c). The diurnal land-sea thermal gradient range decreases equally over both sides from PreMJO to MJO, likely due to the domain increase in cloud-cover as the MJO convective envelope propagates over the western MC (not shown). The on- and off-shore flow arises from a sea-to-land oriented pressure gradient force caused by the differential heating between land and sea, and we can see this represented on both terrain side coasts by showing the diurnal sea-level pressure (SLP) range (Fig. 3.6d),

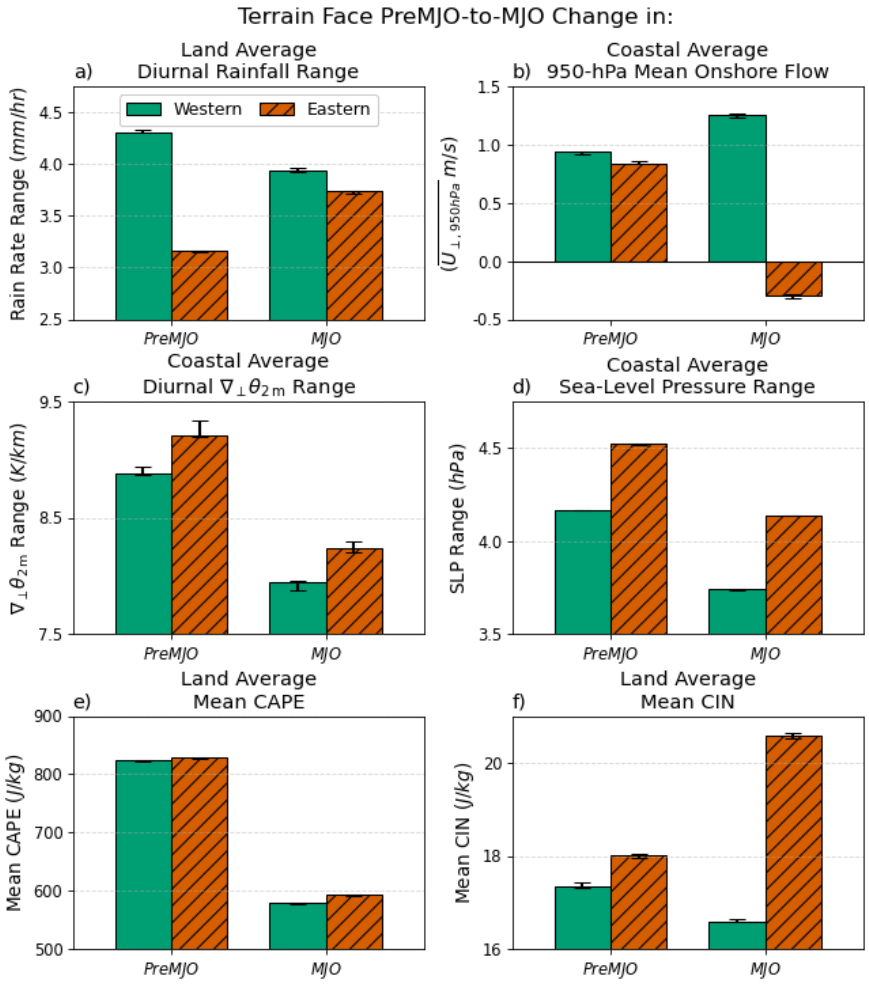

Figure 3.6: The PreMJO-to-MJO terrain face changes in (a) land-average diurnal rain rate range, (b) coastal- and time-averaged 950-hPa onshore flow, (c) coastal-averaged diurnal coast-normal 2-m potential temperature gradient ($\nabla_n \theta_{2\,\mathrm{m}}$) range, (d) coastal-averaged diurnal sea-level pressure (SLP) range, (e) land- and time-averaged convective available potential energy (CAPE), (f) land- and time-averaged convective inhibition (CIN) are averaged over the four main islands (Sumatra, Borneo, Java, and Sulawesi) over the western (teal, no hatch) and eastern (orange, hatch) terrain faces for the $PreMJO$ and MJO. The black brackets represent the confidence interval at a 95% confidence level through bootstrapping at $N = 1000$.

following a similar method used in a prior study (Natoli and Maloney, 2023b).

On both terrain sides, the land–sea thermal gradient and diurnal SLP range both weaken from PreMJO to MJO, suggesting that a weaker thermal gradient induces a weaker onshore and offshore flow. Over the western side, this change is associated

with weaker land diurnal rainfall, suggesting that stronger background flow ultimately weakens the coastal thermal gradient driving on- and off-shore flow. However, the eastern side exhibits an increase in diurnal rainfall strength, suggesting that diurnal rainfall strength is not strongly modulated by a weaker land-sea thermal gradient over the eastern side. Therefore, the mechanism driving the PreMJO-to-MJO increase in diurnal rainfall strength over the eastern side remains to be understood.

Favorable convective environments over land can enhance diurnal convection, potentially explaining why diurnal rainfall increases with decreasing coastal thermal gradient over the eastern sides. To assess whether MJO-associated changes in atmospheric stability contribute to this behavior, we examine the PreMJO-to-MJO land- and time-averaged convective available potential energy (CAPE) and convective inhibition (CIN) provided by the WRF-Python library (Fig. 3.6e,f) (UCAR/NCAR, 2025). CAPE represents the accumulated buoyant energy from the level of free convection to the equilibrium level, where larger values generally indicate a greater potential for deep convection, whereas CIN is the accumulated negative buoyant energy from the parcel starting point to the level of free convection, where larger values generally indicate a greater suppression of convective initiation. Although both CAPE and CIN have limitations as measures of atmospheric instability/stability, together they provide a useful first-order assessment of the convective environment over the islands.

CAPE decreases and CIN increases from PreMJO to MJO over the eastern sides, suggesting that diurnal rainfall should be suppressed; instead, diurnal rainfall strengthens (Fig.3.6a,e,f). This discrepancy suggests that either the convective environment over the eastern side is not responsible for the strengthening of diurnal rainfall from PreMJO to MJO, or that the limitations of CAPE and CIN obscure the processes responsible for this strengthening. For example, CAPE specifically does not account for the effects of air entrainment as an air parcel ascends through the troposphere,

therefore, an environment with relatively weak CAPE could produce as much or more rainfall if the atmospheric profile is moister. This is critical because the atmospheric column progressively moistens from the lower-to-upper troposphere as the MJO propagates across the MC, implying that a relatively drier mid- and upper-levels during $PreMJO$ may suppress convection through enhanced dry-air entrainment that high values of CAPE do not capture. Therefore, we hypothesize that the environmental moisture profile is an important control on diurnal rainfall strength over the islands, particularly over the eastern side of islands.

To investigate the PreMJO-to-MJO evolution of moisture over each terrain face, the land- and time-averaged VI RH between 1000-100 hPa is shown over the western and eastern sides (Fig. 3.7a). As expected, the VI RH increases over both terrain sides from PreMJO to MJO, while it is only the eastern side that increases in diurnal rainfall strength over this time period (Fig. 3.6a). When the atmospheric column is divided into low- (1000-700 hPa), mid- (700-500 hPa), and upper-levels (500-100 hPa), the PreMJO-to-MJO increase in VI RH is significantly more as the vertical levels increase (Fig. 3.7b-d). This result suggests that, while an increase in column moisture enhances diurnal rainfall over land (Fig. 3.4b), wind-driven mechanisms weaken diurnal land- and sea-breeze flows, suppressing diurnal rainfall over the western side. We next test the sensitivity of these mechanisms to MJO-associated moisture and winds to better understand their individual impact on diurnal rainfall.

3.3.3.3 Sensitivity of MJO-associated Environmental Moisture and Wind on Diurnal Rainfall over Land

Our results imply that diurnal rainfall strength over the western sides are modulated more by the strength of the land-sea thermal gradient, while the eastern sides are modulated more by environmental moisture. Therefore we hypothesize that diurnal rainfall

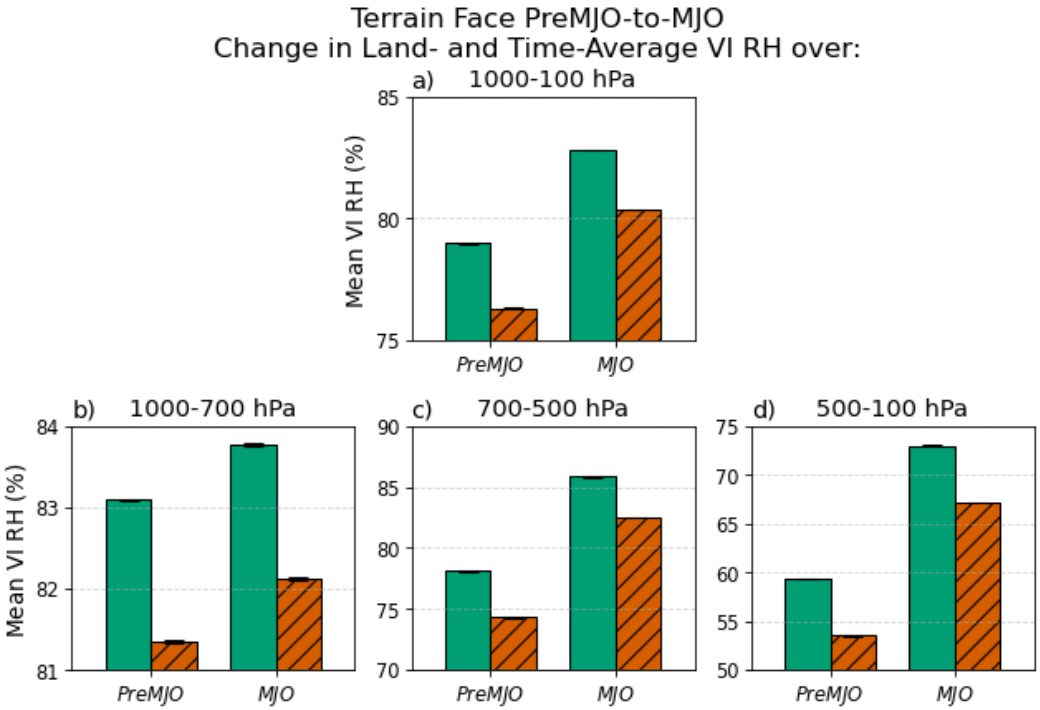

Figure 3.7: Same as Fig. 3.6 but with the y-axis representing land- and time-averaged vertically integrated relative humidity (VI RH) between (a) 1000-100 hPa, (b) 1000-700 hPa, (c) 700-500 hPa, (d) 500-100 hPa.

strength over the western sides from $Swap_{U,V}$ will agree more with $PreMJO$, whereas rainfall values from the eastern sides from $Swap_{RH}$ will agree more with $PreMJO$, with $Swap_{RH,U,V}$ exhibiting the closest overall agreement with $PreMJO$.

Following Fig.3.6a, the land diurnal rain rate range averaged over the eastern and western terrain faces are shown across all simulations, identifying which swapped environmental variable modulates diurnal rainfall towards $PreMJO$ values over each terrain face (Fig. 3.8). Swapping the winds to PreMJO conditions ($Swap_{U,V}$) significantly increases diurnal rainfall range over the western sides while leaving the eastern sides unchanged compared to MJO This suggests the importance of weak mean flow associated with the PreMJO period on diurnal rainfall strength over the western sides. The eastern sides only decrease in diurnal rainfall range compared to MJO when

moisture is adjusted to PreMJO conditions ($Swap_{RH}$ and $Swap_{RH,U,V}$), suggesting that moisture and the advection of moisture both play important roles in determining diurnal rainfall strength. Additionally, $Swap_{U,V}$ enhances the terrain-relative dipole of rainfall, whereas $Swap_{RH}$ weakens or reverses it, and $Swap_{RH,U,V}$ most closely reproduces the strength of the $PreMJO$ dipole, highlighting the combined importance of the background flow and moisture in driving the intraseasonal shift in the terrain-relative dipole of rainfall. These results confirm that modulating the MJO-associated environmental variables affect diurnal rainfall, but the mechanisms responsible have not been examined across all simulations.

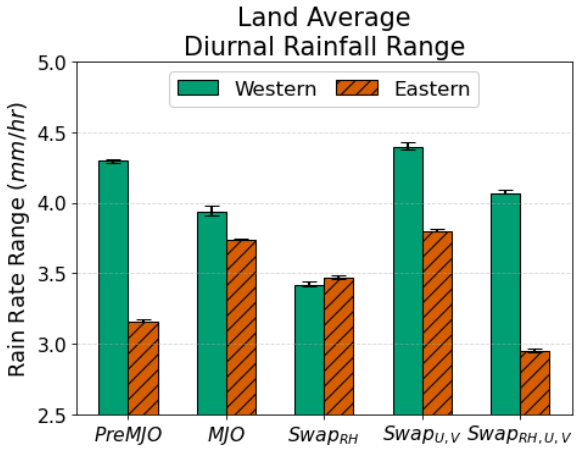

Figure 3.8: Same as Fig. 3.6a, but for all simulations.

We begin by investigating the relationship between the mean flow and the diurnal coastal thermal gradient range across all simulations (Fig. 3.9a). The results exhibit relatively little variation in mean onshore flow over the western sides compared to the eastern, despite having near-equal variation in the diurnal coastal thermal gradient range (Fig. 3.9a). However, swapping to PreMJO wind conditions ($Swap_{U,V}$) strengthens the diurnal coastal thermal gradient range as mean onshore flow weakens over the western sides (Fig. 3.9a). This result paired with the increase in diurnal rainfall strength over the western sides in $Swap_{U,V}$ (Fig. 3.8) suggests that weak anomalous

easterlies associated with the PreMJO time period enhance diurnal rainfall strength on the western sides (Fig. 3.9a). Despite the strengthening coastal thermal gradient, diurnal rainfall strength decreases on the eastern sides (Fig. 3.8, Fig. 3.9a), suggesting that a different mechanism contributes to the changes in diurnal rainfall over the eastern sides.

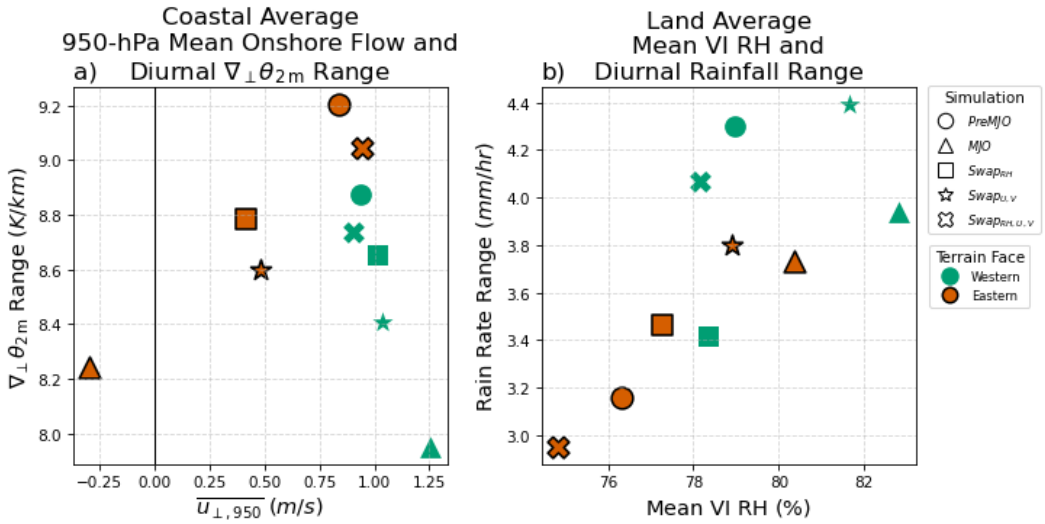

Figure 3.9: (a) Coastal- and time-averaged 950-hPa onshore flow and the diurnal coastal thermal gradient range and the (b) land- and time-averaged vertically integrated relative humidity (VI RH) calculated between 1000-100 hPa and land-averaged diurnal rainfall range is shown for each simulation (marker shape) and terrain face (color and edge line).

The results presented thus far suggest that environmental moisture plays a larger role in modulating diurnal rainfall over the eastern sides than the western. The relationship between the land- and time-averaged VI RH calculated between 1000-100 hPa and diurnal rainfall range across all simulations and terrain faces confirm our prior results (Fig. 3.9b). A strong and clear positive relationship over the eastern side appear in contrast to the unclear western side, confirming that environmental moisture modulates diurnal rainfall over the eastern terrain faces. Additionally, imposing PreMJO-like drier environmental conditions ($Swap_{RH}$) more closely reproduces the

diurnal rainfall strength of the $PreMJO$ over the eastern sides. These results suggest that environmental moisture plays an important role in modulating diurnal rainfall over the eastern sides, where MJO-associated moisture strengthens diurnal rainfall, partially contributing to the weakening of the terrain-relative dipole in diurnal rainfall from PreMJO to MJO.

While the individually swapped simulations ($Swap_{RH}$ and $Swap_{U,V}$) showed a considerable shift in the mechanisms driving diurnal rainfall towards $PreMJO$, swapping both ($Swap_{RH,U,V}$) represent the mechanisms driving diurnal rainfall over the western MC the best due to the dual importance of moisture and circulation on diurnal rainfall over the islands (Fig.3.9). This suggests the important role of moisture and winds play in accurately representing the intraseasonal shift in diurnal rainfall over the western MC, highlighting moisture advection in determining the magnitude and spatial distribution of diurnal rainfall across the western MC islands.

3.3.4 Conclusions

The diurnal cycle of rainfall's land-sea contrast and its spatial distribution over the MC islands has been observed to modulate with the propagation of the MJO (Ichikawa, 2006; Qian, 2020; Zhou et al., 2022; Bai and Schumacher, 2022; Ling et al., 2019). Despite the importance of the MJO and diurnal rainfall over this region, the underlying mechanisms responsible for the observed intraseasonal changes in diurnal rainfall remain uncertain. Understanding the mechanisms through which diurnal rainfall modulates with the MJO can inform efforts to improve the representation of both the diurnal rainfall cycle and the MJO in GCMs (Chen et al., 2022; Yin and Porporato, 2017; Tang et al., 2021; Dong et al., 2023). Our investigation utilizes a convection-permitting model to understand how the onset of the MJO enhanced phase modulates diurnal rainfall over the western MC, which specific mechanisms are responsible, and

how MJO-associated moisture and winds enhance or suppress those mechanisms.

We select an MJO event that occurred in late 2015 (November 23 to December 20, 2015), which provided a well-documented strong change in diurnal convection over the MC (Yokoi et al., 2017). We conduct a pair of control (CTRL) experiments using the WRF model to provide a baseline of diurnal rainfall evolution over the MC when the MJO enhanced phase was over the Indian Ocean ($PreMJO$, November 23 to December 03, 2015) and when it was over the MC region (MJO, December 10 to December 20, 2015). To test the sensitivity of diurnal rainfall to MJO-associated moisture and/or winds, we impose the large-scale fields during the PreMJO period—relative humidity (RH) and/or zonal and meridional winds (U,V) from ERA5— onto the MJO period (Table 3.1). These sensitivity experiments, named after the variables that were imposed during the MJO period ($Swap_{RH}$, $Swap_{U,V}$, and $Swap_{RH,U,V}$), follow $PreMJO$ large-scale moisture and/or wind patterns. Utilizing these experiments, we demonstrate that the diurnal cycle of rainfall modulates differently over land and ocean with changing environmental moisture and circulation (Fig. 3.3).

Domain-averaged diurnal rainfall range over the ocean closely follow column-integrated moisture, whereas the land diurnal rainfall does not (Fig. 3.3). Oceanic rainfall is more strongly modulated by column-integrated moisture than over land (P-r relationship) over the western MC, suggesting that the drier environment associated with the Pre-MJO period strongly suppresses oceanic diurnal rainfall (Fig. 3.4a). The spatial distribution of moisture varies when MJO-associated moisture and winds are decoupled ($Swap_{RH}$, $Swap_{U,V}$), resulting in spatially varying diurnal rainfall, emphasizing the important role moisture advection plays in determining the location of rainfall on the intraseasonal timescale (Fig. 3.2, Fig. 3.5). The weaker P-r relationship (slope) over land compared to ocean (Fig 3.4a,b) suggests that other processes outside of moisture could be contributing to the strength of diurnal rainfall over land.

Diurnal rainfall over tropical islands is strongly driven by the destabilization of the boundary layer by insolation and initiate convection through orographic slope flow and sea-breeze-induced onshore flow during the day. Enhanced turbulent mixing and ventilation from large-scale winds have been shown to strongly dilute these drivers of diurnal rainfall over the windward side of islands (Wang and Sobel, 2017; Short et al., 2019; Shige et al., 2017; Natoli and Maloney, 2023b). We divide the islands into western and eastern facing components to investigate the relationship between large-scale MJO-associated onshore flow and land diurnal rainfall and found that diurnal rainfall over the western sides suppresses when large-scale onshore flow increases (Fig. 3.6a,b). We associate this change to the weakening of the coastal land-sea thermal gradient by enhanced large-scale turbulent mixing and ventilation (Fig. 3.6c). However, diurnal rainfall increases with decreasing coastal thermal gradient over the eastern sides (Fig. 3.6a,c). This suggests that diurnal rainfall strength is not strongly modulated by a weaker land-sea thermal gradient over the eastern side of islands.

The MJO strongly modulates environmental moisture, progressively moistening the lower-to-upper levels of the troposphere, reducing the dry-air entrainment that convection experiences to allow for deeper and persistent convection. The moisture profile over the western sides are generally moister than the eastern (Fig. 3.7), therefore, changes in the strength of the mechanical forcing from the sea breezes may modulate diurnal rainfall more, while changes in moisture may modulate rainfall more over the drier eastern sides (Fig. 3.7). The separate mechanisms modulating diurnal rainfall over each terrain face may help explain why a terrain-relative dipole in rainfall over the MC exists and modulates with the passing of an MJO event (Ichikawa, 2006; Sakaeda et al., 2020; Qian, 2020; Zhou et al., 2022; Bai and Schumacher, 2022).

The relationships that drive diurnal rainfall over each terrain face are investigated further through the swap experiments to confirm the effect of environmental moisture

and wind on diurnal rainfall. We demonstrate that weak large-scale winds associated with the PreMJO period ($Swap_{U,V}$) enhance western side diurnal rainfall, while the drier conditions from the PreMJO period ($Swap_{RH}$) suppress eastern side diurnal rainfall (Fig. 3.9). This validates our findings by suggesting the importance of circulation on the western sides and moisture on the eastern sides in determining diurnal rainfall strength. This is further supported by $Swap_{RH,U,V}$, which best reproduces the diurnal rainfall and underlying mechanisms of $PreMJO$ on both sides of the islands. These results suggest that environmental moisture and winds are both critical in driving the mechanisms that contribute to the intraseasonal modulation of diurnal rainfall over the islands of the western MC.

Our findings agree with prior studies that have suggested the importance of moisture advection by the MJO to enhance diurnal rainfall over ocean (Zhang and Ling, 2017) and the role MJO-associated circulation play in modulating the strength and spatial distribution of diurnal rainfall over islands (Qian et al., 2013; Wang and Sobel, 2017; Zhou et al., 2022; Natoli and Maloney, 2023b; Qian, 2020). Our findings provide new insight by suggesting that the driver of rainfall over the islands differ between terrain sides, emphasizing the role of moisture and winds in determining the intraseasonally modulating terrain-relative rainfall dipole.

While our results are robust in targeting the mechanisms driving the intraseasonal change in diurnal rainfall over the western MC, MJO events vary greatly depending on a multitude of factors, therefore, it is critical to expand this investigation into multiple MJO-events to better understand how these mechanisms generally modulate with the MJO. Further analysis is required to understand whether the PreMJO-to-MJO increase in diurnal rainfall strength over the eastern sides is due to the advection of convection from the western-to-eastern sides, and whether large-scale moisture and/or winds play a more dominate role in the advection. This study's findings provide a framework for

evaluating whether GCMs accurately reproduce the mechanisms that modulate diurnal rainfall over the western MC, thereby improving projections at both regional and global scales.

Chapter 4

Summary and Conclusions

The primary objective of this dissertation was to isolate and clarify the specific physical mechanisms regulating the diurnal cycle of rainfall over the western MC and to determine how these localized processes are modulated by large-scale environmental variations induced by the MJO. Understanding these multi-scale interactions is crucial for addressing systematic GCM biases, which persistently fail to capture the timing, amplitude, and spatial distribution of both diurnal convection and intraseasonal convective propagation over the MC (Yin and Porporato, 2017; Zhang and Ling, 2017; Christopoulos and Schneider, 2021; Dong et al., 2023; Bai and Schumacher, 2022; Chen et al., 2022). By leveraging high-resolution, convection-permitting simulations via the WRF model, this work systematically isolated key physical controls under realistic environmental conditions that observational and idealized modeling frameworks cannot decouple—specifically cloud-radiative interactions (Chapter 2) and MJO-induced moisture and circulation (Chapter 3). Together, the results demonstrate that local topographically-driven thermal gradients and basin-scale dynamics and thermodynamics are deeply coupled, providing an empirical road map for parameterization development in daily and subseasonal-to-seasonal forecasting systems.

Chapter 2 directly addressed how cloud-radiative interactions influence diurnal rainfall characteristics and how island topography strongly alters this relationship. The removal of cloud-radiative interactions in WRF (NCRF) revealed that clouds act as a strong thermodynamic dampener on the diurnal cycle of rainfall. Disabling cloud-radiative interactions increased the land diurnal rainfall range by 34% and the oceanic

range by 7%, in addition to initiating convection earlier over land. This response mirrors classic systematic errors in the GCM representation of the diurnal cycle of convection (e.g., overly frequent triggering and premature onset), indicating that poor representation of local cloud-radiative coupling may actively exacerbate parameterization deficiencies.

The sensitivity of land diurnal rainfall to cloud-radiative interactions was found to increase nonlinearly with terrain height. For terrain exceeding 750 m, the diurnal rain rate range in NCRF was approximately 50% greater than in the control simulation. Because the low-level cloud fraction varies in phase and attenuates solar insolation more effectively than mid- and high-level clouds, its associated cloud-albedo effect more strongly reduces surface shortwave flux over elevated slopes. Consequently, cloud-radiative interactions weaken buoyancy-driven anabatic (upslope) winds and reduce the land-sea thermal contrasts, strongly suppressing diurnal rainfall over high, steep topography. These findings demonstrate the heightened sensitivity of diurnal rainfall over mountainous regions to changes in cloud cover and suggest that the resulting effects can propagate downstream to influence rainfall across entire islands, underscoring the importance of accurately representing cloud-radiative interactions over complex terrain.

We expanded the analysis into the intraseasonal timescale and discovered that cloud-radiative interactions do not explain the intraseasonal land-sea modulation of diurnal rainfall over the western MC. Therefore, chapter 3 investigates the relative impact MJO-induced moisture and wind circulation on the mechanisms responsible for diurnal rainfall using a series of initialization and boundary condition experiments. The land and ocean domains respond differently to MJO-induced environmental changes over the MC. The oceanic diurnal rainfall range closely follows changes in column-integrated moisture (the P-r relationship), where drier environmental conditions associated with the PreMJO phase suppress diurnal rainfall. A weaker direct P-r relationship exists

over land compared to ocean, suggesting that diurnal rainfall is driven instead primarily by mechanical forcing and regional circulation.

Over land, stronger large-scale westerly winds associated with the enhanced phase of the MJO suppress localized diurnal land-sea circulations through enhanced turbulent mixing. The local diurnal coastal thermal gradient weakens due to this enhanced mixing, thereby suppressing diurnal rainfall over the western sides. Conversely, rainfall intensifies over the eastern side of islands upon the onset of the MJO-associated westerly winds. Prior studies suggest that the island "wake-effect" acts to reduce the dampening effect that large-scale winds impose on the diurnal coastal thermal gradient (Qian et al., 2013; Qian, 2020; Zhou et al., 2022).

However, over the eastern side, diurnal rainfall is strongest when the local coastal thermal gradient is weakest, suggesting that the diurnally driven mechanism is not the primary driver of rainfall over the eastern side. The strengthening diurnal rainfall from PreMJO to MJO over the eastern side may instead be explained by tropospheric moistening associated with the onset of the enhanced MJO phase. This deep column moistening dampens dry-air entrainment, helping to shift the preferred terrain-relative position of convection toward the eastern side of the islands as the MJO convective envelope propagates across the region.

While the convection-permitting numerical model framework used in these studies isolated several robust physical mechanisms that modulate the diurnal cycle, certain limitations introduce important avenues for future research. Our simulations focused on a single, well-documented wet-season MJO event in late 2015 under a large-scale easterly background wind regime. Expanding this framework to an ensemble of multi-season MJO events would provide key insights into how diurnal rainfall characteristics and the strength of the proposed mechanisms vary with the seasonal shift in global monsoonal circulation. Future studies should also isolate whether the intraseasonal

increase in diurnal rainfall over eastern-facing terrain is dominated by local triggering within the moistened troposphere, or whether it reflects the physical advection of mesoscale convective systems originating on western terrain faces that cross the central mountain ranges.

The results from this dissertation demonstrate that cloud-radiative interactions provide an important feedback on convective systems by influencing the timing and intensity of the diurnal cycle of rainfall. These findings suggest that biases in cloud production and evolution can directly contribute to errors in the simulated diurnal cycle, highlighting the need for improved cloud representation in numerical weather prediction and climate modes. While prior studies have examined that the sensitivity of the diurnal cycle to convective parameterizations, the feedback cloud-radiative interactions have on the diurnal cycle has received little to no attention before. Future work should investigate how varying convective parameterizations modify cloud characteristics and resulting cloud-radiative feedbacks influence convection. This dissertation also demonstrated that objectively quantifying the spatial evolution of island rainfall provides new insights into the role of MJO-associated background winds in modulating the diurnal cycle prior to the arrival of the MJO enhanced phase. Since diurnal rainfall enhancing over the MC islands before the onset of the MJO enhanced phase has been linked to successful MJO propagation over the MC, objective diagnostics such as developed in chapter 3 provide a valuable framework for evaluating model performance and identifying deficiencies that limit the accurate simulation of MJO propagation. Improving the representation of these processes will ultimately contribute to more reliable weather and climate predictions across the MC and other similarly topographically complex tropical regions.

In conclusion, this dissertation demonstrates that the mechanisms driving the diurnal cycle of rainfall over the MC are strongly modulated by the large-scale dynamics of

the MJO. We have established that topographically constrained low-level cloud cover acts as a critical negative feedback on local thermodynamic forcing by modulating surface shortwave radiation fluxes and dampening diurnal mesoscale circulations over mountains. Concurrently, intraseasonal variations in column-integrated moisture and circulation dictate the spatial distribution and land-to-sea transition of the diurnal cycle of rainfall. Capturing these cross-scale dynamic and thermodynamic interactions within GCMs with parameterized convection remains essential to mitigate structural biases and improve predictive skill across subseasonal-to-seasonal timescales.

Appendix A

Contents of this file

1. Text A.1

2. Figures A.1–A.13

Text A1

To ensure the skew of the diurnal rainfall initiation timing difference between NCRF and CTRL is not strongly influenced by the choice of the rain rate threshold, sensitivity tests were conducted between the value chosen for the rain rate threshold and the amount of skew measured by the Fisher-Pearson's coefficient of skewness. This method measures the asymmetry of a distribution and quantifies how much the distribution deviates from a symmetric normal distribution. The skew was found to always be positive over both land and ocean (right skew, left lean) no matter the threshold used, suggesting a higher probability of earlier initiation of convection for NCRF. Over land, the coefficient minimized (0.16) at a threshold of 0.1 mm/hr and maximized in skew (0.58) as the threshold reached 6.4 mm/hr. At a threshold of 1 mm/hr, the coefficient is 0.23, just slightly above the minimum, suggesting that the threshold of 1 mm/hr is a moderate pick over land. Similarly, over ocean, the coefficient minimized (0.08) at a threshold of 0.1 mm/hr and maximized in skew (0.24) as the threshold reached 5 mm/hr. At a threshold of 1 mm/hr, the coefficient is 0.13, just slightly above the minimum, suggesting that the threshold of 1 mm/hr is a moderate pick over ocean.

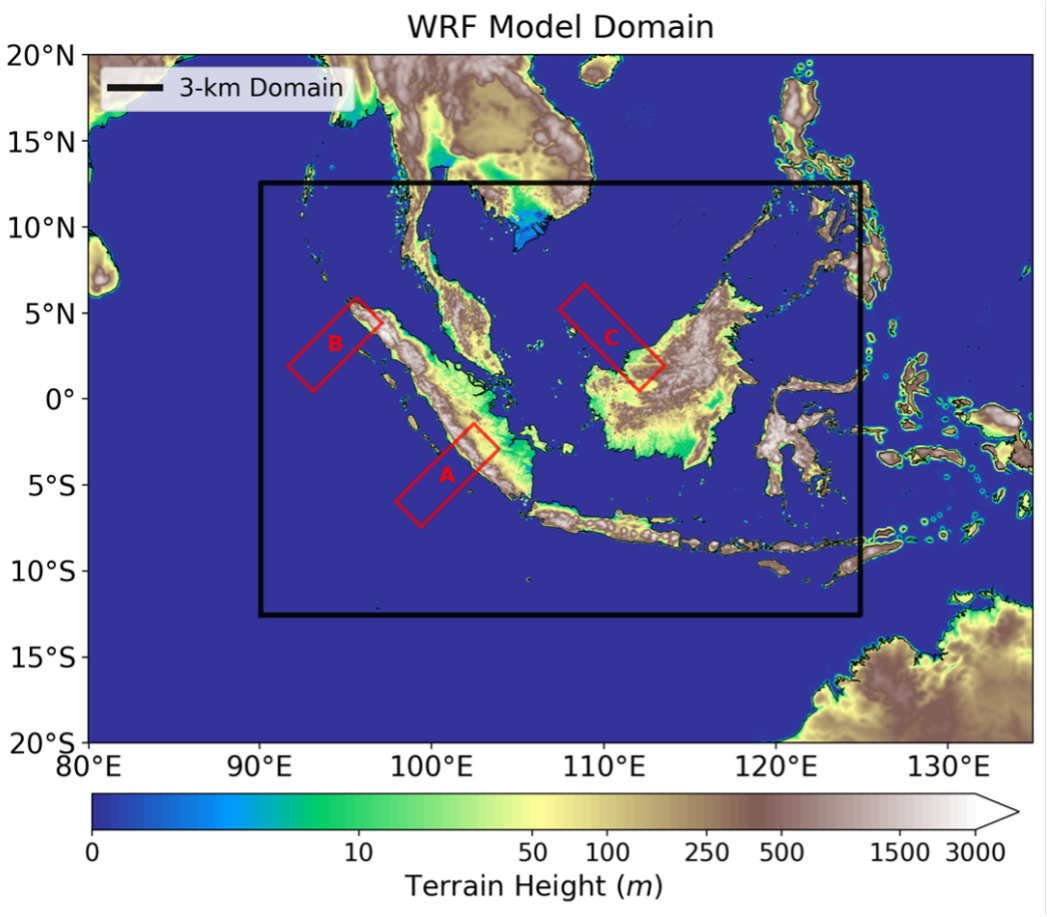

Figure A.1: The WRF model simulation domain is shown, where shading represents terrain height (m), the solid black rectangle represents the high-resolution nested domain (3-km grid spacing), and the three regions where cross-sectional analysis is conducted is overlaid in solid red rectangles and labeled A (Sumatra Mid Central), B (Sumatra Northwest), C (Borneo Northwest).

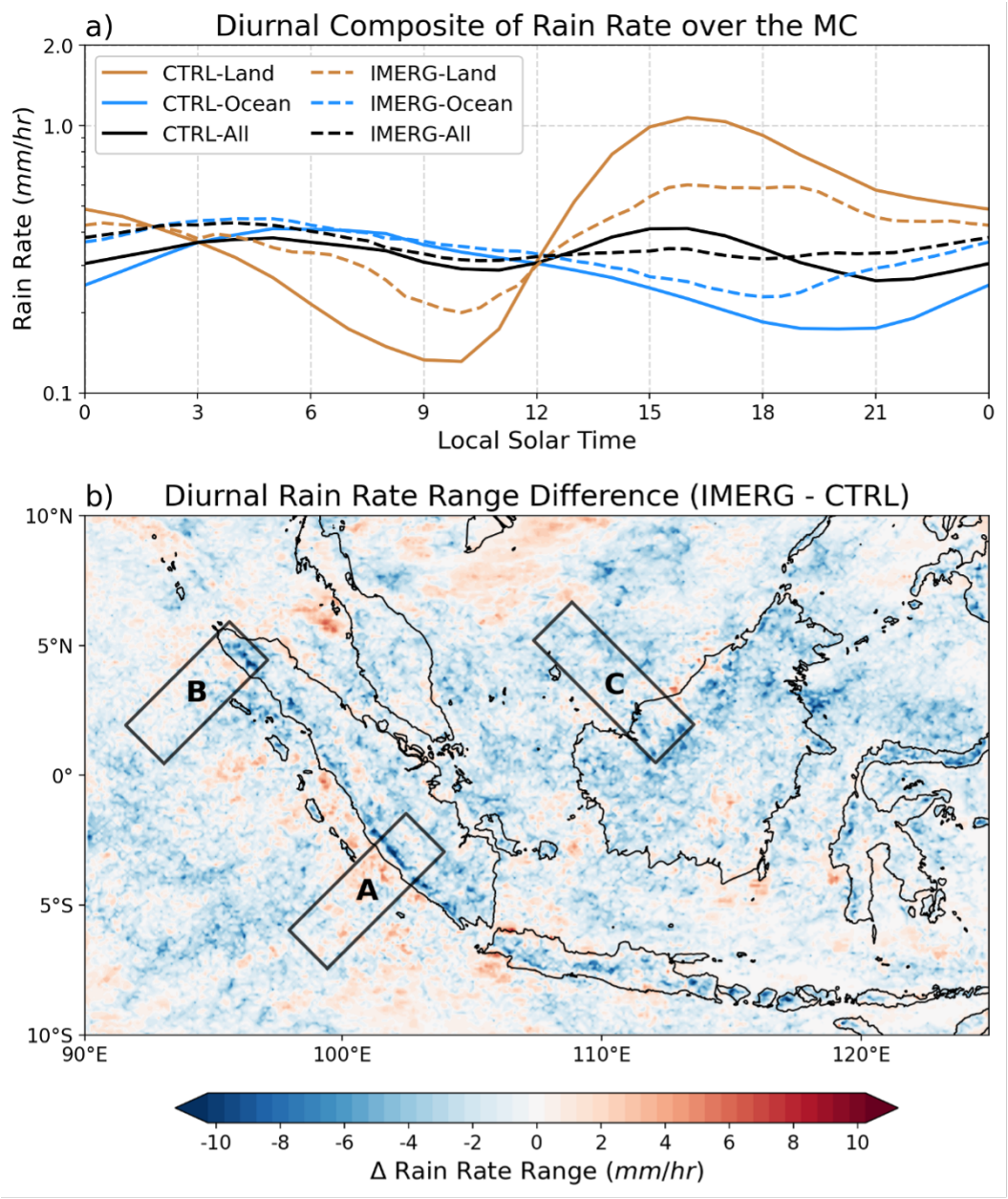

Figure A.2: (a) The domain average ("All") diurnal composite of rain rate (mm/hr, log-scale) is calculated over the MC domain for CTRL (black, solid), and IMERG v7 (black, dashed). It is split into the land (orange) and ocean (blue) domain. (b) The diurnal composite of rain rate range difference between IMERG v7 and CTRL are shown spatially, where red shading indicates greater diurnal range for IMERG and blue shading indicates CTRL has greater range. Three regions where transect analysis is conducted are overlaid in solid black rectangles and labeled A (Sumatra Mid Central), B (Sumatra Northwest), and C (Borneo Northwest).

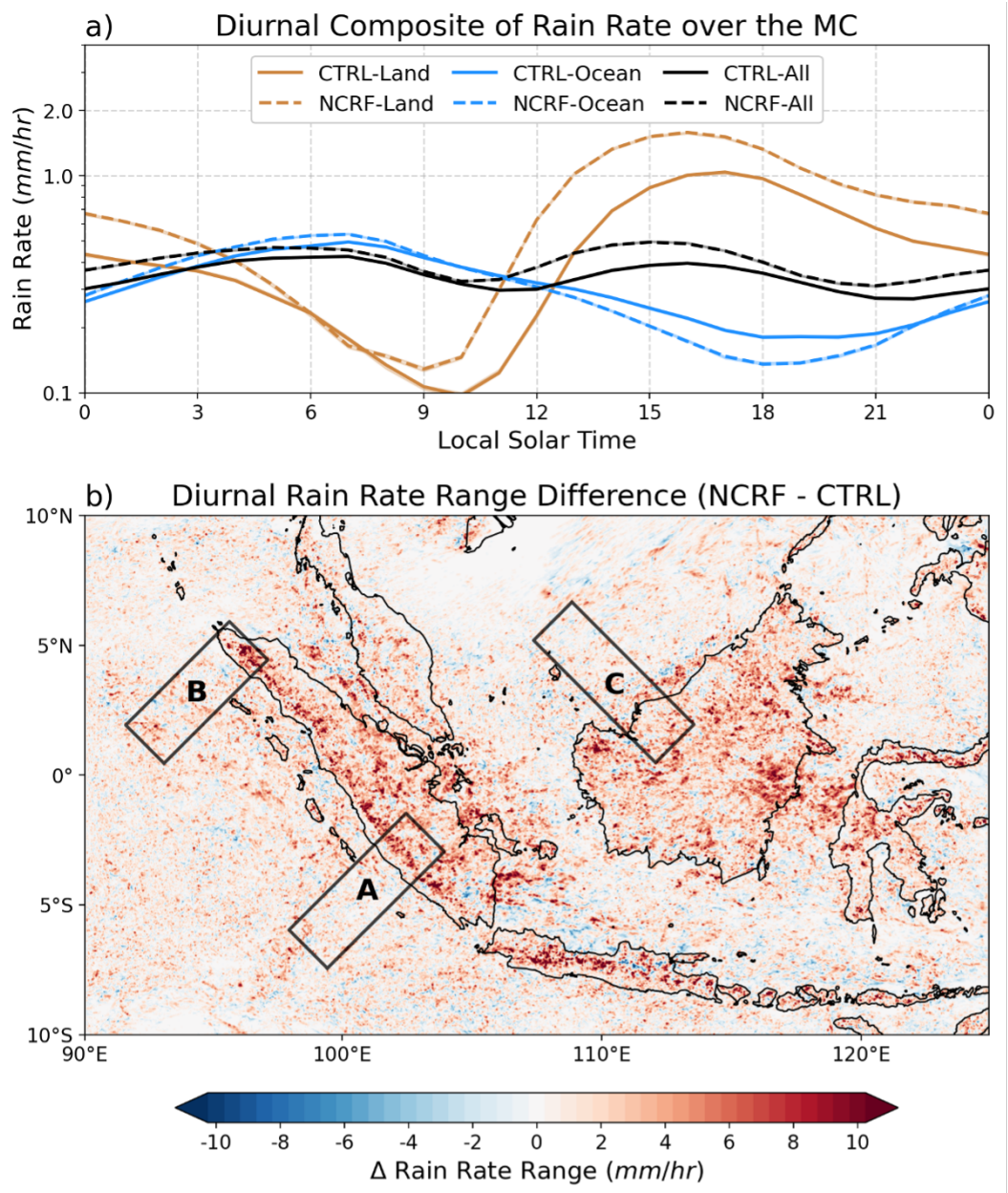

Figure A.3: Same as Fig. 2.1, but for dates December 10-20, 2015.

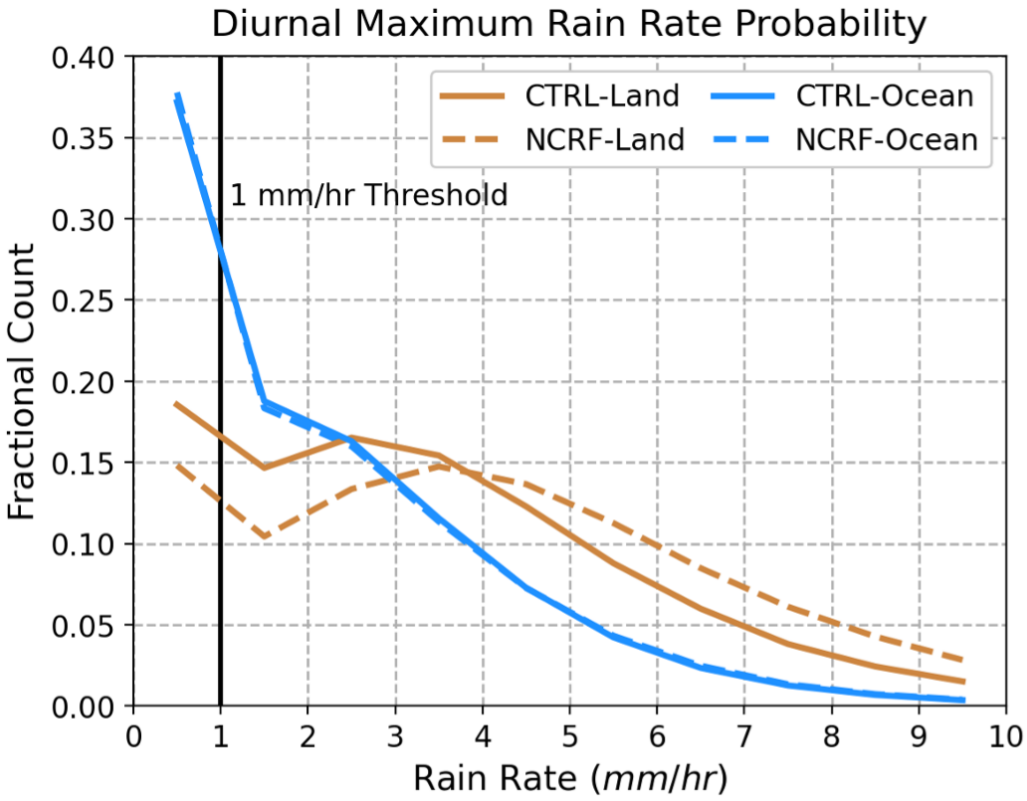

Figure A.4: The maximum diurnal rain rate is calculated over land (orange) and ocean (blue) and compared between CTRL (solid) and NCRF (dashed). Data is binned at a 1 mm/hr interval in the x-axis, and the 1 mm/hr threshold (solid, black) used in the study is plotted for comparison. Fractional count refers to the number of counts in the bin divided by the total number of counts. 81% of CTRL land, 85% of NCRF land, and 62% of CTRL and NCRF ocean data is retained with a 1 mm/hr threshold.

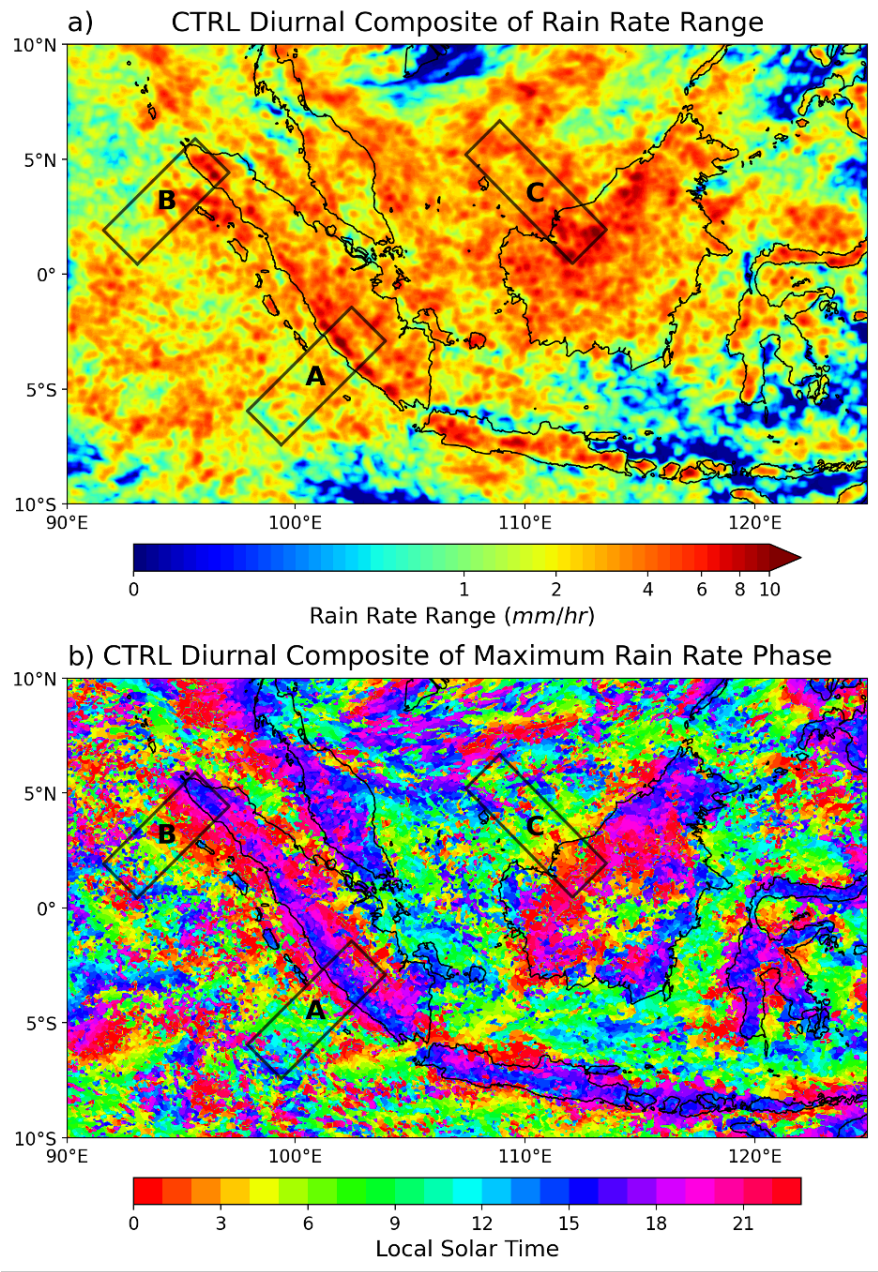

Figure A.5: Utilizing data from CTRL, spatial analysis of (a) the diurnal composite of rain rate range (mm/hr) and (b) the local solar time of when the diurnal composite of rain rate phase maximizes is shown. Rain rates were first spatially smoothed by running a 5-grid point centered moving mean. High rainfall rates exist over regions with high terrain, and frequent occurrence of rain rate ranges exceeding 1 mm/hr over ocean. Additionally, some coastal regions show a smooth gradient of local solar time, suggesting the existence of offshore propagation of convection.

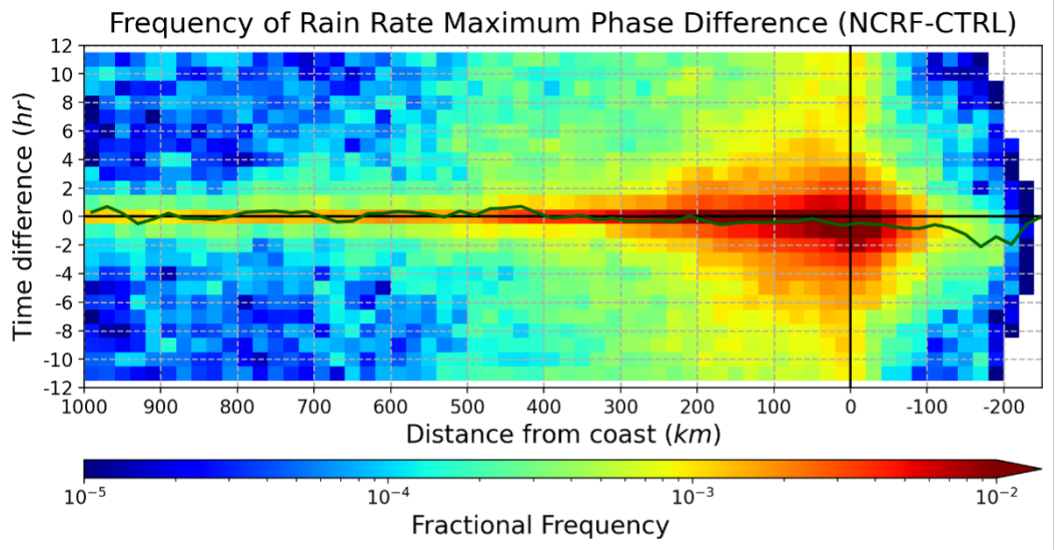

Figure A.6: The fractional frequency distribution of the difference in rain rate phase maximum between simulations ($NCRF-CTRL$) is calculated as a function of distance from coast. Negative distance from coast values represents the land, while positive represents the ocean. The solid green line is the average time difference at each distance from coast bin, where negative represents earlier NCRF diurnal composite rain rate maximum timing compared to CTRL, and positive represents and earlier CTRL timing. Earlier rain rate maximum timing exists over land and up to 150 km into the ocean in NCRF, but becomes indistinguishable past 150 km offshore, suggesting earlier initiation is largely constrained near and over land.

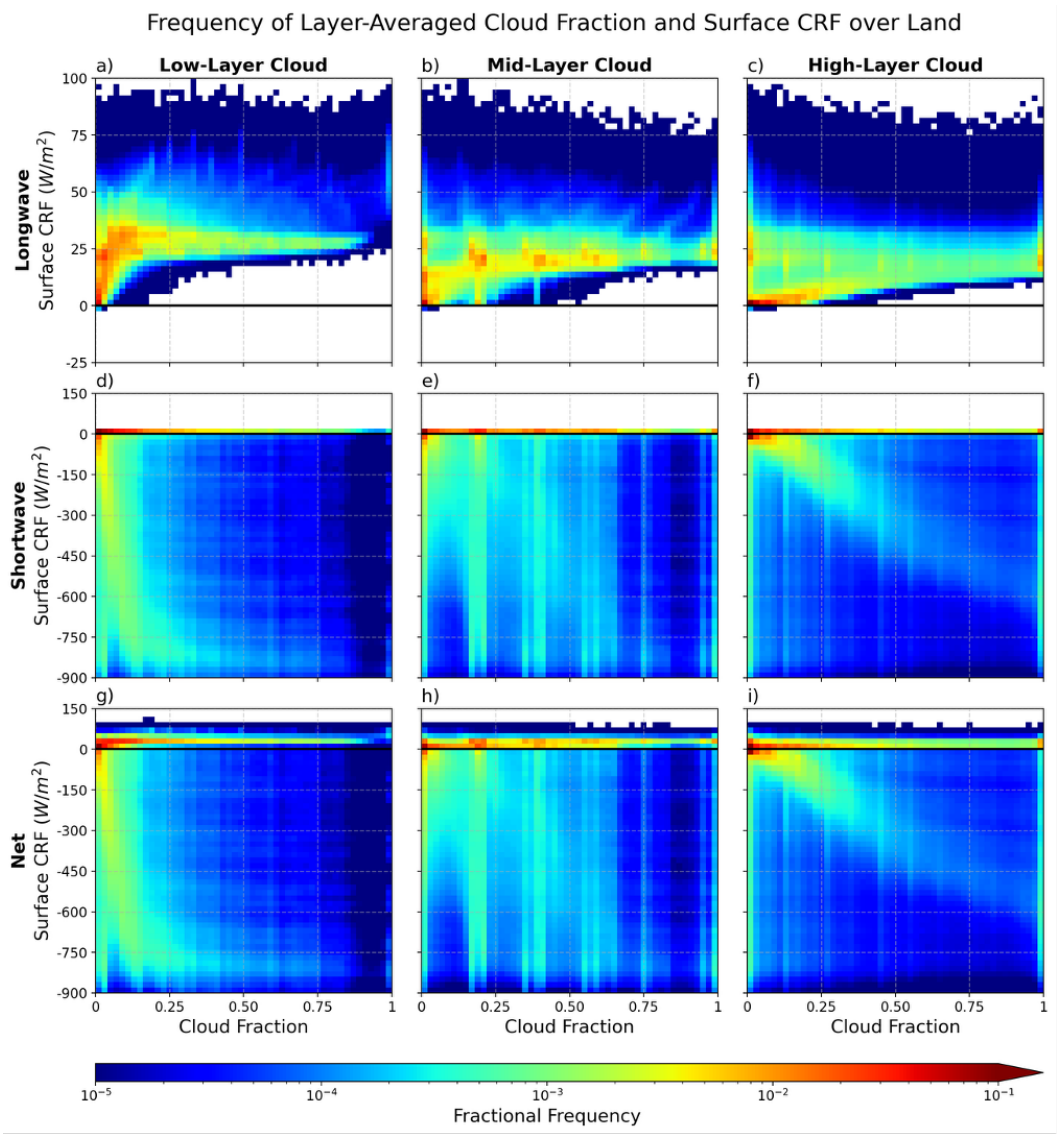

Figure A.7: A frequency distribution between layer-averaged low (a, d, g), mid (b, e, h), and high (c, f, i) cloud fraction and surface cloud-radiative forcing (CRF) in the longwave (a–c), shortwave (d–f) and net (g–i) is conducted over land. The horizontal black line represents the CRF value of zero. Positive CRF values indicate cloud-radiative warming and negative values indicate cloud-radiative cooling at the surface. Data points where cloud fraction was equal to zero were removed.

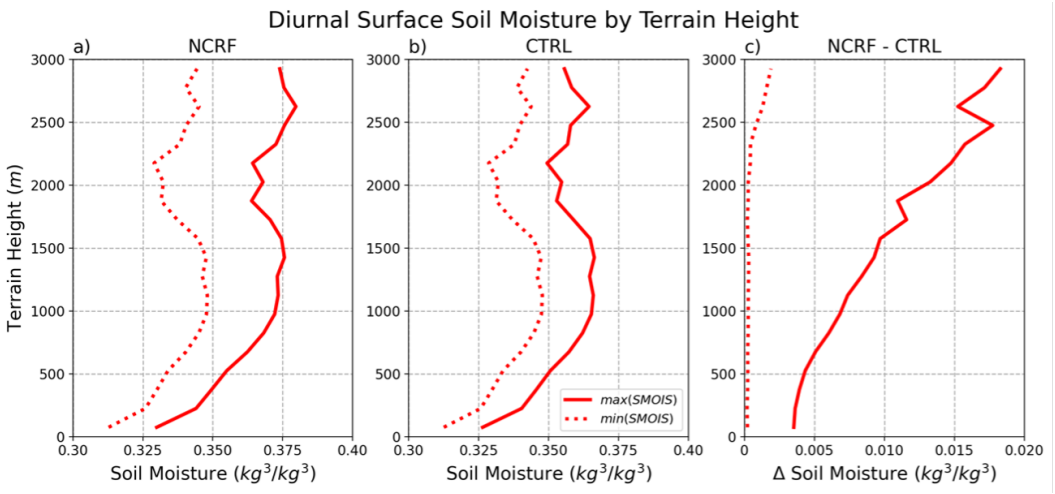

Figure A.8: The maximum (solid) and minimum (dotted) of the diurnal composite of soil moisture (0-0.1m) is averaged at each terrain height bin in (a) NCRF, (b) CTRL, and (c) their difference $NCRF-CTRL$. Minimum soil moisture follows closely between simulations, but the difference in maximum soil moisture deviates increasingly with increasing terrain height. This suggests NCRF soil moisture is moister as terrain height increases compared to CTRL.

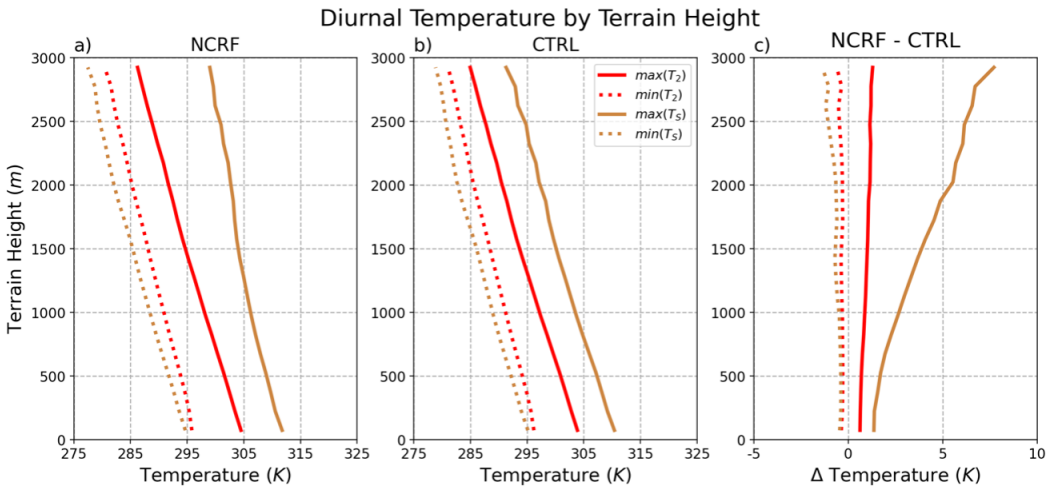

Figure A.9: The maximum (solid) and minimum (dotted) of the diurnal composite 2m temperature (red) and surface temperature (brown) are averaged at each terrain height bin in (a) NCRF, (b) CTRL, and (c) their difference $NCRF - CTRL$. While CTRL surface and 2m temperatures decrease at a constant rate, NCRF maximum surface temperature deviates and decreases at a much slower rate than that of CTRL. The temperature difference between simulations highlights the slower rate of decrease with increasing terrain height, showing NCRF maximum surface temperatures of nearly 7 K greater than CTRL at the highest points. The difference also shows how minimum temperatures are slightly cooler in NCRF, likely due to the absence of longwave trapping at nighttime.

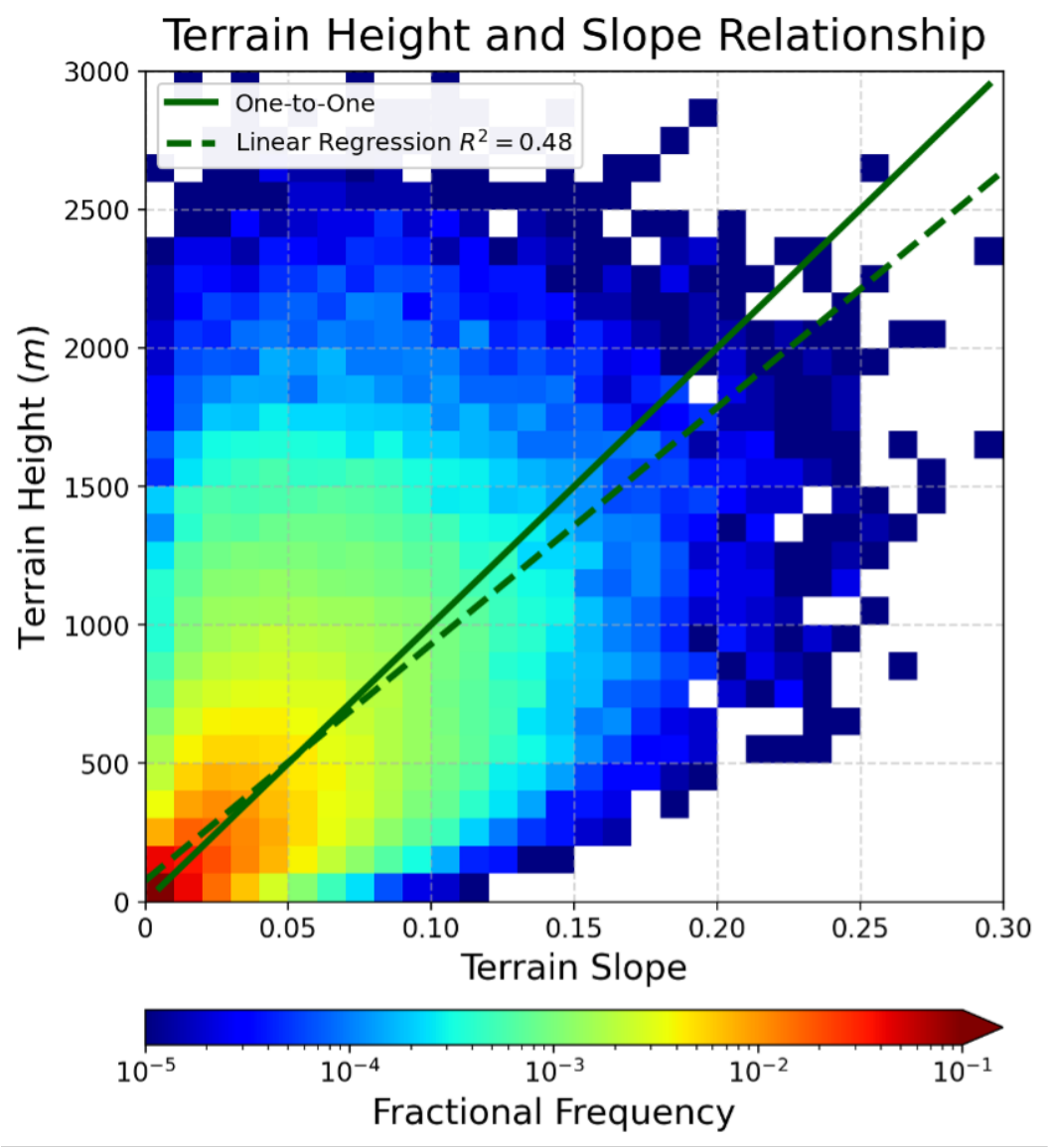

Figure A.10: The fractional frequency of occurrence of the terrain height (m) and terrain height slope (unitless) is conducted (shading), normalized such that the sum over x and y dimensions equal one. The best-fit line is plotted in dashed green after finding the linear relationship between both variables, along with a reference one-to-one line. The best-fit line closely follows the one-to-one line, along with a relatively high R^2 value, both suggesting that terrain slope and terrain height are linearly correlated.

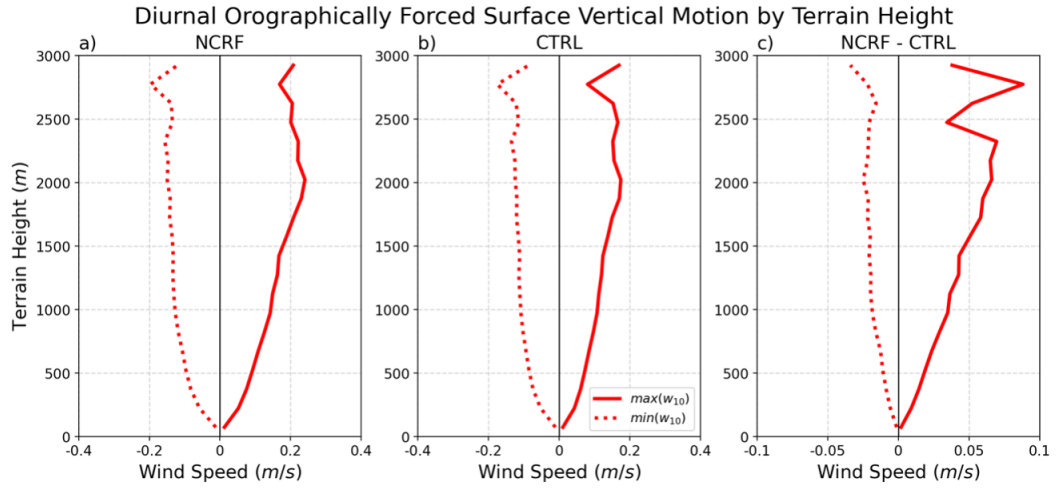

Figure A.11: The maximum (solid) and minimum (dotted) of the diurnal composite 10-m orographically forced surface vertical motion (m/s) are averaged at each terrain height bin in (a) NCRF, (b) CTRL, and (c) their difference $NCRF - CTRL$. Both the maximum and minimum increasingly diverge from 0 with increasing terrain height in both simulations. The difference between NCRF and CTRL show both differences in the maximum and minimum nearly equally contributing to the higher NCRF range compared to CTRL. The maximum in NCRF is significantly higher than CTRL, suggesting that upslope/anabatic winds see a greater increase compared to downslope/katabatic winds.

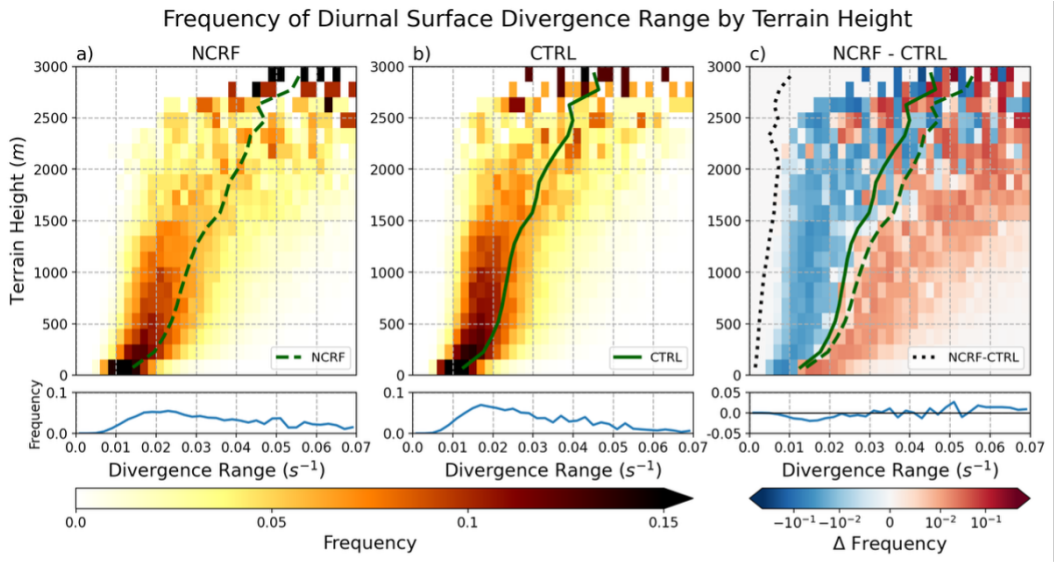

Figure A.12: The frequency distribution of the diurnal range of 10-m wind divergence $(1/s)$ as a function of terrain height (m) over land, normalized by the terrain height bin, for (a) NCRF, (b) CTRL, and (c) their difference $NCRF-CTRL$. Corresponding average surface divergence range (green) at each terrain height bin is overlaid NCRF (dashed) in (a), CTRL (solid) in (b), and their difference (black, dotted) in (c). Terrain averaged frequency (a, b) and anomalous frequency (c) of divergence range is plotted below the heat maps (blue, solid).

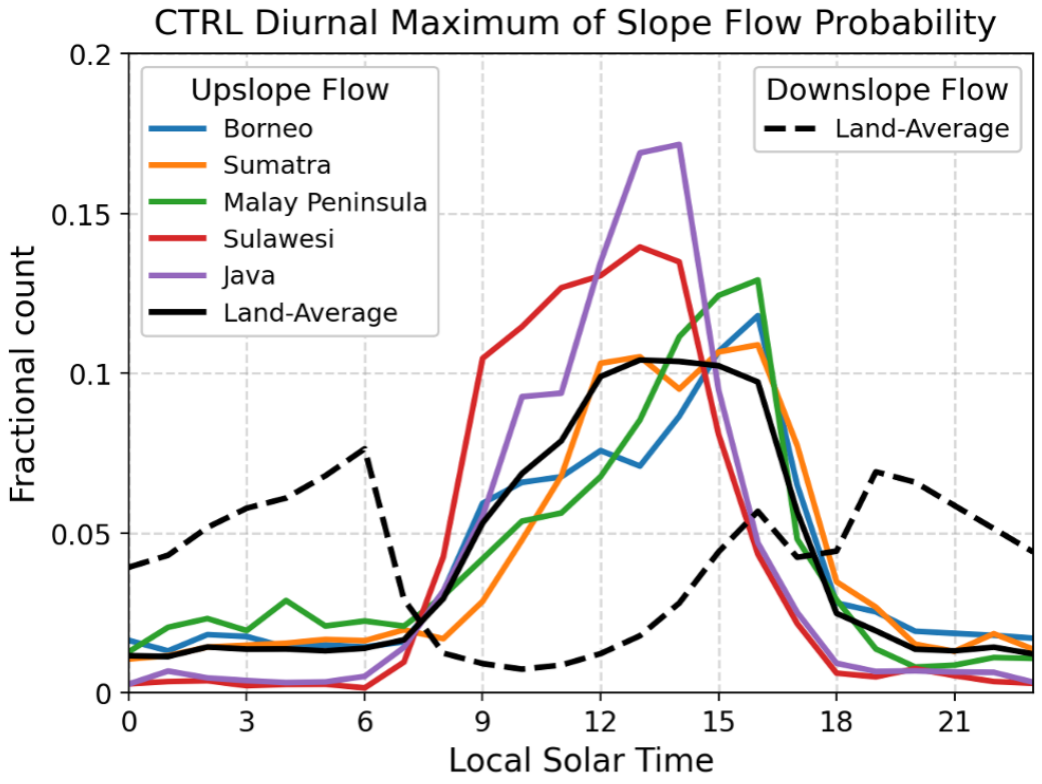

Figure A.13: The local solar time of when CTRL diurnal slope flow maximizes is show w.r.t. upslope and downslope flow. Fractional count refers to the number of counts in the bin divided by the total number of counts. Upslope flow maximizes over all land points around 12-16 LST, while downslope flow maximizes at 6 LST with a local maximum at 19 LST that likely is associated with precipitation downdrafts and cold pools over terrain.

Appendix B

Contents of this file

1. Figures B.1–B.3

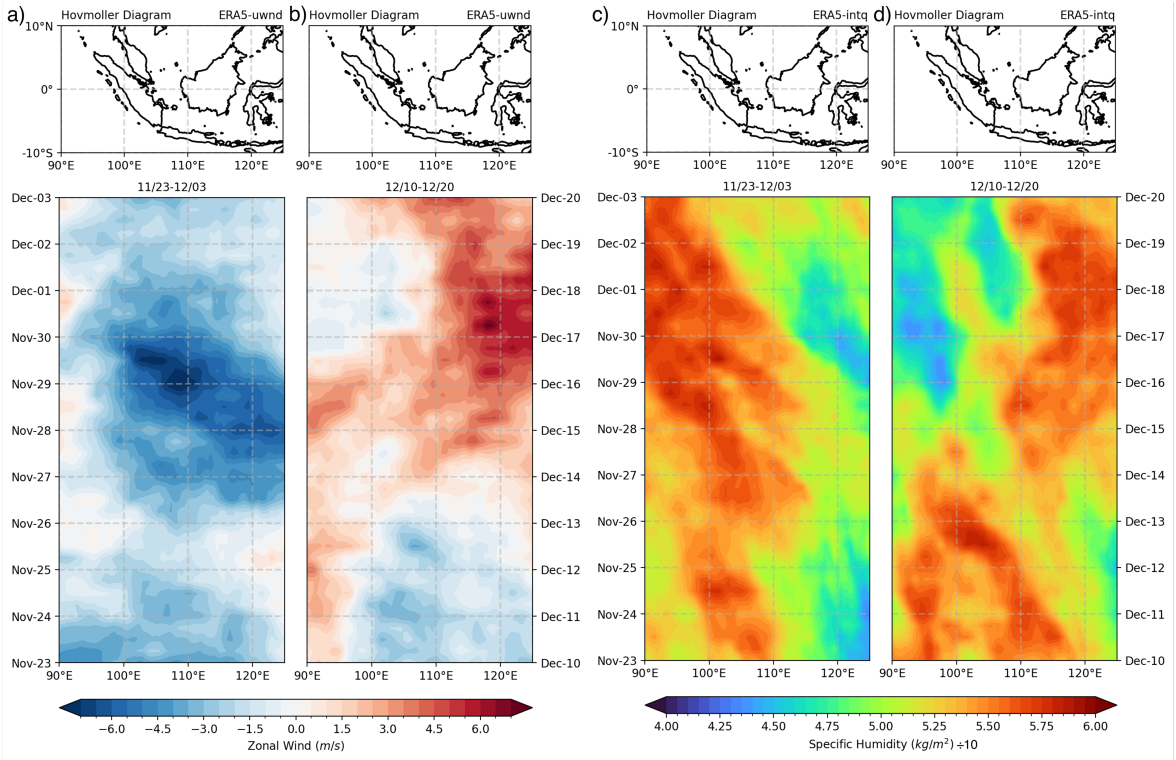

Figure B.1: The fifth generation ECMWF atmospheric reanalysis (ERA5) data set of (a,b) zonal wind (m/s) and (c,d) specific humidity (kg/kg), time series averaged latitudinally (10°S-10°N) over the western Maritime Continent (MC) domain for both (a,c) $PreMJO$ and (b,d) MJO time periods.

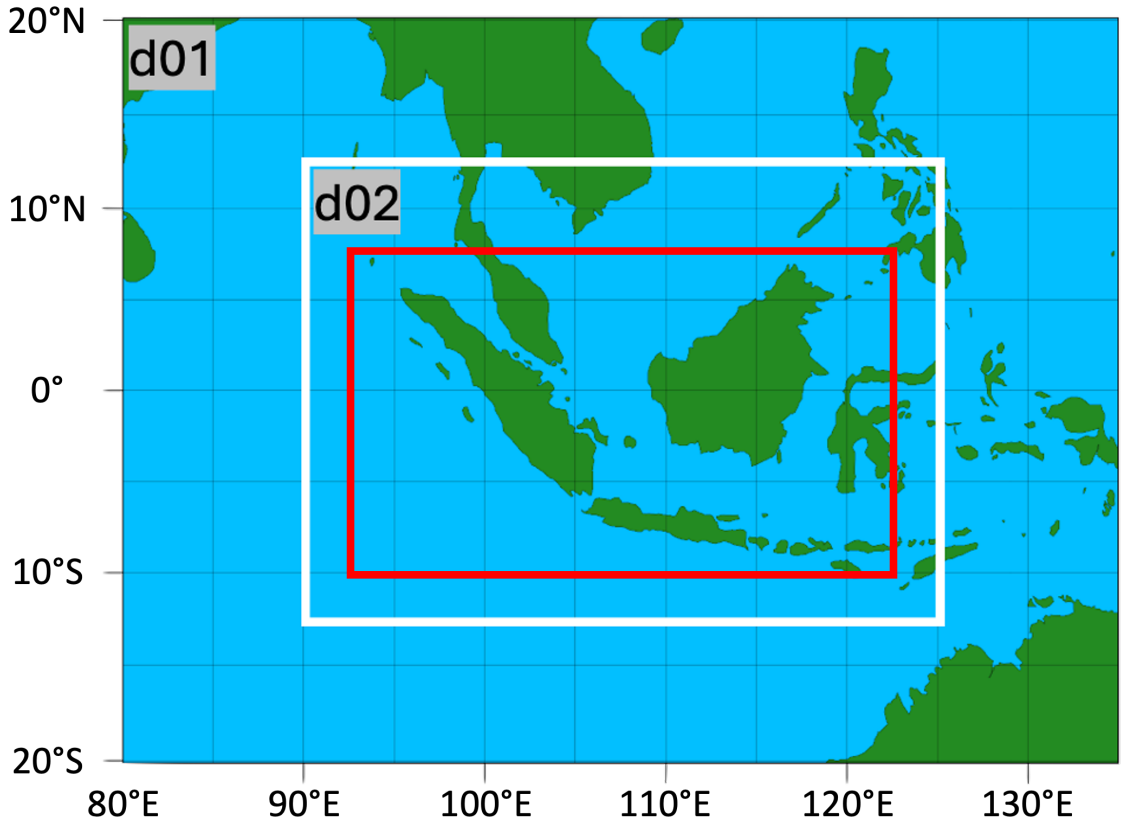

Figure B.2: The outer (d01), inner (d02, white), and the domain analysis nest (red) is shown.

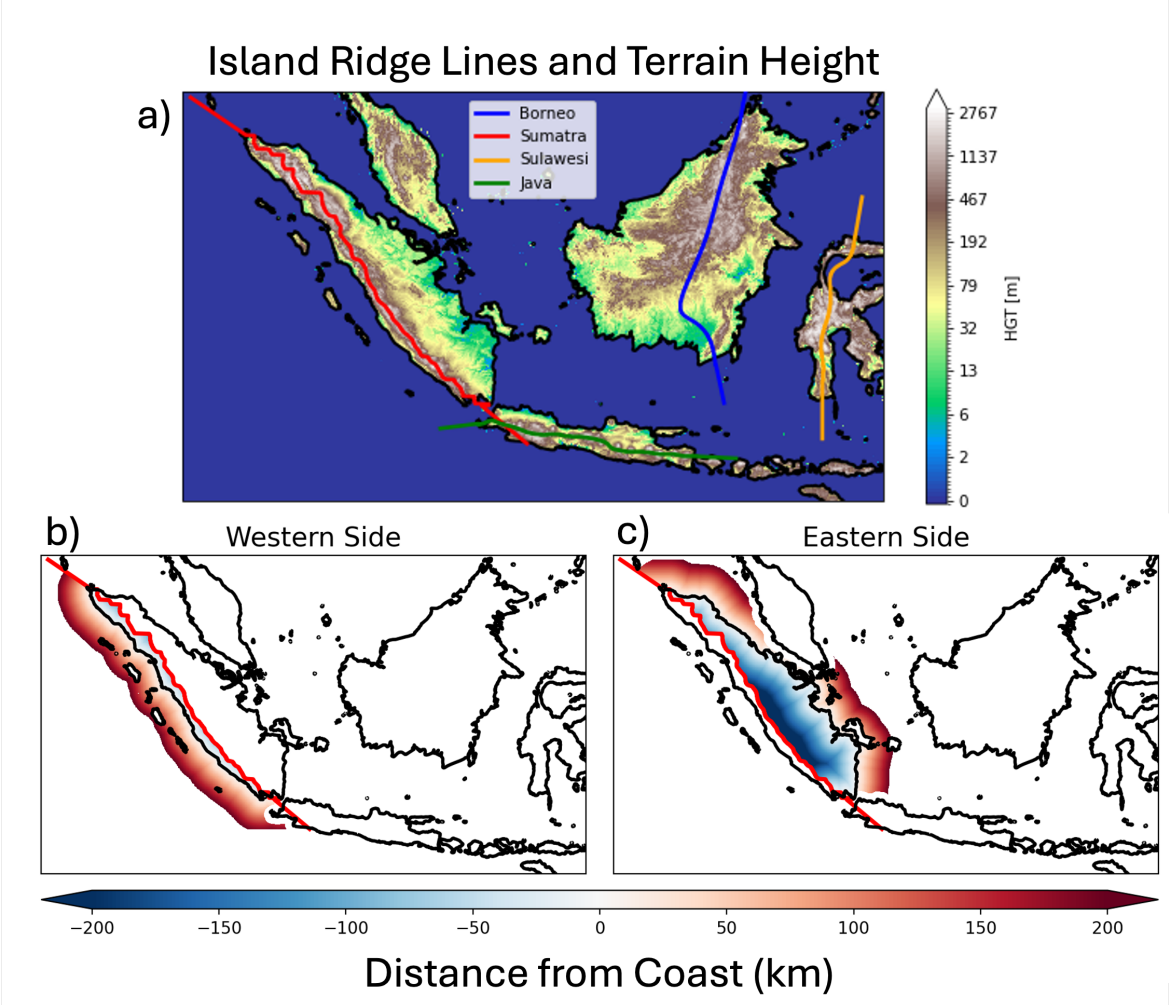

Figure B.3: (a) Terrain height (m, log-scale) is shown in the color contour, with an overlay of the ridge line used to divide the islands into their western/eastern (southern/northern for Java) counterparts. The island of Sumatra is used as an example to show the distance from coast (km) values over the (b) western and (c) eastern sides of the ridge lines.

Reference List

Ahmed, F., and C. Schumacher, 2017: Geographical differences in the tropical precipitation-moisture relationship and rain intensity onset. *Geophysical Research Letters*, **44**, 1114–1122, https://doi.org/10.1002/2016GL071980.

Bai, H., and C. Schumacher, 2022: Topographic influences on diurnally driven mjo rainfall over the maritime continent. *Journal of Geophysical Research: Atmospheres*, **127**, https://doi.org/10.1029/2021JD035905.

Bergemann, M., and C. Jakob, 2016: How important is tropospheric humidity for coastal rainfall in the tropics? Blackwell Publishing Ltd, 5860-5868 pp., https://doi.org/10.1002/2016GL069255.

Boucher, O., and Coauthors, 2013: *Clouds and Aerosols. In: Climate Change 2013: The Physical Science Basis. Contribution of Working Group I to the Fifth Assessment Report of the Intergovernmental Panel on Climate Change*. Cambridge University Press, 571-657 pp., https://doi.org/10.1017/CBO9781107415324.016.

Bretherton, C. S., M. E. Peters, and L. E. Back, 2004: Relationships between water vapor path and precipitation over the tropical oceans. *Journal of climate*, **17**, 1517–1528, https://doi.org/https://doi.org/10.1175/1520-0442(2004)017⟨1517:RBWVPA⟩2.0.CO;2.

Burleyson, C. D., C. N. Long, and J. M. Comstock, 2015: Quantifying diurnal cloud radiative effects by cloud type in the tropical western pacific. *Journal of Applied Meteorology and Climatology*, **54**, 1297–1312, https://doi.org/10.1175/JAMC-D-14-0288.1.

Chen, G., J. Ling, R. Zhang, Z. Xiao, and C. Li, 2022: The mjo from cmip5 to cmip6: Perspectives from tracking mjo precipitation. *Geophysical Research Letters*, **49**, https://doi.org/10.1029/2021GL095241.

Christopoulos, C., and T. Schneider, 2021: Assessing biases and climate implications of the diurnal precipitation cycle in climate models. *Geophysical Research Letters*, **48**, https://doi.org/10.1029/2021GL093017.

Coppin, D., and G. Bellon, 2019: Physical mechanisms controlling the offshore propagation of convection in the tropics: 1. flat island. *Journal of Advances in Modeling Earth Systems*, **11**, 3042–3056, https://doi.org/10.1029/2019MS001793.

Dai, A., X. Lin, and K. L. Hsu, 2007: The frequency, intensity, and diurnal cycle

of precipitation in surface and satellite observations over low- and mid-latitudes. *Climate Dynamics*, **29**, 727–744, https://doi.org/10.1007/s00382-007-0260-y.

Ding, S., X. Chen, X. Zhang, X. Zhang, and P. Xu, 2024: A review on the arctic–midlatitudes connection: Interactive impacts, physical mechanisms, and nonstationary. Multidisciplinary Digital Publishing Institute (MDPI), https://doi.org/10.3390/atmos15091115.

Dong, W., J. P. Krasting, and H. Guo, 2023: Analysis of precipitation diurnal cycle and variance in multiple observations, cmip6 models, and a series of gfdl-am4.0 simulations. *Journal of Climate*, **36**, 8637–8655, https://doi.org/10.1175/JCLI-D-23, URL https://doi.org/10.1175/JCLI-D-23-.

Ek, M. B., K. E. Mitchell, Y. Lin, E. Rogers, P. Grunmann, V. Koren, G. Gayno, and J. D. Tarpley, 2003: Implementation of noah land surface model advances in the national centers for environmental prediction operational mesoscale eta model. *Journal of Geophysical Research: Atmospheres*, **108**, https://doi.org/10.1029/2002jd003296.

Forsythe, N., A. J. Hardy, H. J. Fowler, S. Blenkinsop, C. G. Kilsby, D. R. Archer, and M. Z. Hashmi, 2015: A detailed cloud fraction climatology of the upper indus basin and its implications for near-surface air temperature*. *Journal of Climate*, 3537–3556, https://doi.org/10.1175/JCLI-D-14-00505.s1, URL http://dx.doi.org/10.1175/JCLI-D-14-00505.s1.

Fujita, M., K. Yoneyama, S. Mori, T. Nasuno, and M. Satoh, 2011: Diurnal convection peaks over the eastern indian ocean off sumatra during different mjo phases. *Journal of the Meteorological Society of Japan*, **89**, 317–330, https://doi.org/10.2151/jmsj.2011-A22.

Hersbach, H., and Coauthors, 2020: The era5 global reanalysis. *Quarterly Journal of the Royal Meteorological Society*, **146**, 1999–2049, https://doi.org/10.1002/qj.3803.

Hohenegger, C., and B. Stevens, 2022: Tropical continents rainier than expected from geometrical constraints. *AGU Advances*, **3**, https://doi.org/10.1029/2021AV000636.

Holloway, C. E., and D. J. Neelin, 2009: Moisture vertical structure, column water vapor, and tropical deep convection. *Journal of the Atmospheric Sciences*, **66**, 1665–1683, https://doi.org/10.1175/2008JAS2806.1.

Huffman, G. J., and Coauthors, 2023: Algorithm theoretical basis document (atbd) nasa global precipitation measurement (gpm) integrated multi-satellite retrievals for gpm (imerg) version 07. *Algorithm Theoretical Basis Document (ATBD) Version*, **47**.

Iacono, M. J., J. S. Delamere, E. J. Mlawer, M. W. Shephard, S. A. Clough, and W. D. Collins, 2008: Radiative forcing by long-lived greenhouse gases: Calculations with the aer radiative transfer models. *Journal of Geophysical Research Atmospheres*, **113**, https://doi.org/10.1029/2008JD009944.

Ichikawa, H., 2006: Time-space characteristics of diurnal rainfall over borneo and surrounding oceans as observed by trmm-pr. Tech. rep.

Jiang, X., and Coauthors, 2020: Fifty years of research on the madden-julian oscillation: Recent progress, challenges, and perspectives. *Journal of Geophysical Research: Atmospheres*, **125**, 1–64, https://doi.org/10.1029/2019JD030911, URL https://doi.org/10.1029/2019JD030911.

Kikuchi, K., and B. Wang, 2008: Diurnal precipitation regimes in the global tropics. *Journal of Climate*, **21**, 2680–2696, https://doi.org/10.1175/2007JCLI2051.1.

Kiladis, G. N., J. Dias, K. H. Straub, M. C. Wheeler, S. N. Tulich, K. Kikuchi, K. M. Weickmann, and M. J. Ventrice, 2014: A comparison of olr and circulation-based indices for tracking the mjo. *Monthly Weather Review*, **142**, 1697–1715, https://doi.org/10.1175/MWR-D-13-00301.1.

L'Ecuyer, T. S., Y. Hang, A. V. Matus, and Z. Wang, 2019: Reassessing the effect of cloud type on earth's energy balance in the age of active spaceborne observations. part i: Top of atmosphere and surface. *Journal of Climate*, **32**, 6197–6217, https://doi.org/10.1175/JCLI-D-18-0753.1.

Lim, K. S. S., and S. Y. Hong, 2010: Development of an effective double-moment cloud microphysics scheme with prognostic cloud condensation nuclei (ccn) for weather and climate models. *Monthly Weather Review*, **138**, 1587–1612, https://doi.org/10.1175/2009MWR2968.1.

Ling, J., C. Zhang, R. Joyce, P. ping Xie, and G. Chen, 2019: Possible role of the diurnal cycle in land convection in the barrier effect on the mjo by the maritime continent. *Geophysical Research Letters*, **46**, 3001–3011, https://doi.org/10.1029/2019GL081962.

Lopez-Bravo, C., C. L. Vincent, Y. Huang, and T. P. Lane, 2023: The diurnal cycle of rainfall and deep convective clouds around sumatra and the associated mjo-induced variability during austral summer in himawari-8. *Journal of Geophysical Research: Atmospheres*, **128**, https://doi.org/10.1029/2023JD039132.

Love, B. S., A. J. Matthews, and G. M. Lister, 2011: The diurnal cycle of precipitation over the maritime continent in a high-resolution atmospheric model. *Quar-*

terly Journal of the Royal Meteorological Society, **137**, 934–947, https://doi.org/10.1002/qj.809.

Lu, J., T. Li, and X. Shen, 2023: Precipitation diurnal cycle over the maritime continent modulated by enso. *Climate Dynamics*, **61**, 2547–2564, https://doi.org/10.1007/s00382-023-06699-6.

Lu, J., T. Li, and L. Wang, 2019: Precipitation diurnal cycle over the maritime continent modulated by the mjo. *Climate Dynamics*, **53**, 6489–6501, https://doi.org/10.1007/s00382-019-04941-8.

Luo, H., and M. Yanai, 1983: The large-scale circulation and heat sources over the tibetan plateau and surrounding areas during the early summer of 1979. part i: Precipitation and kinematic analyses. *Monthly Weather Review*, **111**, 922–944, https://doi.org/https://doi.org/10.1175/1520-0493(1983)111⟨0922:TLSCAH⟩2.0.CO;2.

Madden, R., and P. Julian, 1971: Detection of a 40–50 day oscillation in the zonal wind in the tropical pacific. *Journal of the Atmospheric Sciences*, **28**, https://doi.org/10.1175/1520-0469(1971)028⟨0702:doadoi⟩2.0.co;2.

Mapes, B. E., T. T. Warner, and M. Xu, 2003: Diurnal patterns of rainfall in northwestern south america. part iii: Diurnal gravity waves and nocturnal convection offshore. *Monthly Weather Review*, URL https://doi.org/10.1175/1520-0493(2003)131⟨0830:DPORIN⟩2.0.CO;2.

Matus, A. V., and T. S. L'Ecuyer, 2017: The role of cloud phase in earth's radiation budget. *Journal of Geophysical Research*, **122**, 2559–2578, https://doi.org/10.1002/2016JD025951.

Najarian, H., J. Ruppert, and N. Sakaeda, 2025: The influence of cloud-radiative interactions on the diurnal cycle over the maritime continent. *Journal of Geophysical Research: Atmospheres*, **130**, https://doi.org/10.1029/2025JD044512.

Najarian, H., and N. Sakaeda, 2023: The influence of cloud types on cloud-radiative forcing during dynamo/amie. *Journal of Geophysical Research: Atmospheres*, **128**, https://doi.org/10.1029/2022JD038006, URL https://agupubs.onlinelibrary.wiley.com/doi/10.1029/2022JD038006.

Natoli, M. B., and E. D. Maloney, 2023a: Environmental controls on the tropical island diurnal cycle in the context of intraseasonal variability. *Journal of Climate*, **36**, 7465–7485, https://doi.org/10.1175/JCLI-D-22-0824.1.

Natoli, M. B., and E. D. Maloney, 2023b: The tropical diurnal cycle under varying states of the monsoonal background wind. *Journal of the Atmospheric Sciences*, **80**, 235–258, https://doi.org/10.1175/JAS-D-22-0045.1.

Oh, J. H., K. Y. Kim, and G. H. Lim, 2012: Impact of mjo on the diurnal cycle of rainfall over the western maritime continent in the austral summer. *Climate Dynamics*, **38**, 1167–1180, https://doi.org/10.1007/s00382-011-1237-4.

Peatman, S. C., C. E. Birch, J. Schwendike, J. H. Marsham, E. Howard, S. J. Woolnough, J. M. Mustafa, and A. J. Matthews, 2025: Physical controls on the variability of offshore propagation of convection from sumatra. *Journal of Geophysical Research: Atmospheres*, **130**, https://doi.org/10.1029/2024JD042458.

Peatman, S. C., A. J. Matthews, and D. P. Stevens, 2014: Propagation of the madden-julian oscillation through the maritime continent and scale interaction with the diurnal cycle of precipitation. *Quarterly Journal of the Royal Meteorological Society*, **140**, 814–825, https://doi.org/10.1002/qj.2161.

Peters, O., and J. D. Neelin, 2006: Critical phenomena in atmospheric precipitation. *Nature physics*, **2 (6)**, 393–396.

Qian, J. H., 2020: Mechanisms for the dipolar patterns of rainfall variability over large islands in the maritime continent associated with the madden-julian oscillation. *Journal of the Atmospheric Sciences*, **77**, 2257–2278, https://doi.org/10.1175/JAS-D-19-0091.1.

Qian, J. H., A. W. Robertson, and V. Moron, 2010: Interactions among enso, the monsoon, and diurnal cycle in rainfall variability over java, indonesia. *Journal of the Atmospheric Sciences*, **67**, 3509–3524, https://doi.org/10.1175/2010JAS3348.1.

Qian, J. H., A. W. Robertson, and V. Moron, 2013: Diurnal cycle in different weather regimes and rainfall variability over borneo associated with enso. *Journal of Climate*, **26**, 1772–1790, https://doi.org/10.1175/JCLI-D-12-00178.1.

Qian, T., C. C. Epifanio, and F. Zhang, 2012: Topographic effects on the tropical land and sea breeze. *Journal of the Atmospheric Sciences*, **69**, 130–149, https://doi.org/10.1175/JAS-D-11-011.1.

Ramadhan, R., M. Marzuki, W. Suryanto, S. Sholihun, H. Yusnaini, and R. Muharsyah, 2024: Validating imerg data for diurnal rainfall analysis across the indonesian maritime continent using gauge observations. *Remote Sensing Applications: Society and Environment*, **34**, https://doi.org/10.1016/j.rsase.2024.101186.

Rampanelli, G., D. Zardi, and R. Rotunno, 2004: Mechanisms of up-valley winds. *Journal of the Atmospheric Sciences*, **61**, 3097–3111, https://doi.org/https://doi.org/10.1175/JAS-3354.1.

Rauniyar, S. P., and K. J. Walsh, 2011: Scale interaction of the diurnal cycle of rainfall over the maritime continent and australia: Influence of the mjo. *Journal of Climate*, **24**, 325–348, https://doi.org/10.1175/2010JCLI3673.1.

Ray, P., and C. Zhang, 2010: A case study of the mechanics of extratropical influence on the initiation of the madden-julian oscillation. *Journal of the Atmospheric Sciences*, **67**, 515–528, https://doi.org/10.1175/2009JAS3059.1.

Riley, E., B. E. Mapes, and S. N. Tulich, 2011: Clouds associated with the madden-julian oscillation: A new perspective from cloudsat. *Journal of the Atmospheric Sciences*, **68**, 3032–3051, https://doi.org/10.1175/JAS-D-11-030.1.

Ruppert, J. H., and X. Chen, 2020: Island rainfall enhancement in the maritime continent. *Geophysical Research Letters*, **47**, no, https://doi.org/10.1029/2019GL086545.

Ruppert, J. H., and C. Hohenegger, 2018: Diurnal circulation adjustment and organized deep convection. *Journal of Climate*, **31**, 4899–4916, https://doi.org/10.1175/JCLI-D-17-0693.1.

Ruppert, J. H., and F. Zhang, 2019: Diurnal forcing and phase locking of gravity waves in the maritime continent. *Journal of the Atmospheric Sciences*, https://doi.org/10.1175/JAS-D-19, URL https://doi.org/10.1175/JAS-D-19-0061.1.

Sakaeda, N., G. Kiladis, and J. Dias, 2017: The diurnal cycle of tropical cloudiness and rainfall associated with the madden-julian oscillation. *Journal of Climate*, **30**, 3999–4020, https://doi.org/10.1175/JCLI-D-16-0788.1.

Sakaeda, N., G. Kiladis, and J. Dias, 2020: The diurnal cycle of rainfall and the convectively coupled equatorial waves over the maritime continent. *Journal of Climate*, **33**, 3307–3331, https://doi.org/10.1175/JCLI-D-19-0043.1, URL https://doi.org/10.1175/JCLI-D-19-0043.1.

Sari, A. Y., M. Marzuki, M. Vonnisa, R. Ramadhan, H. Yusnaini, R. Muharsyah, and A. Erajalita, 2024: Comparison of climatology of precipitation diurnal cycle in kalimantan deduced from rain gauge and imerg data. *Journal of Physics: Conference Series*, Institute of Physics, Vol. 2866, https://doi.org/10.1088/1742-6596/2866/1/012070.

Schmidt, L., and C. Hohenegger, 2024: Precipitation enhancement over tropical land

through the lens of the moisture–precipitation relationship. *Quarterly Journal of the Royal Meteorological Society*, **150**, 4737–4749, https://doi.org/10.1002/qj.4838.

Segal, M., J. Song, R. Pielke, J. Purdom, and Y. Mahrer, 1986: Evaluation of cloud shading effects on the generation and modification of mesoscale circulations. *Monthly weather review*, **114 (7)**, 1201–1212.

Shige, S., Y. Nakano, and M. K. Yamamoto, 2017: Role of orography, diurnal cycle, and intraseasonal oscillation in summer monsoon rainfall over the western ghats and myanmar coast. *Journal of Climate*, **30 (23)**, 9365–9381.

Short, E., C. L. Vincent, and T. P. Lane, 2019: Diurnal cycle of surface winds in the maritime continent observed through satellite scatterometry. *Monthly Weather Review*, **147**, 2023–2044, https://doi.org/10.1175/MWR-D-18-0433.1.

Skamarock, W. C., and Coauthors, 2021: A description of the advanced research wrf model version 4.3. Tech. rep., National Center for Atmospheric Research. URL http://library.ucar.edu/research/publish-technote.

Sui, C.-H., K.-M. Lau, Y. N. Takayabu, and D. A. Short, 1997: Diurnal variations in tropical oceanic cumulus convection during toga coare. *Journal of the Atmospheric Sciences*, 639–655, https://doi.org/https://doi.org/10.1175/1520-0469(1997)054⟨0639:DVITOC⟩2.0.CO;2.

Tan, H., P. Ray, B. Barrett, J. Dudhia, M. Moncrieff, L. Zhang, and D. Zermeno-Diaz, 2022: Understanding the role of topography on the diurnal cycle of precipitation in the maritime continent during mjo propagation. *Climate Dynamics*, **58**, 3003–3019, https://doi.org/10.1007/s00382-021-06085-0.

Tang, M., J. Dudhia, C. Liu, and G. Torri, 2025: Cold pools, breezes, and monsoons: Propagating convection over new guinea. *arXiv preprint arXiv:2506.00473*, URL http://arxiv.org/abs/2506.00473.

Tang, S., P. Gleckler, S. Xie, J. Lee, M. S. Ahn, C. Covey, and C. Zhang, 2021: Evaluating the diurnal and semidiurnal cycle of precipitation in cmip6 models using satellite- and ground-based observations. *Journal of Climate*, **34**, 3189–3210, https://doi.org/10.1175/JCLI-D-20-0639.1.

Tang, S., and Coauthors, 2022: Long-term single-column model intercomparison of diurnal cycle of precipitation over midlatitude and tropical land. *Quarterly Journal of the Royal Meteorological Society*, **148**, 641–669, https://doi.org/10.1002/qj.4222.

Tao, C., and Coauthors, 2024: Diurnal cycle of precipitation over the tropics and cen-

tral united states: intercomparison of general circulation models. *Quarterly Journal of the Royal Meteorological Society*, **150**, 911–936, https://doi.org/10.1002/qj.4629.

UCAR/NCAR, 2025: Wrf python. Computational and Informational System Lab.

Vincent, C. L., and T. P. Lane, 2016: Evolution of the diurnal precipitation cycle with the passage of a madden-julian oscillation event through the maritime continent. *Monthly Weather Review*, **144**, 1983–2005, https://doi.org/10.1175/MWR-D-15-0326.1.

Vincent, C. L., T. P. Lane, and M. C. Wheeler, 2016: A local index of maritime continent intraseasonal variability based on rain rates over the land and sea. *Geophysical Research Letters*, **43**, 9306–9314, https://doi.org/10.1002/2016GL069987.

Virts, K. S., J. M. Wallace, M. L. Hutchins, and R. H. Holzworth, 2013: Diurnal lightning variability over the maritime continent: Impact of low-level winds, cloudiness, and the mjo. *Journal of the Atmospheric Sciences*, **70**, 3128–3146, https://doi.org/10.1175/JAS-D-13-021.1.

Wang, S., and A. H. Sobel, 2017: Factors controlling rain on small tropical islands: Diurnal cycle, large-scale wind speed, and topography. *Journal of the Atmospheric Sciences*, **74**, 3515–3532, https://doi.org/10.1175/JAS-D-16-0344.1.

Wang, Y. C., S. Xie, S. Tang, and W. Lin, 2020: Evaluation of an improved convective triggering function: Observational evidence and scm tests. *Journal of Geophysical Research: Atmospheres*, **125**, https://doi.org/10.1029/2019JD031651.

Wei, Y., Z. Pu, and C. Zhang, 2020: Diurnal cycle of precipitation over the maritime continent under modulation of mjo: Perspectives from cloud-permitting scale simulations. *Journal of Geophysical Research: Atmospheres*, **125**, https://doi.org/10.1029/2020JD032529.

Wheeler, M. C., and H. H. Hendon, 2004: An all-season real-time multivariate mjo index: Development of an index for monitoring and prediction. *Monthly Weather Review*, **132**, 1917–1932, https://doi.org/https://doi.org/10.1175/1520-0493(2004)132⟨1917:AARMMI⟩2.0.CO;2.

Xiong, J., G. Tang, and Y. Yang, 2025: Continental evaluation of gpm imerg v07b precipitation on a sub-daily scale. *Remote Sensing of Environment*, **321**, https://doi.org/10.1016/j.rse.2025.114690.

Yang, S., and E. A. Smith, 2006: Mechanisms for diurnal variability of global tropical rainfall observed from trmm. *Journal of climate*, **19**, 5190–5226.

Yin, J., and A. Porporato, 2017: Diurnal cloud cycle biases in climate models. *Nature Communications*, **8**, https://doi.org/10.1038/s41467-017-02369-4.

Yokoi, S., S. Mori, M. Katsumata, B. Geng, K. Yasunaga, F. Syamsudin, Nurhayati, and K. Yoneyama, 2017: Diurnal cycle of precipitation observed in the western coastal area of sumatra island: Offshore preconditioning by gravity waves. *Monthly Weather Review*, **145**, 3745–3761, https://doi.org/10.1175/MWR-D-16-0468.1.

Yokoi, S., S. Mori, F. Syamsudin, U. Haryoko, and B. Geng, 2019: Environmental conditions for nighttime offshore migration of precipitation area as revealed by in situ observation off sumatra island. *Monthly Weather Review*, **147**, 3391–3407, https://doi.org/10.1175/MWR-D-18-0412.1.

Zelinka, M. D., T. A. Myers, D. T. McCoy, S. Po-Chedley, P. M. Caldwell, P. Ceppi, S. A. Klein, and K. E. Taylor, 2020: Causes of higher climate sensitivity in cmip6 models. *Geophysical Research Letters*, **47**, https://doi.org/10.1029/2019GL085782.

Zhang, C., and J. Ling, 2017: Barrier effect of the indo-pacific maritime continent on the mjo: Perspectives from tracking mjo precipitation. *Journal of Climate*, **30**, 3439–3459, https://doi.org/10.1175/JCLI-D-16-0614.1.

Zhou, X., P. Ray, J. Dudhia, S. Hagos, N. C. Johnson, E. Nikolopoulos, and B. S. Barrett, 2025: Role of diurnal cycle of insolation on the mjo propagation in the maritime continent. *Journal of Geophysical Research: Atmospheres*, **130**, https://doi.org/10.1029/2025JD044257.

Zhou, Y., S. Wang, and J. Fang, 2022: Diurnal cycle and dipolar pattern of precipitation over borneo during an mjo event: Lee convergence and offshore propagation. *Journal of the Atmospheric Sciences*, **79**, 2145–2169, https://doi.org/10.1175/JAS-D-21-0258.1, URL https://doi.org/10.1175/JAS-D-21-.

Zhou, Y., S. Wang, and J. Fang, 2023: Diurnal cycle and dipolar pattern of precipitation over borneo during the mjo: Linear theory and nonlinear sensitivity experiments. *Journal of Geophysical Research: Atmospheres*, **128**, https://doi.org/10.1029/2022JD037616.